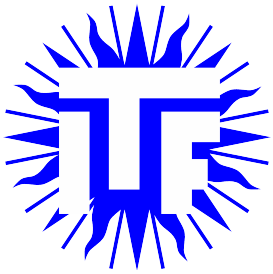

Utrecht University

Master Thesis

Institute for Theoretical Physics

Impurities in Fibonacci Chains, Local Symmetry and Topological Order

Author
Anouar Moustaj

Supervisor
Prof. Dr. Cristiane Morais Smith and
M.Sc. Sander Kempkes

June, 2020

Abstract

Topological order in condensed matter physics has grown to become an important concept in studying novel materials. It shows resilience of quantum properties (e.g. quantized resistivity in quantum-hall systems) against perturbations and therefore has many potential applications. Recently, some claims have been made that this topological order also exists in one-dimensional quasicrystals, and that its effects have been observed [1]. Due to the lack of periodicity in the lattice structure of quasicrystals, it is hard to study topological properties in conventional ways. One question that arises is how well protected topological phases are in this class of materials. In order to start addressing this question, we chose to investigate the effect of placing impurities in an otherwise quasiperiodic lattice.
To do so, we consider the tight-binding Fibonacci chain from the perspective of a real-space renormalization procedure. Two implementations of the quasiperiodic modulations are possible: the on-site potential or the hopping parameter. It is however shown that they are equivalent under renormalization. The effect of impurities in the hopping model is then analyzed and it is found that the amount by which quasiperiodic order is disturbed is highly dependent on what is called the renormalization path of the site at which the impurity is placed. We point to a link in the theory of local symmetry resonators in aperiodic binary chains and finally, the topological properties of the chain are overviewed. These include the appearance of a topological invariant, which is characterized by the presence of edge states.

Acknowledgements

First and foremost, I would like to thank my supervisors M.Sc. Sander Kempkes and prof. Dr. Cristiane Morais Smith for guiding me through the project and correcting my many mistakes. In the beginning of the project, I did not have enough knowledge of condensed matter physics and still chose to do a project in this area. They have spent a lot of time discussing many concepts with me and have led me to produce the work that is presented in this thesis. They have been very patient, and once again I thank them for that. I would also like to thank my student colleagues from the "Master Room", which, before the Corona times (and even after), have kept me company and alleviated the stress that is brought about by focusing on one's project for a long time. Lastly, I would like to thank my relatives that are hosting me. The household consists of my aunt and two cousins, without whom I would not have been able to complete this master in Utrecht. They were especially considerate during the Covid-19 pandemic, as we all had to share the same space for a long period of time.

Contents

1. Introduction

Two seemingly unrelated areas of condensed matter were born around the same period, about forty years ago. These are the fields of topological matter and quasicrystals. They have both been evolving on their own and produced many discoveries and Nobel prizes [2][3][4]. Quasicrystals were first discovered by Dan Schetchman in 1984 [5]. They introduce a new order of solid-state matter, in which the microscopic structure does not follow a spatially periodic arrangement. Their electronic and elastic properties distinguish them from usual crystalline matter, where quasicrystals show poor conductivity and high tensile strengths [6]. They have been mostly studied in one-dimensional systems, as the absence of perfect periodicity makes them very difficult to model. These one-dimensional quasicrystals nonetheless provide most of the novel features present in all dimensions [6].
Topological order, as discovered by David Thouless *et al.* in their seminal paper [7], set in place a new field of physics. It is that of quantum matter with resilient properties against decoherence, therefore opening up a vast well of potential applications, such as topological quantum computations [8]. This topological order was later found to describe the quantum-Hall effect in all its forms, which in turn provided the best known method to probe the fundamental constants of physics [9]. These two discoveries already account for three Nobel prizes (one for the Kosterlitz-Thouless phase transition and two quantum-Hall effects).

Recently, these two fields started to intertwine when it was claimed that topological order was found in one-dimensional quasicrystals [1][10]. In order to understand this relation, we first start by a comprehensive review on what is meant by symmetry protected topological order. This is why in chapter two, we review the important symmetries of condensed matter. In chapter three, we explain what topological states are and give a few examples of these. It is followed by the presentation of a general framework, the Ten-fold way, that describes symmetry protected topological phases. Chapter four is an overview of a theoretical framework treating systems with locally symmetric potentials. In Chapter five, we focus our study in the one-dimensional Fibonacci chain, which is quasiperiodic, has scale invariance and a self-similar spectrum. It also possesses reflection symmetries at all levels. This chain can be thought of as a departure from complete periodicity, while still containing a very high level of order in its spatial structure. We will

present a comprehensive picture on the fragmentation of the spectrum through a real-space renormalization procedure. There, a notion of renormalization path emerges, which is used to characterize the level of disorder induced by the presence of impurities that we will add later on. This part constitutes our original contribution to the work. It is found that, depending on the renormalization path of the site at which the impurity is placed, different classes of disorders emerge and they can all be classified in terms of the same renormalization path. Finally, in chapter six, we present alternative approaches to determine the topological order and point to a correspondence with the theory of local resonator modes [11].

2. Symmetries

One surprising aspect of nature is that it tends to have similar phenomena happening all over the universe's scales. This also seems to be true in a temporal sense. When one peers through a telescope at the past, an important observation is made; the laws governing the dynamics of the universe have been the same throughout its existence. In other words, they seem to be constant over space and time. In a sense, one can always find inherent symmetries in nature, and this has profound consequences for the laws governing its behavior.
In physics, one calls symmetry any property of a system that remains unchanged after a transformation, whether active or passive, is applied to the system. Some of the important insights into symmetries were given a mathematical foundation by Emmy Noether [12]. She is one of the first persons to link conservation laws in physics to symmetry. To this day, a theorem named after her is still the starting point for many physics students that get introduced to the concept of symmetry.
In this section, we will briefly discuss global symmetries that lead to conservation laws. After that, we will discuss the three fundamental discrete symmetries that are relevant to condensed matter systems and have important consequences in the topological features thereof.

2.1 Global Symmetries and Noether's Theorem

The starting point of this discussion will be on global symmetries. These are global transformations that leave the action of a system invariant. They are global in the sense that they are independent of a system's coordinates. They transform the system everywhere in the same way. One can state that the condition for a transformation T to be a symmetry of the action is that it acts trivially on the action functional $S \equiv \int dt L$, where $L(\mathbf{x}, \dot{\mathbf{x}}, t)$ is the system's Lagrangian function $T : S \mapsto S$.
The connection to physically conserved quantities happens by applying continuous transformations, or differentiable transformations (with respect to a set of continuous parameters). The infinitesimal variations $\delta_\alpha x_i = \alpha$, induced by the transformation on $i = 1, \cdots, N$ generalized coordinates, result in a variation of

the action given by

$$\delta_\alpha S = \int_{t_1}^{t_2} dt \delta_\alpha L = \sum_{i=1}^{N} \int_{t_1}^{t_2} dt \left(\frac{\partial L}{\partial x_i} \alpha_i + \frac{\partial L}{\partial \dot{x}_i} \frac{d\alpha_i}{dt} \right) = 0, \tag{2.1}$$

where δ_α refers to the variation induced by the specific symmetry transformation. Using integration by parts, we can write the above equation as

$$\delta_\alpha S = \sum_{i=1}^{N} \left(\frac{\partial L}{\partial \dot{x}_i} \alpha_i \Big|_{t_1}^{t_2} + \int_{t_1}^{t_2} dt \left(\frac{\partial L}{\partial x_i} - \frac{d}{dt} \left(\frac{\partial L}{\partial \dot{x}_i} \right) \right) \alpha_i \right) = 0.$$

When combined with the Euler-Lagrange equations, resulting from the principle of least action $\delta S = 0$ for a general variation in the action functional, the second term vanishes and we end up with a conserved *Noether charge*

$$Q \equiv \sum_{i=1}^{N} \frac{\partial L}{\partial \dot{x}_i} \alpha_i. \tag{2.2}$$

This is the essence of *Noether's theorem*, which states that *any continuous symmetry gives rise to a conservation law.* Note that an additional total derivative term $d\Lambda/dt$ can be added to the variation in the Lagrangian and modify the expression for the conserved charge to

$$Q = \sum_{i=1}^{N} \frac{\partial L}{\partial \dot{x}_i} \alpha_i - \Lambda. \tag{2.3}$$

The field theoretic version of the previous discussion replaces generalized coordinates with fields of infinite degrees of freedom. The Lagrangian is then expressed in terms of some fields $\phi_i(\mathbf{x}, t)$ and their derivatives. Since this approach incorporates relativity, we can express the action as a spacetime integral of the Lagrangian density, defined through $L = \int d^3x \mathcal{L}$ and make the time parameter a coordinate of the system. Using Einstein's notation, the action can then be written as

$$S = c^{-1} \int d^4x \mathcal{L}(\phi_i(x), \partial_\mu \phi_i(x), x_\mu),$$

where c denotes the speed of light, and appears because we write the time coordinate as $x_0 = ct$. Note that in most cases in physics, we only consider the first order derivatives in the Lagrangian, but we can always extend the formulation so as to contain higher order derivatives of the fields. How does Noether's theorem look like in this case? Letting a general infinitesimal symmetry transformation vary the fields like $\delta_\alpha \phi_i = \alpha \Theta_i$ and inducing changes in the Lagrangian density of the form $\mathcal{L} \to \mathcal{L} + \alpha \partial_\mu \Lambda^\mu$, we derive in a similar way to the particle mechanics case, the following *Noether current*

$$j^\mu \equiv \sum_i \frac{\partial \mathcal{L}}{\partial(\partial_\mu \phi_i)} \Theta_i - \Lambda^\mu. \tag{2.4}$$

Another formulation of these ideas can be obtained when considering the Legendre transform of the Lagrangian $L(\mathbf{x}, \dot{\mathbf{x}}, t) \rightarrow H(\mathbf{x}, \mathbf{p}, t) = \frac{\partial L}{\partial \dot{\mathbf{x}}} \cdot \dot{\mathbf{x}} - L(\mathbf{x}, \dot{\mathbf{x}}, t) = \mathbf{p} \cdot \dot{\mathbf{x}} - L$. This is sometimes useful because it can be translated to quantum mechanics through canonical quantization. In that case, we consider symmetries of the Hamiltonian, which generate the variations

$$\delta H = \sum_i \left(\frac{\partial H}{\partial x_i} \delta x_i + \frac{\partial H}{\partial p_i} \delta p_i \right) = \sum_i \alpha \left(\frac{\partial H}{\partial x_i} \frac{\partial \Omega}{\partial p_i} - \frac{\partial H}{\partial p_i} \frac{\partial \Omega}{\partial x_i} \right) = 0.$$

The second equality follows by rewriting the infinitesimal changes in the canonical variables in terms of the Hamiltonian equations of motion and a generating function $\Omega(\mathbf{x}, \mathbf{p}, t)$, which has the role of generating a canonical transformation. The above can be written in terms of Poisson brackets and we get

$$\delta H = \alpha \{H, G\} = 0 \quad \text{for a canonical symmetry transformation.} \tag{2.5}$$

Since the Poisson bracket of any function of canonical coordinates and the Hamiltonian generates time derivatives of that function, we have for the Noether charge the following relation:

$$\frac{dQ}{dt} = \{Q, H\} = 0, \tag{2.6}$$

which tells us that they are generators of canonical symmetry transformations. Once we leave the classical realm and quantize our system, the Poisson brackets can just be replaced by commutators, $\{Q, H\} \rightarrow (1/i\hbar)[Q, H]$, provided the classical symmetries are obeyed in the quantized theory.

2.2 Fundamental Discrete Symmetries of Condensed Matter Systems

The symmetries of relativistic physics are generally described in terms of the Poisson group. However, once one begins describing lattice systems, the continuous spatial symmetries of open space are lost and there is a spontaneous breaking of Lorentz symmetry when a crystal forms. Nevertheless, one can still make use of some residual discrete symmetries that exist in such systems, such as translational symmetry or time-reversal symmetry. In this section, we will discuss some of the important discrete symmetries of condensed matter systems. A fundamental Hamiltonian that we can start with in condensed matter systems is given by

$$\begin{aligned} \hat{\mathcal{H}} = & \sum_i \left(c\boldsymbol{\alpha} \cdot \hat{\mathbf{p}}_i + \beta m_e c^2 \right) + \frac{1}{2} \sum_{i,j} \frac{e^2}{|\mathbf{r}_i - \mathbf{r}_j|} \\ & + \sum_i \frac{\hat{\mathbf{P}}_i^2}{2M_i} + \sum_{i,j} \frac{e^2 Z_j}{|\mathbf{r}_i - \mathbf{R}_j|} + \sum_{i,j} \frac{e^2 Z_i Z_j}{|\mathbf{R}_i - \mathbf{R}_j|} + U_{ext}. \end{aligned}$$

The first term is the Dirac equation for all electrons in the system while the second is the Coulomb interaction between them. In the first term, $\boldsymbol{\alpha}$ is a vector of 4×4 matrices and β is another 4×4 matrix obeying the relations $\alpha_i^2 = \beta^2 = \mathbb{1}$ and which mutually anticommute, m_e is the electron's mass, e its charge, $\mathbf{r}_i$ the position of the i^{th} electron and $\hat{\mathbf{p}}_i$ is its momentum. The third term is the kinetic energy of all nuclei, where $\hat{\mathbf{P}}_i$ is the i^{th} nucleus' momentum and M_i its mass. The fourth term is the Coulomb interaction between electrons and nuclei, where Z_i is the atomic number of the i^{th} nucleus and $\mathbf{R}_i$ is its position vector. Finally, the fifth term is the Coulomb interaction between all nuclei (the last term is just an external potential). It is of course impossible to solve such a system as one has to deal with an order of 10^{23} electrons and nuclei. However, if quantum computers are ever realized, there would be a possibility for such systems to be solved to great accuracy. Nevertheless, there are many models that simplify the picture and offer a probe on the relevant physics.

Here, we discuss a simple, yet important Hamiltonian of condensed matter systems. It is one with a discrete set of continuous energy spectrum, from which many properties of solids can be understood. In the simplest case, we model a solid as a lattice where non-interacting and non-relativistic electrons roam under the influence of a periodic potential due to idealized fixed atomic nuclei. The Hamiltonian in this case can be written as

$$\hat{H} = \sum_{i=1}^{N} \left(\frac{-\hbar^2 \nabla_i^2}{2m} + U(\mathbf{r}_i) \right), \tag{2.7}$$

where the sum runs over N electrons, and the potential is assumed to be periodic over the lattice, $U(\mathbf{r}) = U(\mathbf{r} + \mathbf{R})$, with $\mathbf{R}$ being any vector of the Bravais lattice. It can be shown that, since the electrons are non-interacting, the eigenvalues of this Hamiltonian are given by the sum of eigenvalues of the single-electron Hamiltonian. Felix Bloch worked out the resulting physics and according to his theorem [13], any particle's wavefunction subject to a potential with discrete translational symmetry can be decomposed into a set of periodic wavefunctions of the form

$$\psi_{n\mathbf{k}}(\mathbf{r}) = \frac{e^{i\mathbf{k}\cdot\mathbf{r}} u_{n\mathbf{k}}(\mathbf{r})}{\sqrt{N}} \tag{2.8}$$

where $\mathbf{k}$ is called the *Bloch wave vector*, $\hbar\mathbf{k}$ is the *crystal momentum* and n the *band index*. For each $\mathbf{k}$, there are infinitely many eigenstates of the Bloch Hamiltonian, labeled by the band index. For each of those, there is an associated energy eigenvalue, called *band energy* $E_{\mathbf{k}}$. This band structure allows us to distinguish different types of solids, depending on the overall electronic properties that are allowed. It is convenient to set the *Fermi energy* (the energy of the highest occupied state in a fermionic multi-particle system at absolute zero) to zero. Once thermal energy is added to the system, the amount of excitations above the Fermi

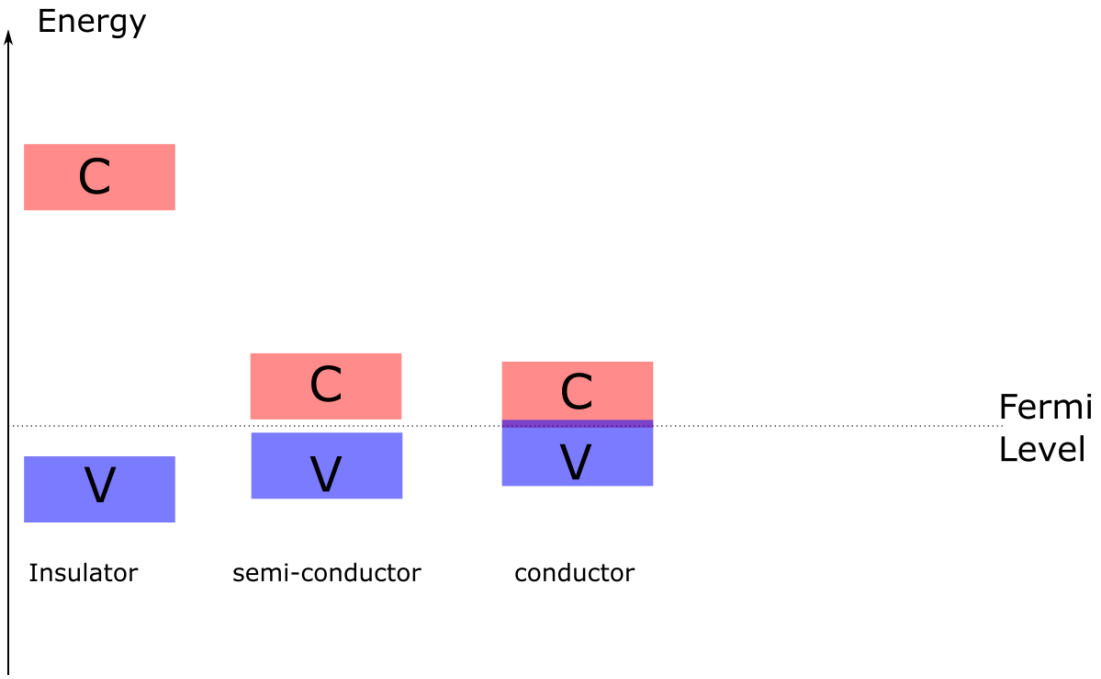

Figure 2.1: Energy bands in solids. C stands for conduction band and V for valence band.

level will depend on how far apart the energy bands are from each other. Since we are discussing lattice systems where the potentials come from atomic nuclei, the highest occupied band beneath the Fermi level is called the *valence band*, while the one above is called the *conduction band*, from which the electrons start roaming through the solid. Depending on the energy difference between these two (usually called the *band-gap*), we either deal with conductors, semiconductors or *band* insulators. A schematic picture of these materials is depicted in figure 2.1. More exotic phases, such as superconductors, topological insulators and so on, which on top of thermal fluctuations also depend on quantum fluctuations, also exist and are much more interesting than the regular ones depicted above.

Now that we have discussed the Bloch Hamiltonian, we will take a look at some of the discrete symmetries that are relevant to the discussion on topological properties that will follow later on.

2.2.1 Time-Reversal Symmetry

We start with transformations that invert the flow of time, $T : t \to -t$. Under this operation, the classical position transforms trivially, while the classical momentum operator undergoes inversion. Requiring this to hold for the quantum mechanical

operators,

$$\begin{aligned} T\hat{\mathbf{x}}T^{-1} &= \hat{\mathbf{x}}, \\ T\hat{\mathbf{p}}T^{-1} &= -\hat{\mathbf{p}}, \end{aligned} \tag{2.9}$$

means that in order to preserve the canonical commutation relations $[\hat{x}_i, \hat{p}_j] = i\hbar\delta_{ij}$, the time reversal operator must be anti-unitary, which can be written as a complex conjugation operator K followed by a unitary operator U, $T = UK$. For the spin operator, the only way for the spin commutation relation to hold under time reversal,

$$T[\hat{S}_i, \hat{S}_j]T^{-1} = T(i\hbar\epsilon_{ijk}S_k)T^{-1},$$

is that the action of time reversal on the spin operator is given by

$$T\hat{\mathbf{S}}T^{-1} = -\hat{\mathbf{S}}. \tag{2.10}$$

The spin operators for fermions (half-integer spin) are usually depicted in the irreducible representation of the $SU(2)$ group spanned by Pauli matrices, σ_i with $i \in \{1, 2, 3\}$. In that case, the time reversal operator is represented by anti-unitary 2×2 matrices, and we can deduce the following relation:

$$T\boldsymbol{\sigma}T^{-1} = -\boldsymbol{\sigma}, \tag{2.11}$$

where $\boldsymbol{\sigma} = (\sigma_1, \sigma_2, \sigma_3)$. As we already stated before, the time reversal operator is composed of a unitary operator and a complex conjugation operator. In order for equation (2.11) to hold, one must impose the following form on the unitary part of T: $U = e^{i\phi}\sigma_2$. This can be seen by writing the components of equation (2.11):

$$\begin{aligned} UK\sigma_1 KU^\dagger &= U\sigma_1 U^\dagger = -\sigma_1, \\ UK\sigma_2 KU^\dagger &= U\sigma_2^* U^\dagger = -\sigma_2, \\ UK\sigma_3 KU^\dagger &= U\sigma_3 U^\dagger = -\sigma_3. \end{aligned}$$

These equations can only be simultaneously satisfied if $U = e^{i\phi}\sigma_2$. Applying the time reversal operator twice results in $T^2 = UKUK = e^{i\phi}\sigma_2 e^{-i\phi}\sigma_2^* = -\mathbb{1}$. In other words, we do not get the same states back when flipping the arrow of time twice, as we would expect classically. This result holds for spin $\frac{1}{2}$ particles and is in fact related to the fundamental antisymmetric nature of fermionic operators in general. For integer spin, the result is $T^2 = \mathbb{1}$.

When time reversal is a symmetry of the Hamiltonian, Kramers' theorem [14] tells us that each energy eigenvalue is doubly degenerate for any system with an odd number of fermionic particles. This will have important consequences for the topological properties of the materials as will be discussed later on. This only works for odd fermion parity because of the anti-unitary nature of the time reversal operator. On a Hilbert space of N particles, it must obey

$$\mathcal{T}^2 == (T^2 \otimes T^2 \otimes \cdots \otimes T^2) = (-1)^N \mathbb{1}^{\otimes N},$$

meaning $\mathcal{T}^2$ is anti-unitary if and only if N is odd.
To see Kramer's theorem in action, we can write the noninteracting many-body Hamiltonian in the second-quantized formalism,

$$\hat{\mathcal{H}} = \sum_{\mathbf{k},\alpha\in\{\uparrow,\downarrow\}} H(\mathbf{k})\psi^\dagger_{\mathbf{k}\alpha}\psi_{\mathbf{k}\alpha}, \tag{2.12}$$

where we are assuming that we are dealing with electrons living in one band, so that we may drop the band index, and where $\psi^\dagger_{\mathbf{k}\alpha}$ and $\psi_{\mathbf{k}\alpha}$ are electron creation and annihilation operators acting on states living in Fock space. $H(\mathbf{k}) = \langle\mathbf{k}|\,\hat{H}\,|\mathbf{k}\rangle = E_{\mathbf{k}}$ is the Bloch state energy eigenvalue, with $\hat{H}$ the Bloch Hamiltonian (first quantization Hamiltonian given in equation (2.7)). If we want the Hamiltonian to be invariant under this transformation, $[\hat{\mathcal{H}}, \mathcal{T}] = 0$, where $\mathcal{T}$ is the time reversal operator acting on the Fock space, then we have to impose the following condition on the Bloch Hamiltonian

$$TH(\mathbf{k})T^{-1} = H(-\mathbf{k}). \tag{2.13}$$

Hence we obtain the same energy eigenvalue for an electron with momentum $-\mathbf{k}$ as one with $\mathbf{k}$. Therefore, the spectrum is at least doubly degenerate, which is the statement of Kramer's theorem.

2.2.2 Particle-Hole Symmetry

This symmetry finds its importance in the description of superconducting systems. It more commonly called charge conjugation symmetry. The transformation $\mathcal{C}$ it enforces on a system turns creation operators into annihilation operators in Fock space: $\mathcal{C}\psi^\dagger\mathcal{C}^{-1} = \psi$. We will describe the symmetry in the context of a superconducting Hamiltonian. The second quantized Hamiltonian, including interactions is given by

$$\hat{\mathcal{H}} = \sum_{\mathbf{k},\alpha,\beta} \psi^\dagger_{\mathbf{k}\alpha} H_{\alpha\beta}(\mathbf{k})\psi_{\mathbf{k}\beta} + \frac{1}{2}\sum_{\mathbf{k},\alpha,\beta}\sum_{\mathbf{k}',\alpha',\beta'} \psi^\dagger_{\mathbf{k}\alpha}\psi^\dagger_{-\mathbf{k}\beta} V_{\alpha\beta\alpha'\beta'}(\mathbf{k},\mathbf{k}')\psi_{-\mathbf{k}'\alpha'}\psi_{\mathbf{k}'\beta'} \tag{2.14}$$

where we have added the possibility for the Bloch Hamiltonian to contain a spin degree of freedom. We consider for the superconducting system the following expansions in the interaction term

$$\begin{aligned}
\psi^\dagger_{\mathbf{k}\alpha}\psi^\dagger_{-\mathbf{k}\beta} &= \langle\psi^\dagger_{\mathbf{k}\alpha}\psi^\dagger_{-\mathbf{k}\beta}\rangle + (\psi^\dagger_{\mathbf{k}\alpha}\psi^\dagger_{-\mathbf{k}\beta} - \langle\psi^\dagger_{\mathbf{k}\alpha}\psi^\dagger_{-\mathbf{k}\beta}\rangle),\\
\psi_{\mathbf{k}\alpha}\psi_{-\mathbf{k}\beta} &= \langle\psi_{\mathbf{k}\alpha}\psi_{-\mathbf{k}\beta}\rangle + (\psi_{\mathbf{k}\alpha}\psi_{-\mathbf{k}\beta} - \langle\psi_{\mathbf{k}\alpha}\psi_{-\mathbf{k}\beta}\rangle),
\end{aligned}$$

and only keep terms that are at most second order in the operators. This is because we expect *Cooper pairs* to form and their energies to dominate in the

original Hamiltonian. The resulting mean-field effective Hamiltonian for a single band superconducting system is given by

$$\hat{\mathcal{H}} = \sum_{\mathbf{k},\alpha,\beta} \psi^\dagger_{\mathbf{k}\alpha} H_{\alpha\beta}(\mathbf{k}) \psi_{\mathbf{k}\beta} + \frac{1}{2} \sum_{\mathbf{k},\alpha,\beta} \left[\psi^\dagger_{\mathbf{k}\alpha} \Delta_{\alpha\beta}(\mathbf{k}) \psi^\dagger_{-\mathbf{k}\beta} + \psi_{-\mathbf{k}\alpha} \Delta^\dagger_{\alpha\beta}(\mathbf{k}) \psi_{\mathbf{k}\beta} \right], \quad (2.15)$$

where we have also defined the *pair potential*

$$\Delta_{\alpha\beta}(\mathbf{k}) \equiv - \sum_{\mathbf{k}',\alpha',\beta'} V_{\alpha\beta\alpha'\beta'}(\mathbf{k},\mathbf{k}') \langle \psi_{\mathbf{k}\alpha'} \psi_{-\mathbf{k}\alpha'} \rangle.$$

Defining a vector containing both the creation and annihilation operators $\Psi_{\mathbf{k}\alpha} \equiv (\psi^\dagger_{\mathbf{k}\alpha}, \psi_{-\mathbf{k}\alpha})$, the Hamiltonian can be written as

$$\hat{\mathcal{H}} = \frac{1}{2} \sum_{\mathbf{k},\alpha,\beta} \Psi_{\mathbf{k}\alpha} \mathbf{H}_{\alpha\beta}(\mathbf{k}) \Psi^\dagger_{\mathbf{k}\beta}, \quad (2.16)$$

with

$$\mathbf{H}_{\alpha\beta}(\mathbf{k}) \equiv \begin{pmatrix} H_{\alpha\beta}(\mathbf{k}) & \Delta_{\alpha\beta}(\mathbf{k}) \\ \Delta^\dagger_{\alpha\beta}(\mathbf{k}) & -H_{\beta\alpha}(-\mathbf{k}) \end{pmatrix}.$$

It is now almost obvious that such a Hamiltonian is invariant under the exchange of the particle and hole sectors. Defining the anti-unitary matrix

$$\mathcal{C} \equiv \begin{pmatrix} 0 & \mathbb{1} \\ \mathbb{1} & 0 \end{pmatrix} K,$$

where $\mathbb{1}$ is the identity in spin space, the Hamiltonian stays invariant under its action and we deduce that the $\mathbf{H}$ matrix transforms as

$$\mathcal{C}\mathbf{H}(\mathbf{k})\mathcal{C}^{-1} = -\mathbf{H}(-\mathbf{k}), \quad (2.17)$$

which is the mathematical statement for *particle-hole symmetry*. This Hamiltonian is closely related to the multi-band *Bogoliubov de-Gennes* Hamiltonian, which takes into account a set of N creation and N annihilation operators (one for each band or one for each lattice site).
The symmetry is in fact related to the construction of this Hamiltonian. It reflects the redundancy in the degrees of freedom, since the creation operators are related to the annihilation ones by a "dagger operation". If we let $\mathbf{V}_\alpha(\mathbf{k}) \equiv (u_\alpha(\mathbf{k}), v^*_\alpha(-\mathbf{k}))^T$ be an eigenvector of $\mathbf{H}(\mathbf{k})$ satisfying

$$\mathbf{H}(\mathbf{k})\mathbf{V}_\alpha(\mathbf{k}) = \varepsilon(\mathbf{k})\mathbf{V}_\alpha(\mathbf{k}),$$

particle-hole symmetry implies that we have

$$\mathbf{H}(\mathbf{k})(\mathcal{C}\mathbf{V}_\alpha(-\mathbf{k})) = -\varepsilon(-\mathbf{k})(\mathcal{C}\mathbf{V}_\alpha(-\mathbf{k})).$$

In other words, eigenvalues come in pairs and we have a diagonalized **H** matrix given by

$$U_d(\mathbf{k})\mathbf{H}(\mathbf{k})U_d^\dagger(\mathbf{k}) = \begin{pmatrix} \varepsilon_\uparrow(\mathbf{k}) & & & \\ & \varepsilon_\downarrow(\mathbf{k}) & & \\ & & -\varepsilon_\uparrow(-\mathbf{k}) & \\ & & & -\varepsilon_\downarrow(-\mathbf{k}) \end{pmatrix}. \tag{2.18}$$

This doubling/pairing of energies has important consequences for the protection of topological states discussed later on.

2.2.3 Chiral Symmetry

The last of the three fundamental discrete symmetries is chiral symmetry, or as it is most commonly realized in condensed matter, sublattice symmetry. It is a mixture of both time-reversal and particle-hole symmetry. This kind of symmetry arises when we consider, for example, a lattice with two different groups of cells that form their own sublattices. In this case, the Hamiltonian can be schematically thought as a direct sum of the two sublattice blocks $H \sim A \bigoplus B$. It will contain information about hopping between the two sublattices encoded in off-diagonal blocks. When such a Hamiltonian can be written as

$$\mathcal{H} = \begin{pmatrix} 0 & H_{AB} \\ H_{AB}^\dagger & 0 \end{pmatrix}, \tag{2.19}$$

then it contains sublattice symmetry. That is, we can define a matrix

$$\Sigma_z = \begin{pmatrix} \mathbb{1} & 0 \\ 0 & -\mathbb{1} \end{pmatrix},$$

for which we have the following relation

$$\Sigma_z \mathcal{H} \Sigma_z^{-1} = -\mathcal{H}. \tag{2.20}$$

This means that if $\Psi = (\psi_A, \psi_B)^T$ is an eigenvector of $\mathcal{H}$ with eigenvalue ε, then $\Sigma_z\Psi = (\psi_A, -\psi_B)^T$ is an eigenvector with eigenvalue $-\varepsilon$. The spectrum of energies always comes in symmetric pairs and as we shall later see, this can render any topological classification trivial.
Chiral symmetry is in fact present whenever one has time-reversal and particle-hole symmetries, which means it can be expressed in terms of the latter two. With particle-hole symmetry, one has an equivalent description of both the particle and the hole, with the sign of their charge interchanged, which amounts to invariance under parity $P : \mathbf{r} \to -\mathbf{r}$. If time-reversal symmetry is also present, then one has invariance of "handedness", which can be defined as whether the direction of spin is the same as that of linear momentum (helicity) or whether a molecule stays

the same when subject to its mirror image. The last statement is that of chiral symmetry. Note that in a more abstract setting, chirality is actually defined as whether the particle in question transforms under the right-handed or left-handed representation of the Poincaré group.

After having briefly discussed the important symmetries in condensed matter systems, we will now move to the role of topology in the next chapter. In there, we will see that the symmetries we mentioned here play an important role in categorizing the kind of topological invariants that characterize different systems.

3. The Role of Topology

In this section, we investigate the role of topology in the description of quantum mechanical condensed matter systems. To this end, we first describe the **Q**uantum **H**all **E**ffect (QHE). This is followed by an analysis of the Kitaev chain, and finally we briefly describe a general framework for characterizing topological insultators and superconductors through the *tenfold way*.

3.1 The quantum-Hall Effect

3.1.1 Classical Drude Model

As a starting point, we briefly describe the classical setup in which the classical Hall Effect takes place. We consider a two dimensional material, through which a current I passes across. When a magnetic field B is applied in a direction perpendicular to the surface, a *Hall voltage* is created. This is because the charge carriers that move along the current deviate from their paths by following a circular trajectory. The frequency of this motion is

$$\omega_B \equiv \frac{eB}{m},$$

also called *cyclotron frequency*. To get a bit more quantitative, we consider the *Drude model* for charge transport. The equation of motion, in the presence of both an electric and magnetic field ($\mathbf{E}$ and $\mathbf{B}$) and friction effects, is

$$m\dot{\mathbf{v}} = -e(\mathbf{E} + \mathbf{v} \times \mathbf{B}) - \frac{m}{\tau}\mathbf{v},$$

where m is the mass of the charge carrier, and τ is a characteristic collision time between the charge carriers. When we consider an equilibrium situation, where the velocity is constant, we can write the equation as

$$\begin{pmatrix} 1 & \omega_B\tau \\ -\omega_B\tau & 1 \end{pmatrix} \mathbf{J} = \frac{e^2 n\tau}{m}\mathbf{E}, \tag{3.1}$$

where we introduced the current density $\mathbf{J} = -ne\mathbf{v}$. By inverting the above matrix, one obtains a general form of *Ohm's law*, $\mathbf{J} = \sigma\mathbf{E}$, where σ is the conductivity of

the material. In the case of the Drude model, this takes the form

$$\sigma = \frac{e^2 n\tau}{m(1+\omega_B^2\tau^2)} \begin{pmatrix} 1 & -\omega_B\tau \\ \omega_B\tau & 1 \end{pmatrix}.$$

The off-diagonal components of the conductivity tensor are responsible for the Hall effect. The magnetic field deflects the charge carriers and there is a build up of charge along the edges of the material. This creates an electric field in the direction perpendicular to the initial current, which is responsible for the Hall voltage across the material.
In the laboratory, people will measure the resistance R of a material, which in turn depends on the resistivity ρ, through $R = \rho L/A$, where L is the length across the material and A the cross sectional area through which current is passing. The resistivity is defined as the inverse of conductivity $\rho \equiv \sigma^{-1}$. In the Drude model, it is easy to compute and we obtain

$$\rho_{xx} = \frac{m}{e^2 n\tau}, \qquad \rho_{xy} = \frac{m\omega_B}{ne^2} = \frac{B}{ne}. \tag{3.2}$$

Hence, in the simple Drude model, the resistance $R_{xy} = R_H B$ grows linearly with the magnetic field B, where we defined the *Hall coefficient* R_H ($R_H = 1/ne$ in the Drude model), which is also the effect observed by Edwin Hall in 1879 [15].

The story does not end with the simplistic classical model that we described above. In 1980, Klaus von Klitzing discovered that this effect was in fact quantised at low temperatures [9]. The original measurements are shown in figure 3.1. He was awarded the Nobel prize of physics in 1985 for the discovery. The discovery of this exact quantisation of a macroscopic observable is somewhat surprising, and it therefore marks the start of a new era of theoretical investigations into this effect. It turned out that the off-diagonal resistivity was quantised as follows

$$\rho_{xy} = \frac{2\pi\hbar}{e^2}\frac{1}{\nu} = \frac{h}{e^2\nu}, \tag{3.3}$$

for a range of magnetic field values B, where $\nu \in \mathbb{Z}$ is called the *filling fraction*. Between each plateau, there is sharp increase to the next plateau at the next value of ν. The QHE was observed in a variety of materials at very low temperatures, but also at room temperature in graphene [16]. We will now describe the effect in a theoretical setting.

3.1.2 Integer quantum-Hall Effect

We start the discussion by determining the quantum mechanical conductivity. Note that the following derivations are based on a quantum mechanical description

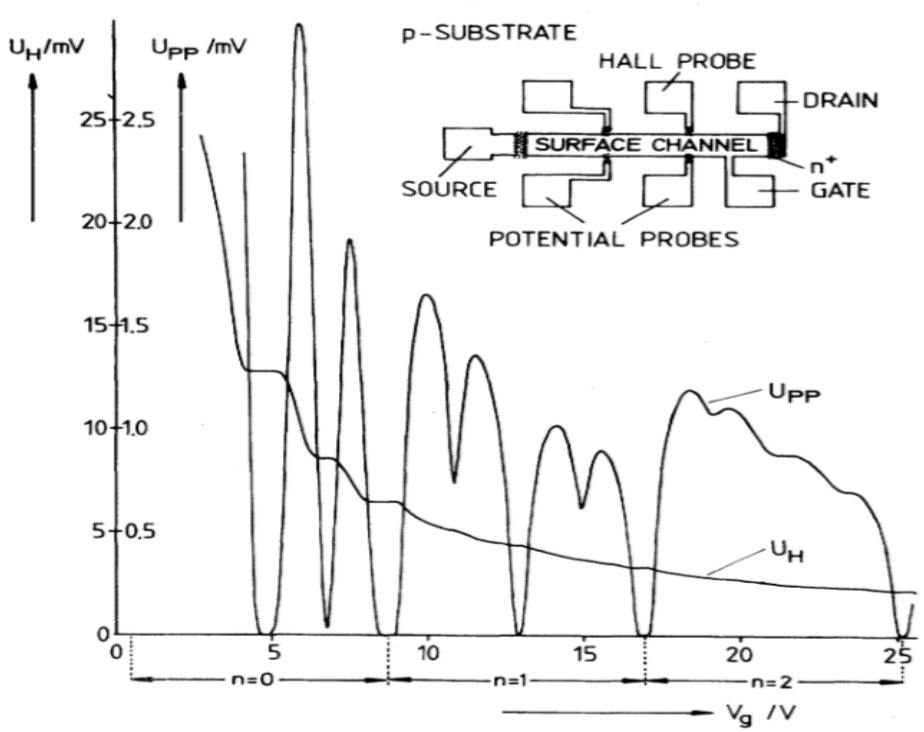

Figure 3.1: Original measurements from Von Klitzing *et al.*, showing quantisation of the Hall Voltage given by the curve U_H. Figure from Ref. [9]

of a single particle in an electromagnetic field (see appendix A).
In this case, to find the quantum mechanical current, we need to compute

$$\mathbf{I} = -e\mathrm{Tr}\left(\dot{\mathbf{x}}\right) = -\frac{e}{m}\sum_{\text{filled states}} \langle\psi|\left(-i\hbar\nabla + e\mathbf{A}\right)|\psi\rangle\,.$$

To make things easier, we deal with the vector potential in the Landau gauge $\mathbf{A} = xB\hat{\mathbf{y}}$, and assume that an electric field pointing in the x direction is present. Furtermore, we assume that there are ν Landau levels filled. The currents in the x and y directions then take the forms

$$\begin{aligned} I_x &= -\frac{e}{m}\sum_{n=1}^{\nu}\sum_k \langle\psi_{nk}| - i\hbar\partial_x\,|\psi_{nk}\rangle\,, \\ I_y &= -\frac{e}{m}\sum_{n=1}^{\nu}\sum_k \langle\psi_{nk}|\,\hbar k + eBx\,|\psi_{nk}\rangle\,. \end{aligned} \tag{3.4}$$

The first of these is zero, as the expectation value of the momentum of a harmonic oscillator is zero. In the second one, we use the fact that the expectation value of the position of this harmonic oscillator is $x_0' = -\hbar k/eB - mE/eB^2$. This results

in a current in the y direction, given by

$$I_y = -\frac{e}{m}\sum_{n=1}^{\nu}\sum_{k}\frac{-mE}{B} = e\nu\sum_{k}\frac{E}{B} = e\nu\frac{AE}{\Phi_0},$$

where we used the number of electrons (ommiting the spin degree of freedom) computed in (A.7). Dividing by the area to obtain the current density $\mathbf{J}$, we see that

$$\mathbf{J} = \begin{pmatrix} 0 \\ eE\nu/\Phi_0 \end{pmatrix} = \begin{pmatrix} 0 & -e\nu/\Phi_0 \\ e\nu/\Phi_0 & 0 \end{pmatrix}\begin{pmatrix} E \\ 0 \end{pmatrix}, \tag{3.5}$$

from which it can be inferred that the resistivity is given by

$$\rho = \begin{pmatrix} 0 & \Phi_0/e\nu \\ -\Phi_0/e\nu & 0 \end{pmatrix} = \begin{pmatrix} 0 & h/e^2\nu \\ -h/e^2\nu & 0 \end{pmatrix},$$

which is indeed the same as equation (3.3).

The previous derivation of the resistivity just tells us that it is quantised, but not why it stays the same for a range of magnetic field values. The reason for this is due to the fact that the experiments are done in samples that are not completely clean. This introduces the notion of disorder within the solid, due to all the impurities present.
Generally, the disorder is described by a *random potential* $V(\mathbf{x})$. We assume that it is much smaller than the level spacing $\hbar\omega_B$, so that we can treat it as a perturbation. Furthermore, we assume that the potential varies very slowly within the scale of a magnetic length l_b: $|\nabla V| \ll \hbar\omega_B/l_b$. This results in the lifting of degeneracy of Landau levels, together with the localization of the states to particular spatial regions. To see why, we consider the quantum operators that describe the centre of cyclotron orbits:

$$x_c = x - \frac{\Pi_y}{m\omega_B},$$
$$y_c = y + \frac{\Pi_x}{m\omega_B}.$$

The Heisenberg equation of motion dictates their time evolution:

$$i\hbar\dot{x}_c = [x_c, V] = [x_c, y_c]\frac{\partial V}{\partial y_c} = il_b^2\frac{\partial V}{\partial y_c},$$
$$i\hbar\dot{y}_c = [y_c, V] = [y_c, x_c]\frac{\partial V}{\partial x_c} = -il_b^2\frac{\partial V}{\partial x_c},$$

where the potential was expanded to first order, and the final equality follows by expressing the center of orbit coordinates in terms of $\boldsymbol{\pi}$, $x_c = -\pi_y/eB$ and $y_c = \pi_x/eB$, which fail to commute $[\pi_x, \pi_y] = i\hbar eB$ (note that the mechanical

momentum $\mathbf{\Pi}$ is different than the momentum $\boldsymbol{\pi}$, which is defined in appendix A.1). What this says is that the orbits are moving in a direction perpendicular to the gradient of the potential V; i.e, along equipotentials. Since the disorder potential rarely stretches across the sample due to its nature, these orbits tend to stay localized around extrema of the potential, except along the edges, where extended equipotentials are possible.
To understand why the plateaus exist, we can see what happens when we decrease the magnetic field strength B, while keeping the electronic density constant. In this case, we see from equation (A.7) that some of the electrons living in the n^{th} Landau level have to go to the next level $n+1$, which, according to the form of the potential, localises these electrons around extrema of the potential. These localised electrons do not contribute to the conductivity/resistivity, which is therefore still being given by the filling factor $\nu = n$. As the $n+1$ level gets filled by more electrons, the localised electrons start to migrate from the extrema towards equipotential lines that stretch through the sample. This allows for percolation of these localised states across the sample, and a very rapid increase in the resistivity follows.

3.1.3 Fractional quantum-Hall Effect

In this section, we briefly discuss the Fractional QHE (FQHE). In this case the filling fraction $\nu \in \mathbb{Q}$ was observed at fractional values $\nu = 1/3,\ 1/5, \ldots$ at the lowest Landau level [17]. These observations can be explained when we consider the interactions between the electrons within the QH system.
One phenomonological description of the effect was given by Laughlin [18] through his guessed *Laughlin wavefunction*. To be able to describe it, it is convenient to introduce the complex coordinates

$$z = x - iy,$$
$$\bar{z} = x + iy.$$

We also work with (anti)holomorphic derivatives given by

$$\partial = \frac{1}{2}\left(\partial_x + i\partial_y\right),$$
$$\bar{\partial} = \frac{1}{2}\left(\partial_x - i\partial_y\right).$$

In the symmetric gauge, rotational symmetry is still present, and when we write down the annihilation operator acting on the lowest Landau level, we obtain the following differential equation for the single electron state's wavefunction

$$a\psi_L(z,\bar{z}) = -i\sqrt{2}\left(l_b\bar{\partial} + \frac{z}{4l_b}\right)\psi_L(z,\bar{z}) = 0.$$

The solutions are of the form

$$\psi_L(z,\bar{z}) = f(z)e^{-|z|^2/4l_b^2},$$

for some holomorphic function $f(z)$. By applying the operator $b = -i\sqrt{2}(l_b\partial + \bar{z}/4l_b)$, we can construct states with angular momentum quantum number m. The lowest state that is annihilated by both a and b is unique and given by $\psi_{L,m=0}(z,\bar{z}) \sim e^{-|z|^2/4l_b^2}$. It then follows that the wavefunction of a general lowest Landau state $|0,m\rangle$ is given by

$$\psi_{L,m}(z,\bar{z}) \sim \left(\frac{z}{4l_b}\right)^m e^{-|z|^2/4l_b^2}, \tag{3.6}$$

where we ommit normalization as it does not contribute to the argument. When we deal with N electrons, interacting through the central Coulomb potential $V(|\mathbf{r}_i - \mathbf{r}_j|)$ (between the i^{th} and j^{th} electrons), the wavefunction of the lowest Landau level takes the form

$$\Psi_L(z_1,\ldots,z_N,\bar{z}_1,\ldots,\bar{z}_N) = f(z_1,z_2,\ldots,z_N)e^{-\sum_{i=1}^N |z_i|^2/4l_b^2},$$

where the holomorphic function $f(z_1,z_2,\ldots,z_N)$ must be antisymmetric under exchange of particles (since we are dealing with electrons). We must assume that the separation between levels is higher than the potential, so that no mixing between levels can occur. This is where Laughlin boldly guessed the wavefunction for a filling fraction $\nu = 1/m$ to be of the form

$$\Psi_L(z_1,\ldots,z_N,\bar{z}_1,\ldots,\bar{z}_N) = \prod_{i<j}(z_i - z_j)^m e^{-\sum_{i=1}^N |z_i|^2/4l_b^2}, \tag{3.7}$$

where m is odd, which is clearly antisymmetric. A typical term of this wavefunction looks like

$$z_1^0 z_2^m z_3^{2m} \ldots z_N^{(N-1)m} e^{-\sum_{i=1}^N |z_i|^2/4l_b^2}.$$

The angular momentum for a single particle can be computed from equation (3.6) and is $\hbar m$, so the maximum angular momentum that a single electron can have in the Laughlin state is $M_{max} = \hbar m(N-1)$. On the other hand, the total angular momentum for N particles is

$$L_{tot} = \hbar m \sum_{k=1}^N k = \frac{\hbar m(N-1)N}{2}.$$

The probability of finding an electron at some $r = |z|$ can be computed from (3.6), and has the following form

$$|\psi_{L,m}(r)|^2 \propto r^{2m} e^{-r^2/2l_b^2}.$$

This peaks at $r_m = \sqrt{2m}l_b$. Therefore, the radius $R = \sqrt{2m(N-1)}l_b$ determines the size of the system, as all the other electrons will have angular momenta equal or smaller than that and will thus remain within an area given by $A = \pi R^2 = 2\pi m(N-1)l_b^2$. The area that one electron occupies is given by $\Delta A = \pi(r_{m+1}^2 -$

$r_m^2) = 2\pi l_b^2$. Hence, we find that the filling fraction of the Laughlin state is given by

$$\nu = \frac{\Delta A}{A} N = \frac{N}{m(N-1)} = \frac{1}{m}, \tag{3.8}$$

for $N \gg 1$. This is indeed a filling fraction that explains the first few values observed experimentally, as m is an odd integer. The Laughlin wavefunction provides a simple explanation for the appearance of plateaus at fractional filling factors, at least when we only consider the ground state of that QH system.

quantum-Hall effects show this behavior where macroscopic observables, which at first sight depend on an incredibly complicated set of microscopic parameters, are described by a simple integer in the end. In the next section, we will show, in parts, how this integer can be computed from a general framework.

3.2 Topological Characterizations

3.2.1 Berry connection

In this section, we discuss an important and universal concept that has a deep connection with the topological properties of quantum systems. It is the concept of the Berry phase, or more generally, the Berry connection.
We consider time-dependent Hamiltonians that are parametrized by a set of external, non-canonical degrees of freedom $\{\alpha_\mu(t)\}_{\mu=1}^K$, $H = H(\alpha_1(t), \alpha_2(t), \ldots, \alpha_K(t))$. According to the *adiabatic* theorem, if we vary the parameters "sufficiently" slowly in a degenerate quantum mechanical system, an arbitrary energy eigenstate with energy E_0 is restricted to live within the M-fold degenerate subspace of the Hilbert space $\mathbb{H}_M^{E_0}$. If the parameters of the Hamiltonian trace out a closed curve in parameter space, then we should end up in a state living in $\mathbb{H}_M^{E_0}$, i.e

$$\begin{aligned} |\phi\rangle \to \Lambda\, |\phi\rangle\,, \text{ where} \\ \Lambda : \mathbb{H}_M^{E_0} \to \mathbb{H}_M^{E_0}. \end{aligned}$$

We will ignore the time evolution phase factor in this contribution by setting $E_0 = 0$ and compute any additional phase that is picked up by this loop in parameter space.
Let the α-dependent ground states be denoted by $|n^j(\alpha)\rangle$, where $j = 1, \ldots, M$. The time evolution of these states is given by

$$|\phi_j(t)\rangle = U_{jk}(t)\, \left|n^k(\alpha)\right\rangle,$$

for some time dependent unitary operator $U(t) \in U(N)$. The time-derivative gives

$$\left|\dot{\phi}_j\right\rangle = \left(\frac{dU_{jm}}{dt}\, |n^m(\alpha)\rangle + U_{jm}(t) \frac{d\,|n^m(\alpha)\rangle}{dt}\right) = 0,$$

where the last equality is obtained by applying the Schrödinger equation with energy eigenvalue zero, and assuming that the time evolution is sufficiently slow so that the adiabatic theorem applies. We then have

$$\dot{U}_{jm} \left|n^m\right\rangle = -U_{jm} \left|\dot{n}^m\right\rangle = -U_{jm} \frac{\partial}{\partial \alpha^\mu} \left|n^m\right\rangle \frac{\partial \alpha^\mu}{\partial t}.$$

On the right hand side, we used that the time-dependence of the ground states is parametrized through the set $\{\alpha_i(t)\}_{i\in\mathbb{N}}$. We eliminate the unitary evolution operator on the right hand side to obtain

$$U^\dagger_{kj} \dot{U}_{jm} = -\left\langle n^k \right| \frac{\partial}{\partial \alpha^\mu} \left|n^m\right\rangle \frac{\partial \alpha_\mu}{\partial t} = i(\mathcal{A}_\mu)_{km} \frac{\partial \alpha^\mu}{\partial t}, \tag{3.9}$$

where we defined the non-Abelian *Berry connection*

$$(\mathcal{A}_\mu)_{ij} \equiv -i \left\langle n^i \right| \frac{\partial}{\partial \alpha_\mu} \left|n^j\right\rangle . \tag{3.10}$$

This is a $U(M)$ gauge connection over the parameter space manifold. Since it is a gauge connection, there is an ambiguity in its definition through the gauge choice of our basis. A change of basis $\left|n^l\right\rangle = \Lambda_{lm} \left|n^m\right\rangle$ induces the following change in the connection

$$\mathcal{A}'_\mu = \Lambda \mathcal{A}_\mu \Lambda^\dagger - \frac{\partial \Lambda}{\partial \alpha^\mu} \Lambda^\dagger,$$

which allows one to define the curvature tensor, or antisymmetric field strength tensor

$$F_{\mu\nu} = \frac{\partial \mathcal{A}_\mu}{\partial \alpha^\nu} - \frac{\partial \mathcal{A}_\nu}{\partial \alpha^\mu} - i[\mathcal{A}_\mu, \mathcal{A}_\nu]. \tag{3.11}$$

The solution to equation (3.9) is

$$U = \mathcal{P} \exp\left\{ -i \oint \mathcal{A}_\mu d\alpha^\mu \right\}, \tag{3.12}$$

where $\mathcal{P}$ stands for *path ordering*. The matrix U is called the *Berry Holonomy*.

If we consider a non-degenerate ground state for our Hamiltonian, the adiabatic theorem implies that the ground state remains the same and just picks up a phase factor $e^{i\lambda}$, $|\phi\rangle \to e^{i\lambda} |\phi\rangle$, which takes the role of the *Berry Holonomy*. In this case, we do not need to deal with any path ordering and the result is easily given by

$$\lambda = -\oint \mathcal{A}_\mu d\alpha^\mu,$$

where $\mathcal{A}_\mu$ is now an Abelian $U(1)$ gauge connection. The parameter λ is known as the *Berry phase*. It is possible to write down the Berry phase as a surface integral using Stoke's theorem. This yields

$$\lambda = -\int_S F_{\mu\nu} dS^{\mu\nu}, \tag{3.13}$$

where S is a surface enclosing the loop made by the line integral. This result is very elegant, as it relates to topological properties of the parameter space by way of a classification in terms of the *Chern number* $C \in \mathbb{Z}$, defined by

$$\int_S F_{\mu\nu} dS^{\mu\nu} = 2\pi C, \tag{3.14}$$

where $dS^{\mu\nu}$ is a shorthand notation for the wedge product of the differential forms, $d\alpha^\mu \wedge d\alpha^\nu$. In fact, in the language of differential geometry, this is nothing but an integral of the 2-form $F = F_{\mu\nu}\, d\alpha^\mu \wedge d\alpha^\nu$ over the relevant part of the parameter manifold $\mathcal{M}$,

$$C = \frac{1}{2\pi} \int_{\mathcal{M}} F.$$

3.2.2 Topological Invariants from the Berry Connection

We will first show a simple and useful example where the Berry phase plays an important role. It is obtained when considering the Hamiltonian of a spinor in a magnetic field. The second application of the Berry connection is one that is related to the QHE, and shows the topological properties of QH systems.

Spinor in a Magnetic Field

The Hamiltonian of a particle with in a magnetic field $\mathbf{B} = (B_x, B_y, B_z)$ is given by

$$H = \mu \boldsymbol{\sigma} \cdot \mathbf{B},$$

where $\boldsymbol{\sigma} = (\sigma_1, \sigma_2, \sigma_3)$ are Pauli matrices. It lives in a two-dimensional Hilbert space, and its energy eigenvalues are $\pm\mu B$, with $B = |\mathbf{B}|$. The eigenstates are given by

$$\begin{aligned} |0\rangle &= \begin{pmatrix} e^{-i\phi} \sin(\theta/2) \\ -\cos(\theta/2) \end{pmatrix}, \\ |1\rangle &= \begin{pmatrix} e^{-i\phi} \cos(\theta/2) \\ \sin(\theta/2) \end{pmatrix}. \end{aligned} \tag{3.15}$$

Note that we have made use of spherical coordinates (B, θ, ϕ) in magnetic field space, and that there is an ambiguity in the coordinate ϕ, as it does not define the states in (3.15) properly when $\theta = 0$. We pick the (nondegenerate) ground state $|0\rangle$ to compute the components of the Abelian Berry connection, which are $\mathcal{A}_\theta = -i \langle 0| \partial_\theta |0\rangle = 0$ and $\mathcal{A}_\phi = -i \langle 0| \partial_\phi |0\rangle = -\sin^2(\theta/2)$. This means that the only nontrivial component of the Berry curvature is $F_{\theta\phi} = -\frac{1}{2}\sin(\theta)$. In Cartesian coordinates[1], this is given by

$$F_{ij} = -\epsilon_{ijk} \frac{B^k}{2B^3}.$$

[1] $F_{ij} = \frac{\partial\theta}{\partial x^i} \frac{\partial\phi}{\partial x^j} F_{\theta\phi}$

There is a monopole of charge $-1/2$ sitting at the origin at $\mathbf{B} = 0$ and the field strength is rotationally symmetric. What happens there is that a level crossing appears. The two energy eigenvalues coincide, which makes the assumption of adiabatic evolution nullified and the Berry phase undefined. This characterizes the topology of the parameter space, as it contains a hole in the center. We relate this to the Chern number by taking the whole sphere as our closed surface. This results in

$$C = \frac{1}{4\pi}\int_{S^2} d\theta d\phi \sin(\theta) = \frac{1}{4\pi}\int_{S^2} d\Omega = 1.$$

TKNN Invariant and the QHE

We will now see how the Berry connection relates the quantisation of flux in the QHE to the topological properties of the quantum system. This example was very important in the history of topological quantum matter, as it is the first time that the Chern number was applied to describe properties of a topological insulator. The paper that set the ground for this idea was published by Thouless, Kohmoto, Nightingale and Den Nijs (TKNN) [19], which is why the topological invariant is called *TKNN*. In order to describe this relationship, we need an expression for the conductivity in terms of the current operators. This can be obtained through pertubartion theory (or linear response theory). The result is called the *Kubo* formula for the Hall conductivity:

$$\sigma_{xy} = i\hbar \sum_{n\neq 0} \frac{\langle 0| I_y |n\rangle \langle n| I_x |0\rangle - \langle 0| I_x |n\rangle \langle n| I_y |0\rangle}{(E_n - E_0)^2}, \tag{3.16}$$

where $|n\rangle$ is the n^{th} energy eigenstate and $\mathbf{I} = (I_x, I_y)$ is the current operator. It is a formula that describes the conductivity of a system through the linear response of the current operator when it is perturbed by a time dependent weak electric field.

The next step is to look at the band structure, and the Brioullin zone with edges identified with themselves, $(k_x, k_y) \in \mathbb{T}_2$, where $\mathbb{T}_2$ is a two-torus. This time, we define a Berry connection on the state space:

$$\mathcal{A}_i = -i \langle u_{\mathbf{k}}| \partial_{k_i} |u_{\mathbf{k}}\rangle . \tag{3.17}$$

Note that $|u_{\mathbf{k}}\rangle$ is the Bloch state defined previously in equation (2.8) through $\langle \mathbf{r}|u_{\mathbf{k}}\rangle = \psi_{\mathbf{k}}(\mathbf{r})$ (where the band index is implicit). Because of this construction, one can compute a Chern number C_a for each band by evaluating the Berry curvature at each band a. The Kubo formula for a non-interacting many-body system leads to a transverse conductivity

$$\sigma_{xy} = \frac{ie^2}{\hbar}\sum_a \int \frac{d^2k}{(2\pi)^2}\Big(\langle \partial_{k_y} u^a_{\mathbf{k}} | \partial_{k_x} u^a_{\mathbf{k}}\rangle - \langle \partial_{k_x} u^a_{\mathbf{k}} | \partial_{k_y} u^a_{\mathbf{k}}\rangle \Big). \tag{*}$$

The expression in between brackets is in fact the Berry curvature for the band a,

$$F^a_{xy} = -i \left\langle \partial_{k_y} u^a_{\mathbf{k}} \middle| \partial_{k_x} u^a_{\mathbf{k}} \right\rangle + i \left\langle \partial_{k_x} u^a_{\mathbf{k}} \middle| \partial_{k_y} u^a_{\mathbf{k}} \right\rangle . \qquad (**)$$

Plugging Eq. (**) into Eq. (*), we have

$$\begin{aligned} \sigma_{xy} &= -\frac{e^2}{\hbar} \sum_a \int \frac{dk_x dk_y}{(2\pi)^2} F^a_{xy} \\ &= \frac{e^2}{2\pi\hbar} \sum_a C_a, \end{aligned}$$

where we used equation (3.14) to get the second line. In the end, we obtain the famous *TKNN formula* for the Hall conductivity

$$\sigma_{xy} = \frac{e^2}{2\pi\hbar} C, \quad \text{where} \quad C \equiv \sum_a C_a. \qquad (3.18)$$

This establishes the topological aspect of the QHE, and gives an intuitive reason for the fact that the quantisation of the Hall conductivity is very robust.

So far we have seen how the Chern number characterizes the topological properties of a particle with spin, in a magnetic field, and also of QH systems. In the next section, we will look at other kinds of characterizations through a simple example from the class of topological superconductors.

3.2.3 Kitaev Chain

A simple model that displays topological properties is the 1D Kitaev chain. It is a tight-binding model that includes superconductivty in a system of spinless fermions. The Hamiltonian is given by

$$\mathcal{H} = -\mu \sum_j c_j^\dagger c_j - t \sum_j (c_j^\dagger c_{j+1} + c_{j+1}^\dagger c_j) + \sum_j (\Delta c_j^\dagger c_{j+1}^\dagger + \Delta^* c_{j+1} c_j), \qquad (3.19)$$

where t is the hopping strength, μ the chemical potential and Δ the spinless pair potential, similar to the one obtained from equation (2.15).This Hamiltonian takes the following form in Fourier space

$$\begin{aligned} \mathcal{H} &= -\sum_k \Big[\mu + 2t\cos(k)\Big] c_k^\dagger c_k + \sum_k i\Delta \sin(k)(c_k^\dagger c_{-k}^\dagger - c_{-k} c_k), \\ \mathcal{H} &= -\frac{1}{2} \sum_k \begin{pmatrix} c_k^\dagger & c_{-k} \end{pmatrix} H(k) \begin{pmatrix} c_k \\ c_{-k}^\dagger \end{pmatrix} \end{aligned} \qquad (3.20)$$

with

$$H(k) = \begin{pmatrix} \mu + 2t\cos(k) & 2i\Delta\sin(k) \\ -2i\Delta\sin(k) & -\mu - 2t\cos(k) \end{pmatrix},$$

where we took Δ to be real for simplicity. Let us now apply a Bogoliubov transformation, given by

$$\begin{aligned} c_k &= \alpha_k d_k + \beta_k d_{-k}^\dagger, \\ c_{-k} &= \alpha_{-k} d_{-k} + \beta_{-k} d_k^\dagger, \end{aligned} \tag{3.21}$$

where the fermionic operator $d_k^\dagger$ creates a quasiparticle with momentum k that is a superposition of a particle and a hole. The coefficients α_k and β_k are subject to the constraints

$$\begin{aligned} |\alpha_k|^2 + |\beta_k|^2 &= 1, \\ \alpha_k \beta_{-k} + \beta_k \alpha_{-k} &= 0. \end{aligned}$$

We set $\alpha_k = \alpha_{-k}$ and $\beta_k = -\beta_{-k}$. In order to diagonalize the Hamiltonian, one must impose the following condition on these coefficients:

$$\frac{\alpha^*}{\beta_k} = \frac{\epsilon_k \pm \sqrt{\epsilon_k^2 + 4|\Delta_k|^2}}{2\Delta_k},$$

where $\epsilon_k = \mu + 2t\cos(k)$ and $\Delta_k = i\Delta\sin(k)$. We can then choose the following parametrization:

$$\begin{aligned} \alpha_k &= \sqrt{\frac{E_k + \epsilon_k}{2E_k}}, \\ \beta_k &= \frac{2\Delta_k}{\sqrt{2E_k(E_k + \epsilon_k)}}, \end{aligned}$$

where $E_k^2 = \epsilon_k^2 + 4|\Delta_k|^2$, such that the Hamiltonian takes the diagonal form

$$\mathcal{H} = -\sum_k E_k d_k^\dagger d_k + \sum_k \frac{2|\Delta_k|^2}{E_k + \epsilon_k}. \tag{3.22}$$

We can thus interpret the energy E_k as the excitation energy of a quasiparticle. It has different features, depending on the values of the parameters. Some of these can be seen in figure 3.2.
We clearly see a phase transition happening depending on the value of the chemical potential. This is a topological phase transition where zero modes (with $E_k = 0$) at the edges of the Brioullin zone (BZ) are identified. This phase transition happens at about $\mu = \pm 2t$. We can also see this when we compute the energy of a finite chain numerically. In order to do this, we take the Hamiltonian (3.19) and write it as

$$\mathcal{H} = \frac{1}{2} C^\dagger H_{BdG} C, \tag{3.23}$$

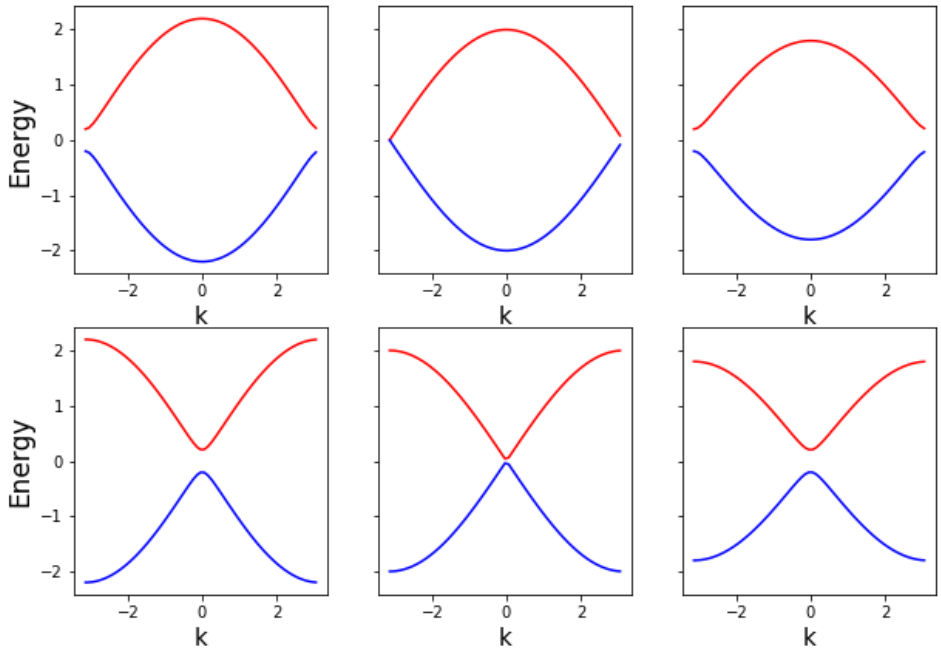

Figure 3.2: Energy of a quasiparticle excitation as a function of momentum in the BZ. In all three figures, we set $\Delta = t = 0.5$. a) $\mu = 1.2$, trivial phase. b) $\mu = 1$, critical point. c) $\mu = 0.8$, topological phase. The figures on the second row are plotted for negative values of the chemical potential.

where $C = (c_1, \ldots, c_N, c_1^\dagger, \ldots, c_N^\dagger)^T$. The *Bogoliubov de Gennes* Hamiltonian takes the form

$$H_{BdG} = \begin{pmatrix} \mu & -t & 0 & \ldots & 0 & 0 & \Delta & 0 & \ldots & 0 \\ -t & \mu & -t & \ldots & 0 & -\Delta & 0 & \Delta & \ldots & 0 \\ 0 & -t & \mu & \ldots & 0 & 0 & -\Delta & 0 & \ldots & 0 \\ \vdots & \vdots & \ddots & \ddots & \vdots & \vdots & \vdots & \ddots & \ddots & \vdots \\ 0 & 0 & \ldots & -t & \mu & 0 & \ldots & 0 & -\Delta & 0 \\ 0 & -\Delta & 0 & \ldots & 0 & -\mu & t & 0 & \ldots & 0 \\ \Delta & 0 & -\Delta & \ldots & 0 & t & -\mu & t & \ldots & 0 \\ 0 & \Delta & 0 & \ldots & 0 & 0 & t & -\mu & \ldots & 0 \\ \vdots & \vdots & \ddots & \ddots & \vdots & \vdots & \vdots & \ddots & \ddots & \vdots \\ 0 & 0 & \ldots & \Delta & 0 & 0 & 0 & \ldots & t & -\mu \end{pmatrix} \tag{3.24}$$

We plotted the energy as a function of chemical potential for a chain containing $N = 30$ sites in figure 3.3. Two regimes are observed: between $\mu = -2t$ and $\mu = 2t$, we can clearly see zero modes, plotted in black. This is the topological

phase, which we identified previously, with these modes living on the boundary of the system. There is a phase transition to a trivial phase for $|\mu| > 2t$, as can be seen from the completely gapped nature of the system beyond the critical points.

=

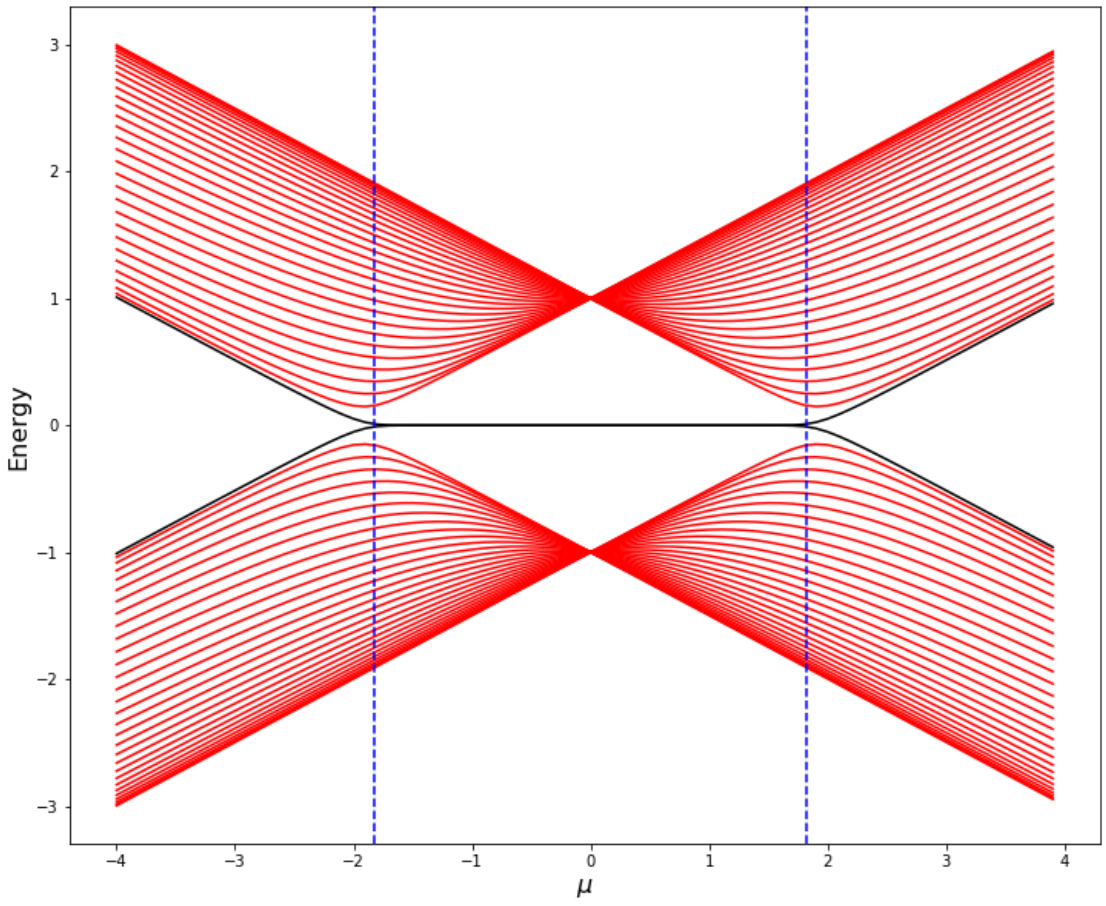

Figure 3.3: Energy levels of a $N = 30$ Kitaev chain, with $t = \Delta = 1$. The zero modes, plotted in black, appear between $\mu = -2$ and $\mu = 2$. Beyond this region, the system is gapped.

To understand the nature of these zero modes, we write down the fermion operators c_j in terms of *Majorana* operators:

$$\begin{aligned} c_j &= \frac{1}{2}(\gamma_{j_1} + i\gamma_{j_2}), \\ c_j^\dagger &= \frac{1}{2}(\gamma_{j_1} - i\gamma_{j_2}). \end{aligned} \tag{3.25}$$

These operators are self conjugate, $\gamma_{j_l} = \gamma_{j_l}^\dagger$, and obey the anticommutation relations

$$\{\gamma_{j_l}, \gamma_{k_m}\} = 2\delta_{jk}\delta_{lm}.$$

Partitioning the chain in this way, and using the parameters picked for our plots ($\Delta = t = 1$), we see that two unbound Majorana modes are isolated at the boundary of the chain, as shown in figure 3.4.

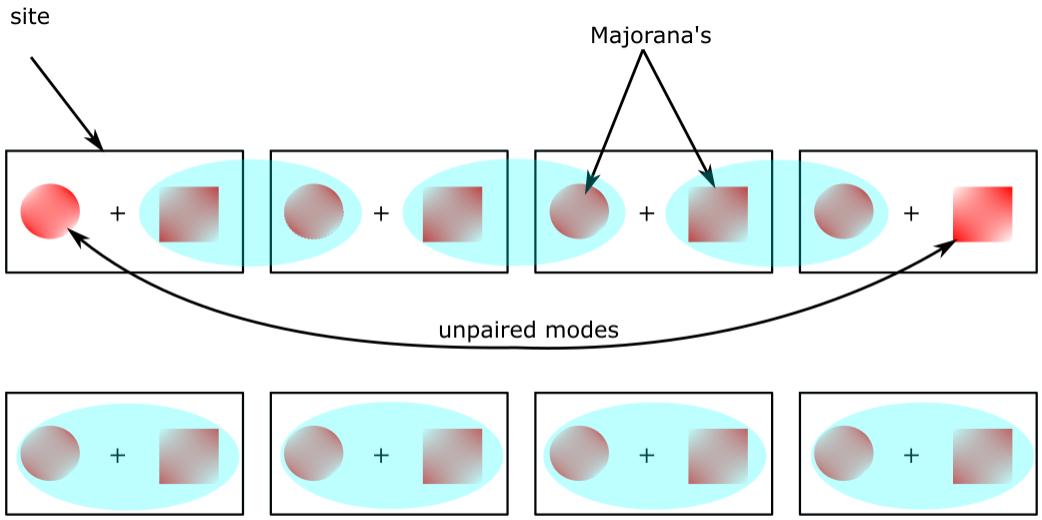

Figure 3.4: N=4 Chain, where each site hosts two Majorana modes and pairing is illustrated with a blue, shaded ellipse. a) Partition with unpaired Majorana's. b) Partition without unpaired Majorana's

The topological phase is thus characterized by the stable existence of Majorana zero modes at the boundary of the system. There is a distinction between the bulk of the system, which is gapped and the edge, which is gapless. These modes are in fact protected by the particle-hole symmetry that we previously talked about and the fact that there is no bulk zero mode. This is an example of the *Bulk-Edge correspondance*.
To see how the two phases can be regarded as topologically disctint sectors of the Hamiltonian, we use Kitaev's scheme [20] of calculating a *Majorana number* $Q = \pm 1$. It is 1 when there are Majorana modes at the edges and 0 when there are no unpaired modes. There is a certain quantity, called the *Pfaffian* of a matrix M, which comes in handy. It is defined by

$$\mathrm{Pf}^2(M) = \det(M). \tag{3.26}$$

In case M is antisymmetric, its eigenvalues come in pairs $\pm\lambda_n$, so that

$$\det(M) = \prod_n -\lambda_n^2,$$

and the Pfaffian takes the form

$$\mathrm{Pf}(M) = \pm i \prod_n \lambda_n.$$

Since the Kitaev chain has particle-hole symmetry, an antisymmetrized form of the Hamiltonian would keep the sign of the Pfaffian intact, as the energy eigenvalues come in pairs, $E_k = -E_{-k}$. The only exception happens when zero modes are present, which in the case of the present Hamiltonian happens when $k = 0$ and $\pm\pi$, as can be seen from equation (3.20). Hence, we can construct antisymmetrized matrices at those points through

$$\begin{aligned} H_{as}(0) &= \frac{i}{2}\begin{pmatrix}1 & 1\\ i & -i\end{pmatrix}\begin{pmatrix}\mu+2t & 0\\ 0 & -\mu-2t\end{pmatrix}\begin{pmatrix}1 & -i\\ 1 & i\end{pmatrix} = \begin{pmatrix}0 & \mu+2t\\ -\mu-2t & 0\end{pmatrix}, \\ H_{as}(\pi) &= \frac{i}{2}\begin{pmatrix}1 & 1\\ i & -i\end{pmatrix}\begin{pmatrix}\mu-2t & 0\\ 0 & -\mu+2t\end{pmatrix}\begin{pmatrix}1 & -i\\ 1 & i\end{pmatrix} = \begin{pmatrix}0 & \mu-2t\\ -\mu+2t & 0\end{pmatrix}, \end{aligned} \tag{3.27}$$

where the subscript *as* stands for "antisymmetric". These in turn give the following Pfaffians:

$$\begin{aligned} \mathrm{Pf}(H_{as}(0)) &= \mu + 2t \\ \mathrm{Pf}(H_{as}(\pi)) &= \mu - 2t \end{aligned} \tag{3.28}$$

The existence of zero modes thus allows for the Pfaffians to change sign when $\mu = \pm 2t$, in agreement with the band structure in figure 3.2. We can construct a unique topological invariant of the Hamiltonian by using both Pfaffians to get

$$Q = \mathrm{sign}(\mathrm{Pf}(H_{as}(0))\mathrm{Pf}(H_{as}(\pi))). \tag{3.29}$$

We see that $Q = -1$ corresponds to the topological phase and $Q = 1$ corresponds to the trivial phase. We should note that one cannot continuously deform $H_{as}(0)$ into $H_{as}(\pi)$ without changing topological sectors, i.e crossing a zero energy line. This means that the Hamiltonians at $k = 0$ and $k = \pi$ belong to different homotopy classes, characterized by a $\mathbb{Z}_2$ group.
Another way of constructing a topological invariant in this case can be achieved by noting some properties of the single-particle Hamiltonian $H(k)$, from equation (3.20). We note that it can be written as

$$H(k) = \mathbf{f}(k) \cdot \boldsymbol{\sigma},$$

where $\mathbf{f}(k) \equiv (0, -2\Delta \sin(k), \mu + 2t\cos(k))$. The image of the mapping from the Brioullin zone to the unit vector $\hat{\mathbf{f}}(k) = \mathbf{f}(k)/|\mathbf{f}(k)|$ lies on a unit circle on the (f_y, f_z) plane. Thus, we can define a winding number for the mapping and see how many times we circle over the origin as we go over half the Brioullin zone $k \in [0, \pi]$. This winding number is generally defined by $w = \oint d\theta/2\pi$, which in Cartesian coordinates gives

$$w = \frac{1}{2\pi}\oint dk \left(\frac{f_y}{|\mathbf{f}|^2}\frac{df_z}{dk} - \frac{f_z}{|\mathbf{f}|^2}\frac{df_y}{dk}\right). \tag{3.30}$$

It is not trivial to compute this in a straightforward way, but we can nonetheless argue that its value should be either 0 or ± 1. From the form of the vector $\mathbf{f}(k)$, we see that the trajectory is that of an ellipse which will either contain the origin or not, depending on whether it is in the topological or in the trivial phase, respectively. We plot three different ellipses in figure 3.5, which show the two regimes. The regimes where $\mu < 2t$ and $\mu > -2t$ (for $\mu > 0$ and $\mu < 0$) have winding numbers ± 1 respectively, but they still describe the same topological sector (with a different physical realisation when the chemical potential is negative). We thus find that the winding number gives an equivalent description of the topological properties of the Kitaev chain as that given by the Pfaffian construction.

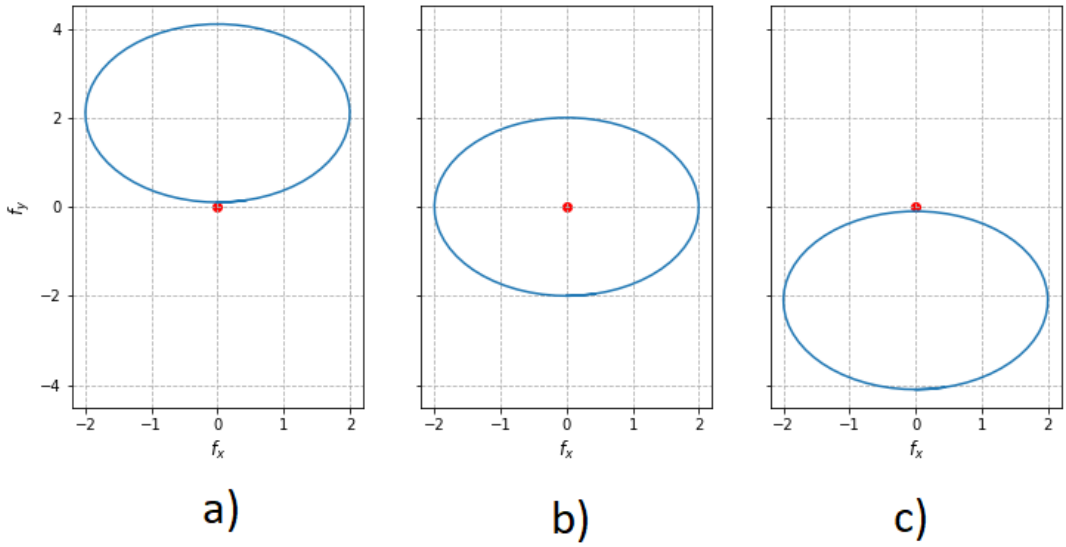

Figure 3.5: Ellipse in Hamiltonian space showing different regimes with the origin marked in red. a) $\mu > 2t$, $\mu > 0$. Origin outside of ellipse, $w = 0$: trivial regime. b) $|\mu| < 2t$. Origin inside the ellipse, which is traversed once, $w = \pm 1$: topological regime. c) $\mu < 2t$, $\mu < 0$. Origin outside of ellipse, $w = 0$: trivial regime again.

3.2.4 Tenfold Way

In the previous sections, we have discussed the topological properties of two specific models. The first was a 2D topological insulator giving rise to quantum-Hall states and which is characterized by a $\mathbb{Z}$ topological invariant, the *TKNN* number. The second one was a finite 1D topological superconductor, which gives rise to Majorana zero modes at the boundary of the system. It was characterized by a $\mathbb{Z}_2$ topological invariant, given either in terms of the Pfaffian of an antisymmetrized first-quantised Hamiltonian, or through the winding number of the map from the Brioullin zone to the Hamiltonian space.

There is a very general framework based on the works of Altland and Zirnbauer [21], which identifies the existence of topological phases in any number of spatial dimensions. It is based on the characterizations of symmetry protected topological states allowed by a set of Hamiltonians possessing the three discrete symmetries discussed in section 1. Altland and Zirnbauer noted in their works that there is a one-to-one correspondence between first quantised Hamiltonians possessing the three symmetries and the set of "large" symmetric spaces. A fundamental result obtained by the mathematician Élie Cartan [22][23] states that there exist ten such symmetric spaces. The possible symmetries allowed by combinations of charge conjugation $\mathcal{C}$ and time-reversal $\mathcal{T}$ are 10. This can be understood as follows:
Each Hamiltonian can be symmetric, antisymmetric or not symmetric at all under each of the two operations. To each of these cases, we attach the numbers $+1$, -1 and 0 respectively. This means that there are $3 \times 3 = 9$ combinations of the two. The third symmetry to look at is chirality, which can be seen as a combination of the two previous ones, as stated in the last part of section 2.2.3. It can also have three different values depending on the the value of the previous two. There is only one combination that makes its value ambiguous: when $\mathcal{T}$ and $\mathcal{C}$ are both 0. The chiral symmetry Σ can in this case be either 1 or 0. Hence, removing the case $(0, 0)$ from the nine possibilities and adding the two additional ones for Σ ends up giving 10 possible symmetry combinations of the Hamiltonian.

Figure 3.6 shows the ten symmetries, together with the group in which the time evolution operator $\exp(iHt/\hbar)$ lives, and the target space of the non-linear σ model describing the topological insulator (superconductor) on its $d-1$ boundary. The latter description goes beyond the focus of our section, but more information can be found in the article from Shinsei Ryu *et al.* [24]. In short, it reduces the problem of classifying the bulk topological insulator in d dimensions in terms of an *Anderson localization* problem in $d-1$ dimensions, where at long length-scales (large mean-free path), a non-linear σ model emerges. Tackling those Anderson localization problems allows one to define a topological term that depends on the type of non-linear σ model and the dimension of the boundary $d-1$. Arranging these topological terms together with the symmetries present results in the table given in figure 3.7.

Cartan label	T	C	S	Hamiltonian	G/H (ferm. NLσM)
A (unitary)	0	0	0	$\mathrm{U}(N)$	$\mathrm{U}(2n)/\mathrm{U}(n)\times\mathrm{U}(n)$
AI (orthogonal)	+1	0	0	$\mathrm{U}(N)/\mathrm{O}(N)$	$\mathrm{Sp}(2n)/\mathrm{Sp}(n)\times\mathrm{Sp}(n)$
AII (symplectic)	−1	0	0	$\mathrm{U}(2N)/\mathrm{Sp}(2N)$	$\mathrm{O}(2n)/\mathrm{O}(n)\times\mathrm{O}(n)$
AIII (ch. unit.)	0	0	1	$\mathrm{U}(N+M)/\mathrm{U}(N)\times\mathrm{U}(M)$	$\mathrm{U}(n)$
BDI (ch. orth.)	+1	+1	1	$\mathrm{O}(N+M)/\mathrm{O}(N)\times\mathrm{O}(M)$	$\mathrm{U}(2n)/\mathrm{Sp}(2n)$
CII (ch. sympl.)	−1	−1	1	$\mathrm{Sp}(N+M)/\mathrm{Sp}(N)\times\mathrm{Sp}(M)$	$\mathrm{U}(2n)/\mathrm{O}(2n)$
D (BdG)	0	+1	0	$\mathrm{SO}(2N)$	$\mathrm{O}(2n)/\mathrm{U}(n)$
C (BdG)	0	−1	0	$\mathrm{Sp}(2N)$	$\mathrm{Sp}(2n)/\mathrm{U}(n)$
DIII (BdG)	−1	+1	1	$\mathrm{SO}(2N)/\mathrm{U}(N)$	$\mathrm{O}(2n)$
CI (BdG)	+1	−1	1	$\mathrm{Sp}(2N)/\mathrm{U}(N)$	$\mathrm{Sp}(2n)$

Figure 3.6: The 10 possible symmetry characterizations of Hamiltonians. The first column assigns Cartan labels to each case. The second column shows the combination of symmetries present. The third column lists the group in which the time evolution operator $\exp(iHt/\hbar)$ lives. The last column lists the non-linear σ model describing the $d-1$ boundary theory.

	d												
Cartan	0	1	2	3	4	5	6	7	8	9	10	11	…
Complex case:													
A	$\mathbb{Z}$	0	$\mathbb{Z}$	0	$\mathbb{Z}$	0	$\mathbb{Z}$	0	$\mathbb{Z}$	0	$\mathbb{Z}$	0	…
AIII	0	$\mathbb{Z}$	0	$\mathbb{Z}$	0	$\mathbb{Z}$	0	$\mathbb{Z}$	0	$\mathbb{Z}$	0	$\mathbb{Z}$	…
Real case:													
AI	$\mathbb{Z}$	0	0	0	$2\mathbb{Z}$	0	$\mathbb{Z}_2$	$\mathbb{Z}_2$	$\mathbb{Z}$	0	0	0	…
BDI	$\mathbb{Z}_2$	$\mathbb{Z}$	0	0	0	$2\mathbb{Z}$	0	$\mathbb{Z}_2$	$\mathbb{Z}_2$	$\mathbb{Z}$	0	0	…
D	$\mathbb{Z}_2$	$\mathbb{Z}_2$	$\mathbb{Z}$	0	0	0	$2\mathbb{Z}$	0	$\mathbb{Z}_2$	$\mathbb{Z}_2$	$\mathbb{Z}$	0	…
DIII	0	$\mathbb{Z}_2$	$\mathbb{Z}_2$	$\mathbb{Z}$	0	0	0	$2\mathbb{Z}$	0	$\mathbb{Z}_2$	$\mathbb{Z}_2$	$\mathbb{Z}$	…
AII	$2\mathbb{Z}$	0	$\mathbb{Z}_2$	$\mathbb{Z}_2$	$\mathbb{Z}$	0	0	0	$2\mathbb{Z}$	0	$\mathbb{Z}_2$	$\mathbb{Z}_2$	…
CII	0	$2\mathbb{Z}$	0	$\mathbb{Z}_2$	$\mathbb{Z}_2$	$\mathbb{Z}$	0	0	0	$2\mathbb{Z}$	0	$\mathbb{Z}_2$	…
C	0	0	$2\mathbb{Z}$	0	$\mathbb{Z}_2$	$\mathbb{Z}_2$	$\mathbb{Z}$	0	0	0	$2\mathbb{Z}$	0	…
CI	0	0	0	$2\mathbb{Z}$	0	$\mathbb{Z}_2$	$\mathbb{Z}_2$	$\mathbb{Z}$	0	0	0	$2\mathbb{Z}$	…

Figure 3.7: Exhaustive classification of the possible realisations of topological insulators (superconductors) depending on the dimension of the theory and the symmetries present. 0 indicates triviality, i.e. no topological phase can exist in that situation. $\mathbb{Z}$ indicates the existence of topological phases labeled by an integer number. $\mathbb{Z}_2$ indicates the existence of a trivial phase and a topological phase. $2\mathbb{Z}$ indicates the existence of topological phases labelled by even integers.

4. Local Symmetries

In the previous chapters, we talked about the role of symmetries in condensed-matter systems and how they characterize their topological properties. In particular, we looked at some specific systems in which topological phases arise, and finally we briefly discussed the tenfold way, a general framework in which topological states can arise depending on the kind of global symmetry present in the system.
We now turn our attention to a new framework that deals with another kind of symmetry that a system can possess. Namely, we will discuss the role of local spacetime symmetries. To be clear, this is different from internal symmetries, which are described by local transformations acting differently on each spacetime point. These are generally referred to as gauge symmetries of the system, but can be found in the literature under the name of local symmetries. In this work, we will distinguish the two by referring to internal symmetries as gauge symmetries. On the other hand, the local spacetime symmetries are actual physical symmetries of the system. As we shall see in the next section, they can be seen as global spacetime symmetries on a restricted set of subdomains.
We will first go through a general description of these local symmetries, following the works of P. Schmelcher *et al.*. [25][26][27]. We will then try to find out whether this new framework allows for the existence of topological states.

4.1 Wave Propagation in One-Dimensional Locally Symmetric Potentials

4.1.1 Characterizing Local Symmetry: Invariant Currents

In this section, we describe generic quantum mechanical wave propagation through a spatial locally symmetric potential landscape. Some general results are presented, such as a new class of invariant nonlocal currents that provide a mapping between the various subdomains of the potential landscape, and also provide a generalization of the Bloch and parity theorems to the cases in which the global symmetries are reduced to local ones.
Let us begin with the derivation of two spatially invariant currents. The one-

dimensional Schrödinger equation can be written as

$$\psi''(x) + U(x)\psi(x) = 0 \tag{4.1}$$

where

$$U(x) \equiv \frac{2m}{\hbar^2}(E - V(x)) \tag{4.2}$$

with E being the energy of a particle of mass m and $V(x)$ the potential it is subjected to. A reflection about a point x_0 takes x to $-x+2x_0$, while a translation by an amount L takes x to $x + L$. We can define the linear transformation $F : \mathbb{R} \to \mathbb{R}$ that takes into account both actions:

$$x \mapsto \overline{x} = \alpha x + \beta \tag{4.3}$$

with

$$\boxed{\begin{array}{l}\alpha = -1 \text{ and } \beta = 2x_0 \rightarrow \text{ reflection;} \\ \alpha = 1 \text{ and } \beta = L \rightarrow \text{ translation.}\end{array}}$$

For any domain $D \subset \mathbb{R}$ where the potential U is symmetric under this transformation, one can write down the two following nonlocal currents in the subdomain D:

$$Q = \frac{1}{2i}\left[\alpha\psi(x)\psi'(\overline{x}) - \psi'(x)\psi(\overline{x})\right], \tag{4.4}$$

$$\tilde{Q} = \frac{1}{2i}\left[\alpha\psi^*(x)\psi'(\overline{x}) - \psi'^*(x)\psi(\overline{x})\right]. \tag{4.5}$$

The first of these is obtained by transforming equation (4.1) with F, multiplying the transformed equation by $\psi(x)$, equation (4.1) by $\psi(\overline{x})$ and subtracting the two. Since the transformation now acts on the domain D, the potential terms cancel each other and the result is expressed as

$$\frac{d}{dx}\left[\alpha\psi(x)\psi'(\overline{x}) - \psi'(x)\psi(\overline{x})\right] = 0,$$

leading to the constant Q. $\tilde{Q}$ is obtained similarly by taking the complex conjugate of equation (4.1).
These two nonlocal currents in subdomain D are linked to the globally conserved current through

$$\alpha\left(|\tilde{Q}|^2 - |Q|^2\right) = J^2, \tag{4.6}$$

where

$$J = \frac{1}{2i}\left[\psi'(x)\psi^*(x) - \psi'^*(x)\psi(x)\right]$$

is the globally conserved quantum mechanical probability current.
One can write the two currents as a matrix equation

$$2i\begin{pmatrix} Q \\ \tilde{Q} \end{pmatrix} = \begin{pmatrix} \alpha\psi(x) & -\psi'(x) \\ \alpha\psi^*(x) & -\psi'^*(x) \end{pmatrix}\begin{pmatrix} \psi'(\overline{x}) \\ \psi(\overline{x}) \end{pmatrix}.$$

Taking the inverse of this matrix yields an expression for the transformed wave functions:

$$\begin{aligned} \psi(\overline{x}) &= \frac{\tilde{Q}}{J}\psi(x) - \frac{Q}{J}\psi^*(x), \\ \psi'(\overline{x}) &= \alpha\left(\frac{\tilde{Q}}{J}\psi'(x) - \frac{Q}{J}\psi'^*(x)\right), \end{aligned} \tag{4.7}$$

where it is assumed that the global probability current J is nonzero. This result shows how the wavefunctions at different domains, where the realisation of the symmetry $U(x) = U(\overline{x})$ is present, can be mapped to each other through the use of the newly found nonlocal currents. One can also see this as a generalization of the Bloch and parity theorems to cases where the global symmetries are now only realized locally. The invariant Q is the symmetry breaking term, which is also referred to as the *remnant* of the broken global symmetry. When it is equal to zero, we recover the usual Bloch and parity theorems. The wavefunctions then become eigenfunctions of the operator F with eigenvalues $\tilde{Q}/J$ or $\alpha\tilde{Q}/J$ for $\psi'(x)$. It follows from equation (4.6) that for reflection symmetry, $\alpha = -1$, $\tilde{Q} = J = 0$, meaning that the only cases where there is a global parity symmetry is when the probability current is null everywhere. This is the scenario for bound states or scattering states with symmetrically incoming waves about the mirror axis. For translations ($\alpha = 1$), equation (4.6) says $|\tilde{Q}/J| = 1$, meaning that the eigenvalue is a unit complex number, in agreement with being the eigenvalue of the translation operator.

Consider now a realization of local symmetry in N different spatial subdomains D_n, where $n = 1, \ldots, N$. The potential is globally not symmetric under the operator F. However, we do have a local realization of the symmetry, $U_n(\overline{x}) = U_n(x)$ for $x \in D_n$, i.e the symmetry is realized in each subdomain. Examples of such potentials are shown in figure 4.1. Following the previous analysis in each subdomain D_n, a number of invariant currents, also labelled by n, exist. By applying equation (4.6) in each D_n, the currents are subjected to the following constraint:

$$|\tilde{Q}_1|^2 - |Q_1|^2 = |\tilde{Q}_2|^2 - |Q_2|^2 = \cdots = |\tilde{Q}_N|^2 - |Q_N|^2 \tag{4.8}$$

These constants then provide a way to map the wavefunctions between the different subdomains where the local symmetries are realized.

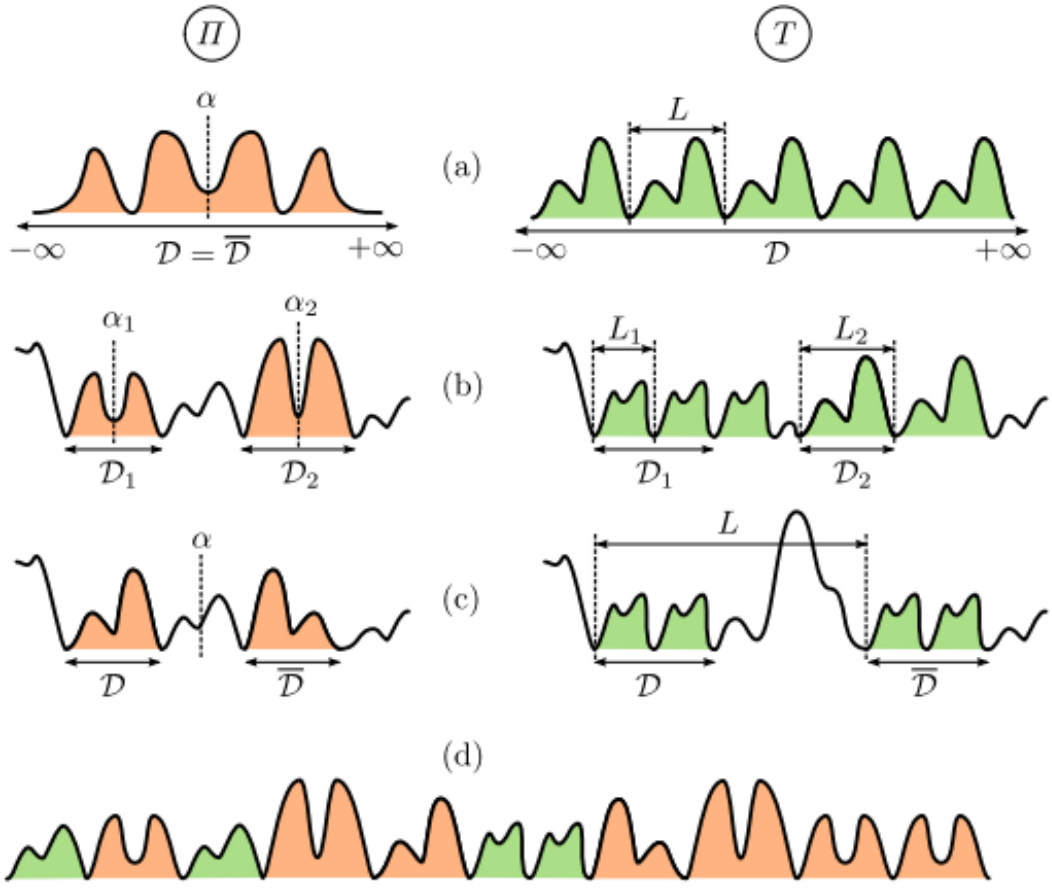

Figure 4.1: Different realizations of locally symmetric potentials. Π refers to reflection symmetry through axes $\alpha's$ and T refers to symmetries under translations by L's. The symmetry operations map a domain $\mathcal{D}$ to $\overline{\mathcal{D}}$. a) Global Symmetry, b) Nongapped Local Symmetry, c) Gapped Local Symmetry, d)Completely Locally Symmetric Potential. Figure taken from Ref. [27].

4.1.2 A More General Approach

Local Symmetry Basis

In this section, a general approach to construct eigenstates of the local symmetry operator is considered. Solutions of equation (4.1) can be written as superpositions of two linearly independent basis wave functions $\phi_1(x)$ and $\phi_2(x)$. The same procedure to construct the invariant currents derived previously allows now for eight different currents, depending on whether one mixes the two basis functions

or not. These are given by

$$\begin{aligned} Q_{mn} &= \frac{1}{2i}\Big[\alpha\phi_m(x)\phi'_n(\overline{x}) - \phi'_m(x)\phi_n(\overline{x})\Big], \\ \tilde{Q}_{mn} &= \frac{1}{2i}\Big[\alpha\phi^*_m(x)\phi'_n(\overline{x}) - \phi'^*_m(x)\phi_n(\overline{x})\Big], \end{aligned} \tag{4.9}$$

where $m, n \in \{1, 2\}$. In addition to these, we also have the conserved currents (only in the case of translation symmetry) corresponding to the m^{th} solution:

$$J_m = \frac{1}{2i}\Big[\phi^*_m(x)\phi'_m(x) - \phi'^*_m(x)\phi_m(x)\Big]. \tag{4.10}$$

A similar relation as equation (4.6) exists between the three expressions:

$$|\tilde{Q}_{mn}|^2 - |Q_{mn}|^2 = J_m J_n. \tag{4.11}$$

We can write the first line of equation (4.9) in matrix form as

$$\begin{pmatrix} Q_{11} & Q_{12} \\ Q_{21} & Q_{22} \end{pmatrix} = \frac{1}{2i}\begin{pmatrix} \phi_1(x) & \phi'_1(x) \\ \phi_2(x) & \phi'_2(x) \end{pmatrix}\begin{pmatrix} \alpha & 0 \\ 0 & -1 \end{pmatrix}\begin{pmatrix} \phi'_1(\overline{x}) & \phi'_2(\overline{x}) \\ \phi_1(\overline{x}) & \phi_2(\overline{x}) \end{pmatrix}. \tag{4.12}$$

Multiplying both sides by the inverse of the first matrix on the right hand side, and then transposing, yields

$$\begin{aligned} \begin{pmatrix} \alpha\phi'_1(\overline{x}) & \alpha\phi'_2(\overline{x}) \\ -\phi_1(\overline{x}) & -\phi_2(\overline{x}) \end{pmatrix} &= \frac{2i}{\mathcal{W}}\begin{pmatrix} -\phi'_2(x) & -\phi'_1(x) \\ -\phi_2(x) & \phi_1(x) \end{pmatrix}\begin{pmatrix} Q_{11} & Q_{12} \\ Q_{21} & Q_{22} \end{pmatrix} \\ \begin{pmatrix} \alpha\phi'_1(\overline{x}) & -\phi_1(\overline{x}) \\ \alpha\phi'_2(\overline{x}) & -\phi_2(\overline{x}) \end{pmatrix} &= \frac{2i}{\mathcal{W}}\begin{pmatrix} Q_{11} & Q_{21} \\ Q_{12} & Q_{22} \end{pmatrix}\begin{pmatrix} -\phi'_2(x) & -\phi_2(x) \\ -\phi'_1(x) & \phi_1(x) \end{pmatrix} \\ &= \frac{2i}{\mathcal{W}}\begin{pmatrix} Q_{21} & Q_{11} \\ Q_{22} & Q_{12} \end{pmatrix}\begin{pmatrix} -\phi'_1(x) & -\phi_1(x) \\ -\phi'_2(x) & \phi_2(x) \end{pmatrix}, \end{aligned}$$

where $\mathcal{W} \equiv \phi_1(x)\phi'_2(x) - \phi_2(x)\phi'_1(x)$ is known as the Wronskian. This provides a mapping between the wavefunctions in terms of the invariant currents, similar to the mapping obtained in the previous section.

$$\begin{aligned} \begin{pmatrix} \phi_1(\overline{x}) \\ \phi_2(\overline{x}) \end{pmatrix} &= \frac{2i}{\mathcal{W}}\begin{pmatrix} -Q_{21} & Q_{11} \\ -Q_{22} & Q_{12} \end{pmatrix}\begin{pmatrix} \phi_1(x) \\ \phi_2(x) \end{pmatrix}, \\ \begin{pmatrix} \phi'_1(\overline{x}) \\ \phi'_2(\overline{x}) \end{pmatrix} &= \frac{-2i}{\alpha\mathcal{W}}\begin{pmatrix} Q_{21} & Q_{11} \\ Q_{22} & Q_{12} \end{pmatrix}\begin{pmatrix} \phi'_1(x) \\ \phi'_2(x) \end{pmatrix}. \end{aligned} \tag{4.13}$$

We note that these results are general and independent of the the boundary conditions imposed on the wavefunctions, as opposed to equation (4.7), which does assume physical boundary conditions, as the global current J does not vanish, implying a situation with scattering states with one incoming wave.

We now proceed with the construction of a local symmetry basis (LSB) for the general local symmetry operator F. To this end, we need to transform the basis of linearly independent solutions $\{\phi_1(x), \phi_2(x)\}$ to a new basis given by

$$\boldsymbol{\chi}(x) = \begin{pmatrix} \chi_+(x) \\ \chi_-(x) \end{pmatrix} = \mathbf{S}\boldsymbol{\phi}(x), \tag{4.14}$$

where the two new wavefunctions satisfy the condition $Q_{\pm,\pm} = 0$, i.e

$$\alpha\chi_\pm(x)\chi'_\pm(\overline{x}) = \chi'_\pm(x)\chi_\pm(\overline{x}), \tag{4.15}$$

for all $x \in D$, with D being the subdomain where we have a realization of F-symmetry. The matrix $\mathbf{S}$ diagonalizes the matrix $\mathbf{Q}$ within D, where

$$\mathbf{Q} = \frac{2i}{\mathcal{W}} \begin{pmatrix} -Q_{21} & Q_{11} \\ -Q_{22} & Q_{12} \end{pmatrix}.$$

With this we can write

$$\boldsymbol{\chi}(\overline{x}) = \mathbf{Q}_\chi \boldsymbol{\chi}(x) = \mathbf{S}\mathbf{Q}\mathbf{S}^{-1}\boldsymbol{\chi}(x) = \begin{pmatrix} z_+ & 0 \\ 0 & z_- \end{pmatrix} \boldsymbol{\chi}(x). \tag{4.16}$$

$z_\pm$ are the eigenvalues of $\mathbf{Q}$. These can be computed through the characteristic equation $\det(\mathbf{Q} - z\mathbb{1}) = 0$, yielding

$$z^2 - \mathrm{Tr}(\mathbf{Q})z + \det(\mathbf{Q}) = 0.$$

We compute the determinant below:

$$\begin{aligned} \det(\mathbf{Q}) &= \frac{4}{\mathcal{W}^2}(Q_{21}Q_{12} - Q_{11}Q_{22}) \\ &= \frac{\alpha}{\mathcal{W}^2}\Big[\phi'_1(x)\phi'_1(\overline{x})\phi_2(x)\phi_2(\overline{x}) + \phi_1(x)\phi_1(\overline{x})\phi'_2(x)\phi'_2(\overline{x}) \\ &\qquad - \phi_1(x)\phi'_1(\overline{x})\phi'_2(x)\phi_2(\overline{x}) - \phi'_1(x)\phi'_1(\overline{x})\phi_2(x)\phi_2(\overline{x})\Big]. \end{aligned}$$

Since the currents are invariant throughout the domains of symmetry, we can choose a point satisfying $x_0 = \overline{x}_0$. We also note that the square of the Wronskian is given by a similar expression as the one in between brackets in the above equation, with the only difference that it is evaluated at $x = \overline{x}$. Bringing these two facts together, we evalutate the determinant to be

$$\det(\mathbf{Q}) = \alpha, \tag{4.17}$$

which is a nice a result as it permits the distinction between translation (+1) and reflection (-1). With this result, we have that the eigenvalues are given by

$$z_\pm = \frac{\mathrm{Tr}(\mathbf{Q})}{2} \pm \sqrt{\left(\frac{\mathrm{Tr}(\mathbf{Q})}{2}\right)^2 - \alpha} \tag{4.18}$$

With these, the diagonlizing matrix $\mathbf{S}$ can be evaluated by taking the inverse of the matrix of eigenvectors ($\mathbf{S}^{-1}$).
This basis permits the decoupled evaluation of the symmetry transformation, since $\chi_\pm$ are not mixed upon transformation by F. Indeed, acting with the operator $\hat{O}_F$, corresponding to F acting on elements of D, we have

$$\hat{O}_F \chi_\pm(x) = z_\pm \chi_\pm(x). \tag{4.19}$$

For mirror symmetry ($F = \Pi$), $z_\pm = \pm 1$, so that the wavefunctions $\chi_\pm$ correspond to the even or odd solutions of the Schrödinger equation with a locally Π-symmetric potential. For translation symmetry ($F = T$), three different cases are distinguished, depending on whether $\mathrm{Tr}^2(Q) > 4\alpha$ ($z_\pm \in \mathbb{R}$), $\mathrm{Tr}^2(Q) < 4\alpha$ ($z_\pm \in \mathbb{C}$ with $|z_\pm|^2 = \alpha$) or $\mathrm{Tr}^2(Q) = 4\alpha$ ($z_\pm = \alpha$). The first of these gives rise to real solutions, which could diverge at $\pm\infty$, so that they can only exist for finite locally symmetric subdomains D. The second one gives rise to propagating wave solutions with $z_\pm = e^{\pm ikL}$, where L is the translation amount and

$$kL = \arctan\left\{ \frac{2\sqrt{\left[\frac{\mathrm{Tr}(\mathbf{Q})}{2}\right]^2 - \alpha}}{\mathrm{Tr}(\mathbf{Q})} \right\}.$$

In the case of global translation symmetry, $\hbar k$ corresponds to the crystal momentum of a Bloch state. Finally, the third one corresponds to solutions which are periodic within the domain D, with period L ($z_\pm = 1$) or $2L$ ($z_\pm = -1$).

Global Basis and Physical Solutions

Having developed a scheme to construct a LSB, we now use it to construct a global basis. It is global in the sense that it can be done for arbitrary potentials with any combinations of Π and T symmetries. Different domains with different symmetries of the potential will be patched up together and described by a global basis of wavefunctions

$$\boldsymbol{\xi}(x) = \begin{pmatrix} \xi_1(x) \\ \xi_2(x) \end{pmatrix}$$

which need to be continuous and have continuous first derivatives, so that special care needs to be taken at interfaces between different symmetry regions. To this end we will use a labeling of the different domains as introduced by P. Schmelcher's *et al.* [27]. A given potential is decomposed into N domains $D_d = [x_{d-1}, x_d]$ of different symmetry realizations F_d, with $d = 1, \ldots, N$. Each of these D_d is divided into N_d cells $C_l^{(d)}$ of equal length, where $l = 1, \ldots, N_d$. Note that for Π symmetric regions, with the mirror axis centered about y_d, $N_d = 2$ and the two cells are $C_1^{(d)} = [x_{d-1}, y_d]$ and $C_2^{(d)} = [y_d, x_d]$. For a T symmetric region, each cell covers a period L_d. An example of such a decomposition is shown in figure 4.2.

The LSB solutions $\boldsymbol{\chi}^{(d)}(x)$ within a subdomain D_d, as constructed previously, are mapped to the different cells via

$$\boldsymbol{\chi}_l^{(d)}(F_d^{l-1}(x)) = [\mathbf{Q}_\chi^{(d)}]^{l-1}\boldsymbol{\chi}_1^{(d)}(x), \quad x \in C_1^{(d)}. \tag{4.20}$$

In other words, we can write the LSB in the l^{th} cell of a D_d symmetric region by

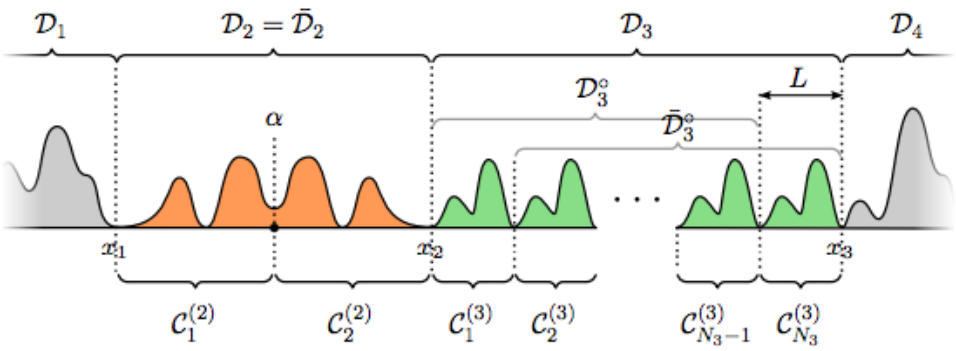

Figure 4.2: Example of a decomposition of a locally symmetric potential. The orange region $\mathcal{D}_2$ is a Π symmetric region with inversion centre α. It is decomposed into two cells of equal length. The green region is a T symmetric region with period L. It is decomposed into N_3 cells of length L. Figure extracted from [27]

mapping the LSB solution in the first cell through the application of the diagonal matrix $\mathbf{Q}_\chi^{(d)}$ $l-1$ times, i.e. through the application of the symmetry transformation F_d $l-1$ times. We proceed now in connecting the LSB of the D_d subdomain to the LSB of the D_{d+1} subdomain. This is done by trying to match the two solutions at the interface x_d with a *matching matrix* $\mathbf{M}_{d+1}$. For a potential which allows continuous derivatives of wavefunctions at the interface point x_d, These matching matrices are given by [27]

$$\mathbf{M}_{d+1} = \frac{1}{W_{+,-}^{d+1,d+1}} \begin{pmatrix} W_{+,-}^{d,d+1} & W_{+,+}^{d+1,d} \\ W_{-,-}^{d,d+1} & W_{+,-}^{d+1,d} \end{pmatrix}, \tag{4.21}$$

where

$$W_{r,s}^{i,j} \equiv \left[\chi_r^{(i)} \chi_s^{'\,(j)} - \chi_s^{(j)} \chi_r^{'\,(i)} \right]_{x=x_d}, \tag{4.22}$$

which stem from requiring the continuity of the functions and their first derivatives. Starting from some initial reference domain D_i, we set

$$\boldsymbol{\xi}^{(i)}(x) = \boldsymbol{\chi}^{(i)}(x). \tag{4.23}$$

Using the matching matrix, we obtain an expression for the global basis functions living in the domain D_d by successively applying the matching conditions above.

Hence, with $d > i$, the function is given by the LSB of that domain multiplied by a product of matching matrices:

$$\boldsymbol{\xi}^{(d)}(x) = \left\{ \prod_{h=i+1}^{d} \mathbf{M}_h \right\} \boldsymbol{\chi}^{(d)}(x) \equiv \mathbf{M}^{(di)} \boldsymbol{\chi}^{(d)}(x). \tag{4.24}$$

Using equation (4.20), we can express the LSB in the l^{th} cell of the D_d domain in terms of the first cell wavefunction

$$\boldsymbol{\chi}_l^{(d)}(x) = [\mathbf{Q}_\chi^{(d)}]^{l-1} \boldsymbol{\chi}_1^{(d)} \left(F_d^{-(l-1)}(x) \right), \quad x \in C_l^{(d)}, \tag{4.25}$$

so that the global basis functions can be written as

$$\begin{aligned} \boldsymbol{\xi}(x) = \boldsymbol{\xi}_l^{(d)}(x) &= \left\{ \prod_{h=i+1}^{d} \mathbf{M}_h \right\} [\mathbf{Q}_\chi^{(d)}]^{l-1} \boldsymbol{\chi}_1^{(d)} \left(F_d^{-(l-1)}(x) \right), \\ &= \mathbf{M}^{(di)} [\mathbf{Q}_\chi^{(d)}]^{l-1} \boldsymbol{\chi}_1^{(d)} \left(F_d^{-(l-1)}(x) \right), \\ &\equiv \mathbf{G}_l^{(di)} \boldsymbol{\chi}_1^{(d)} \left(F_d^{-(l-1)}(x) \right), \quad x \in C_l^{(d)}, \end{aligned} \tag{4.26}$$

at the celullar level. The *forward propagation matrix* $\mathbf{G}_l^{(di)}$ takes the LSB $\boldsymbol{\chi}^{(d)}(x)$ from the first to the l^{th} cell and then applies the matching from domain D_i to domain D_d.
Finally, a general symmetry operation F_d in domain D_d acting on the global basis functions is of the form:

$$\boldsymbol{\xi}^{(d)}(\overline{x}) = \mathbf{M}^{(di)} \mathbf{Q}_\chi^{(d)} \left[\mathbf{M}^{(di)} \right]^{-1} \boldsymbol{\xi}^{(d)}(x) \equiv \mathbf{Q}_\xi^{(d)} \boldsymbol{\xi}^{(d)}(x). \tag{4.27}$$

If one starts with $i = 1$ and $d = N$, $\boldsymbol{\xi}(x)$ is a global basis of functions for all of space covered by the locally symmetric potential. A physical solution is then given by

$$\psi(x) = c_1 \xi_1(x) + c_2 \xi_2(x), \tag{4.28}$$

where the coefficients c_1 and c_2 are determined from the boundary conditions imposed on the system at x_0 in D_1 and x_N in D_N.

4.2 Application of the Framework and Experimental Observations

In this section, we present two cases in which local symmetries have played a role. The first one is the actual observation of the nonlocal currents derived in the previous section, albeit in the case of a discrete system [28]. The second case explores the possibility to use local symmetries in a quantum network in order to control the storage and transfer of quantum states [29].

Local Symmetry in a photonic system To show the consequences of the existence of local symmetries, an experiment was conducted in 2019 [28], in which the team fabricated photonic waveguides that contained sites with either a global symmetry, local symmetries, or no symmetry at all. Such setups can be seen in figure 4.3.

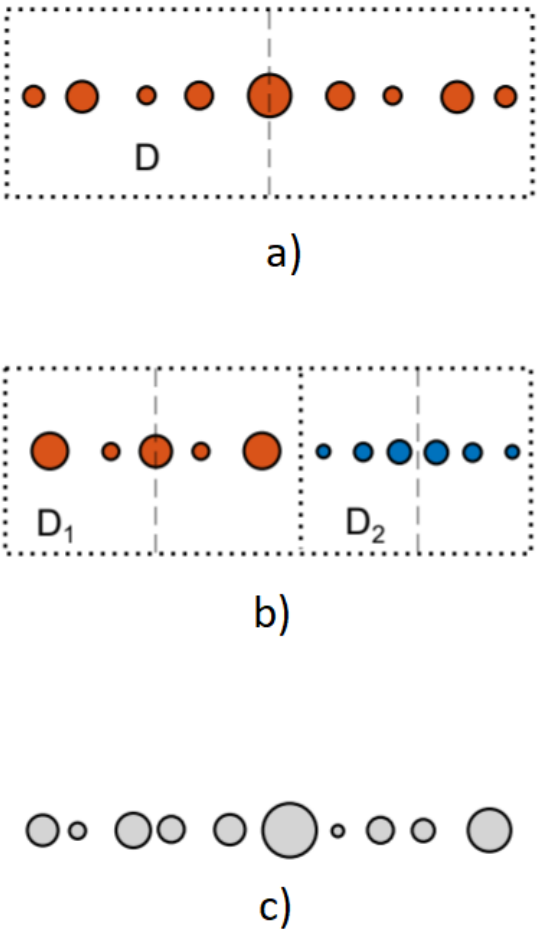

Figure 4.3: Example of discrete distributions of lattice sites. a) Global symmetry. b) Two regions with local symmetries. c) No symmetry. Figure taken from Ref. [28].

They used *femtosecond* direct laser writing in silica glass wafers [30] to construct their discrete lattices, where the symmetry distribution was incorporated in the waveguide site separation distances. In order to distinguish between the three cases, they injected a pulse into one of the sites, and measured the intensity pattern of fluorescent light from the neighboring sites. They then fitted a polynomial to the observed amplitude pattern in order to calculate the relevant derivatives and compute currents.
The total "nonlocal" charge within a region D is calculated using [31]

$$\Sigma_D = \sum_{n \in D} \langle \psi | n \rangle \langle \overline{n} | \psi \rangle \equiv \left\langle \psi_D \middle| \overline{\psi_D} \right\rangle, \tag{4.29}$$

for a general state $|\psi\rangle$, and where $\{|n\rangle\}$ is a basis in terms of lattice sites. The continuity equation relating this charge to its flow across the boundary of D is given by

$$\partial_z \Sigma_D = q_{\partial D}, \tag{4.30}$$

where z is the wave propagation direction, and the current can be calculated from [31] [28]:

$$q_{\partial D} = \pm 2(c_{b,b+1}|\psi_a||\psi_{b+1}| \mp c_{a,a-1}|\psi_b||\psi_{a-1}|), \tag{4.31}$$

where a and b respectively denote the sites at the start and end of the symmetry domain, and $c_{m,n}$ is a coupling between the waveguides at site m and at site n. The three cases depicted in figure 4.3 are distinguished as follows:

$$\begin{aligned} \text{global symmetry} &: \partial_z \Sigma_D = q_{\partial D} = 0, \\ \text{local symmetry} &: \partial_z \Sigma_D = q_{\partial D}, \\ \text{no symmetry} &: \partial_z \Sigma_D \neq q_{\partial D}. \end{aligned}$$

The results of their measurements show a good agreement between theoretical calculations and observations, as displayed in figure 4.4.

Storage and Transfer of Localised States The next application finds use for local symmetries in the storage and transfer of *compact localised states* (CLS) in a generic quantum network [29]. These are defined as eigenstates of the Hamiltonian that have vanishing amplitudes outside of a local region of space. Such states can arise in a variety of physical systems [32] due to, for example, lattice geometry resulting in destructive interference. The framework was applied to a decorated Lieb lattice (square-octagon lattice shown in figure 4.5) and the team has devised protocols to generate and manipulate (store and transfer) these CLS using local reflection symmetries in particular domains of the lattice. Their creation and transfer is achieved via amplitude phase-flips, or control, over time, of intersite couplings.

The Hamiltonian for a tight-binding "star" system, as shown on figure 4.5, is given by [29]

$$H = v_c \, |c\rangle \langle c| + \sum_{n=1}^{4} \Big[v_n \, |n\rangle \langle n| + J_n (|n\rangle \langle c| + |c\rangle \langle n|) \Big],$$

where v_n is the on-site potential, the index n denotes the four sites surrounding the central site and J_n is a coupling between the n^{th} central site. In the presence of local symmetries, this star system hosts CLS's. For example, as shown in figure 4.5, with $J_1 = J_2$ and $v_1 = v_2$, the state $|I\rangle = (|1\rangle - |2\rangle)/\sqrt{2}$ is an eigenstate

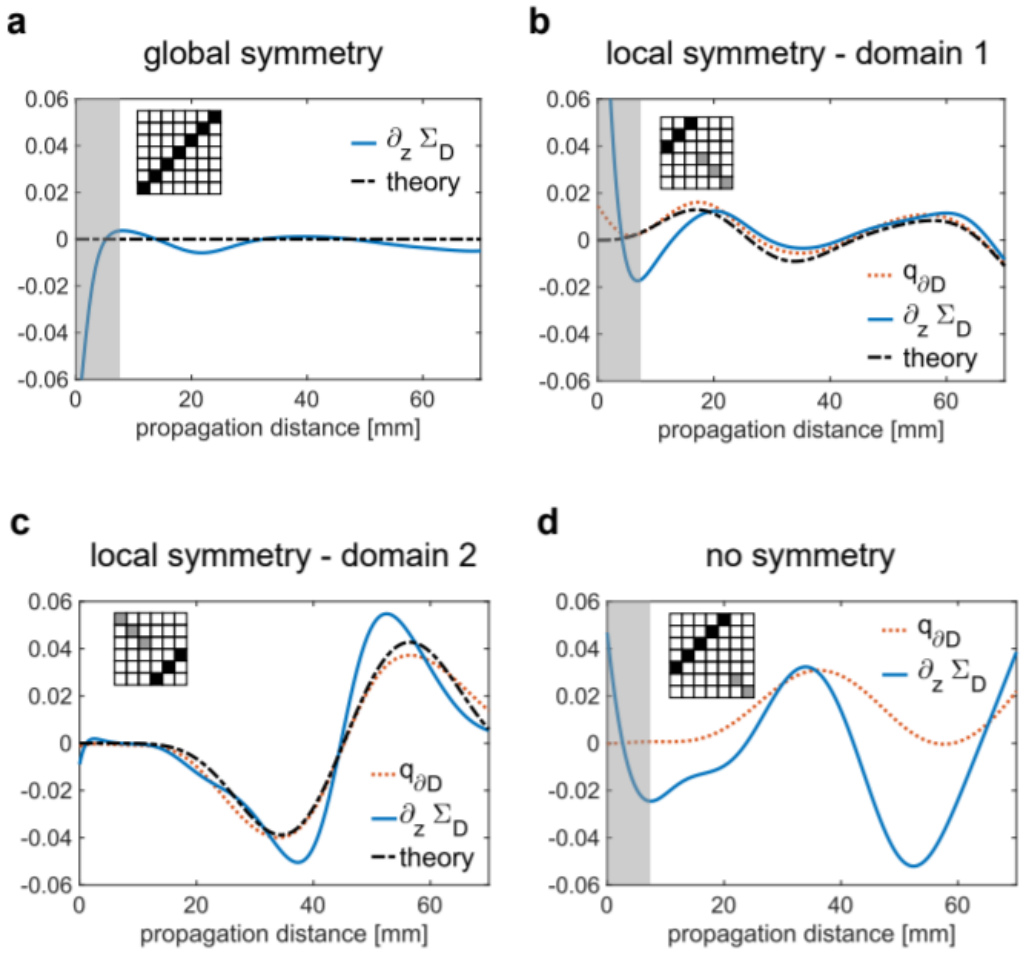

Figure 4.4: Comparison of theory and experiment. The square checkerboard represents the matrix that encodes the symmetry transformation in the basis of lattice sites (local inversion symmetry). Figure taken from Ref. [28].

with opposite sign amplitudes on sites 1 and 2, and 0 amplitude on the others. Its hopping rate also vanishes, thereby making it a CLS. It stays localised for an indefinite amount of time. It can be transferred to the state $|F\rangle = (|3\rangle - |4\rangle)/\sqrt{2}$, which has $J_3 = J_4$ and $v_3 = v_4$ using a modulation protocol devised by the authors of the paper [29]. More information on the protocol and its robustness can be found in the paper itself.

To summarize, we have studied the dynamics of wave propagation in one-dimensional locally symmetric potentials by characterizing the local symmetry through invariant currents. A general approach to the mapping of the wavefunction throughout

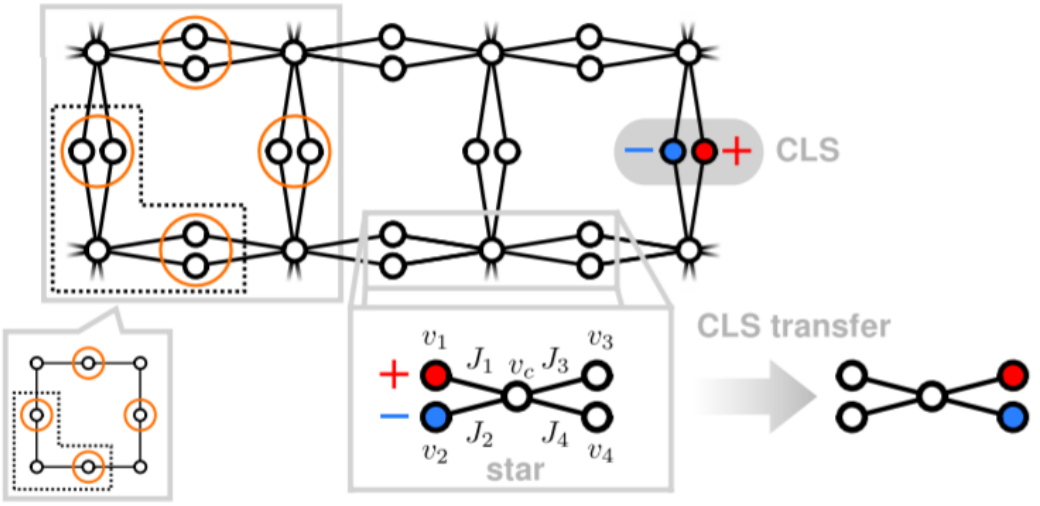

Figure 4.5: Decorated Lieb lattice, constructed from the original Lieb lattice (whose plaquette is shown in the lower lefthand inset) by replacing the encircled sites with dimers. Each such dimer can host one CLS with opposite amplitudes on the two dimer sites. The lower right-hand inset shows the isolated "star" subsystem functioning as a unit for the CLS transfer. Figure and caption taken from Ref. [29].

the region has been derived and some examples of the application of the framework have been provided.

5. Quasicrystals and Topology

In the first section of this thesis, we briefly discussed the features of periodic, *crystalline* systems, where the potential function in the general Hamiltonian (2.7) is structured according to a perfect translational symmetry in the lattice, $U(\mathbf{r}) = U(\mathbf{r} + \mathbf{R})$ ($\mathbf{R}$ being a Bravais lattice vector). These crystalline symmetries come in different forms and are mathematically characterised by space groups, of which the translational symmetry of the lattice forms one of the two subgroups, with the other being point groups of discrete rotations by an angle θ about some axis.
When a crystal belongs to a specific point group, it is expected to exhibit a particular difraction pattern when subjected to *X-ray* scattering experiments. According to the mathematical apparatus describing these symmetries, there are only a few 3D point groups allowed; namely a 2-, 3-, 4- and 6-fold rotational symmetry. This follows from what is called the *Crystallographic Restriction Theorem*. However, in 1982, Dan Shechtman observed diffraction patterns on an Al-Mg sample [5] that challenged the results of the theorem. The pattern corresponded to a forbidden 5-fold symmetry, which could not be understood at that time. Nowadays, it is known that the pattern was due to a solid matter arrangement that is different from what was commonly known as crystalline structure. It was initially thought to be a phase that stood somewhere between amorphous matter and ordered matter, but in 1992, the *Union of Crystallography* extended the notion of crystals to include the category of quasiperiodic systems. They proposed the following definition:

> *In the following by "crystal" we mean any solid having an essentially discrete diffraction diagram, and by "aperiodic" crystal we mean any crystal in which three-dimensional lattice periodicity can be considered to be absent [33].*

Hence instead of just having the periodicity of the atomic structure defining the solid phases of matter, it is the presence of long-range order that should be considered as an attribute.
In this chapter, after briefly introducing quasicrystals in general, we will give a description of the Fibonacci chain and understand its features through the perspective of a theory of local resonator modes [11]. We then give a brief overview of the Harper model. We will show that one can define a generalized potential with a parameter β, for which one can continuously move from the Fibonacci chain

model to the Harper model, rendering them topologically equivalent. The presence of topological order in the Harper model is then established by following the work of Kraus *et al.* [1][10]. After that, we focus on the Fibonacci chain and study it through a real-space renormalization procedure, and finally, we will study the effect of adding impurities on the chain.

5.1 Quasicrystals

Quasicrystals belong to the category of ordered condensed matter. This category can be broken down into two families: classical crystals, which have a periodic structure, and aperiodic crystals, which can be thought of as a generalisation of the former [34]. This comes from the fact that every quasiperiodic function can be described by a set of periodic ones. Mathematically speaking, periodic functions are a special case of quasiperiodic functions, which themselves are a special case of what is called *almost periodic* functions. The latter can be approximated by a Fourier series having a countable infinity of pairs of frequencies with an irrational ratio [35]. An explicit Fourier decomposition of an ordered lattice is given by

$$f(\mathbf{x}) = \sum_{\mathbf{k}} a_{\mathbf{k}} e^{i\mathbf{k}\cdot\mathbf{x}}, \tag{5.1}$$

where $\mathbf{k}$ is a vector in the reciprocal lattice. If $\mathbf{k}$ needs more basis vectors to span its space than the real lattice vectors, then a higher dimensional description of the reciprocal lattice is needed to have a periodic structure, which results in an aperiodic function in lower dimensional lattice. An example of a one-dimensional aperiodic function is given by

$$f(x) = A\cos(x) + B\cos(px),$$

with p being an irrational number. If we take this function to be obtained from a two dimensional domain space, in which the "second" dimension y is projected onto the x-axis by the linear relation $y = px$, then we obtain a periodic function in two-dimensions, namely

$$f(x, y) = A\cos(x) + B\cos(y).$$

One way to construct quasiperiodic lattices is through the use of what is called *Penrose tiling*. To obtain such a lattice with a 5-fold rotation symmetry, two basic "tiles" are used: a rhombus with angles 36° and 144°, and another rhombus with angles 72° and 108°. Each of the edges of the rhombi is given one or two arrows and there is a specific rule used to construct mosaics from these tiles. Namely, neighbouring edges must have the same amount of arrows and they must point in the same direction. An example of this two dimensions mosaic with 5-fold symmetry is shown in figure 5.1.

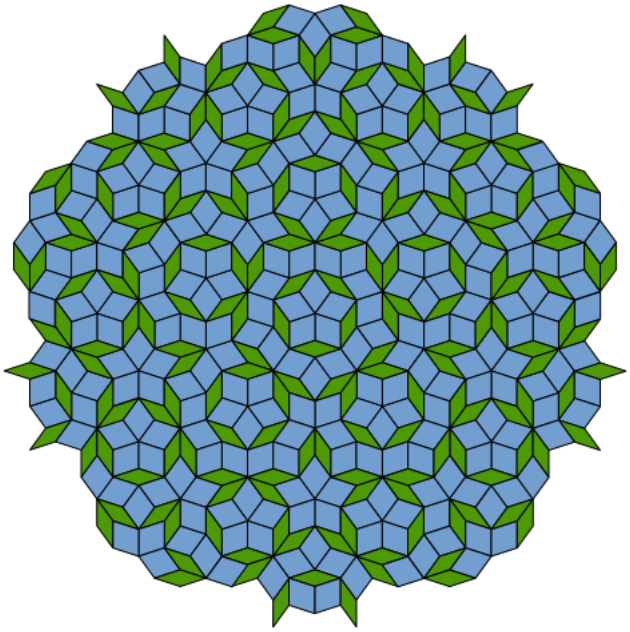

Figure 5.1: Fivefold symmetric Penrose tiled mosaic (figure taken from Wikipedia).

Properties of Quasicrystals It is known that for a classical periodic crystal, for which electronic wave functions are described by Bloch functions, electrons will have different behaviors depending on the band structure. In particular, whether the wavefunctions are localized or extended will determine the conduction properties of the material. Bloch functions have exactly the right structure to permit extended wavefunctions (which comes about from the modulation of the localized $u(x)$ by the wave e^{ikx}). On the other hand, amorphous (completely non-periodic) matter will only have a localized wavefunction possible at each atomic site n,

$$\psi_n(x) = A_n e^{-l_n|x|}.$$

This is due to the fact that the distribution of atoms, encoded in amplitudes A_n and localisation lengths l_n [36], is random throughout the material. This makes any two atomic sites uncorrelated. If a short-range correlation shows up in disordered matter, extended states start to appear. Since quasicrystals are neither completely periodic, nor disordered, it is expected that they would stand somewhere in between and have peculiar properties.
A classification can be made in terms of the spectrum of a discretised Hamiltonian (discretised Schrödinger equation):

$$(H\psi)_n = t\psi_{n+1} + t\psi_{n-1} + \lambda\big([(n+1)p] - [np]\big)\psi_n \tag{5.2}$$

where t is the hopping parameter (taken to be equal for all sites), λ is a measure of potential strength, $[x]$ denotes the nearest integer to x and p is taken to be the

golden ratio for a quasiperiodic system. In the mathematical discipline of measure theory and functional analysis, the Lebesgue's decomposition theorem states that the spectrum of a Borel measure can be decomposed into three parts (and mixtures of them)

$$\mu = \mu_P + \mu_{AC} + \mu_{SC}, \tag{5.3}$$

where μ_P is a *pure-point* measure, μ_{AC} is an *absolutely continuous* measure and μ_{SC} a *singularly continuous* measure. For example, the hydrogen atom's energy spectrum has both the pure-point part and an absolutely continuous part. On the other hand, only quasicrystals show the existence of a singular continuous energy spectrum [37]. According to the *gap-labelling* theorem, a relationship exists between the spectra of Fourier space and those of energy, which allows for a classification of aperiodic systems as shown in figure 5.2. This allows one to think about a correspondence between the kind of state (and hence wavefunction) and the kind of spectrum a quasiperiodic system has. It would mean that we would know whether we have localized or extended wavefunctions (or something in between, referred to as "critical" state).

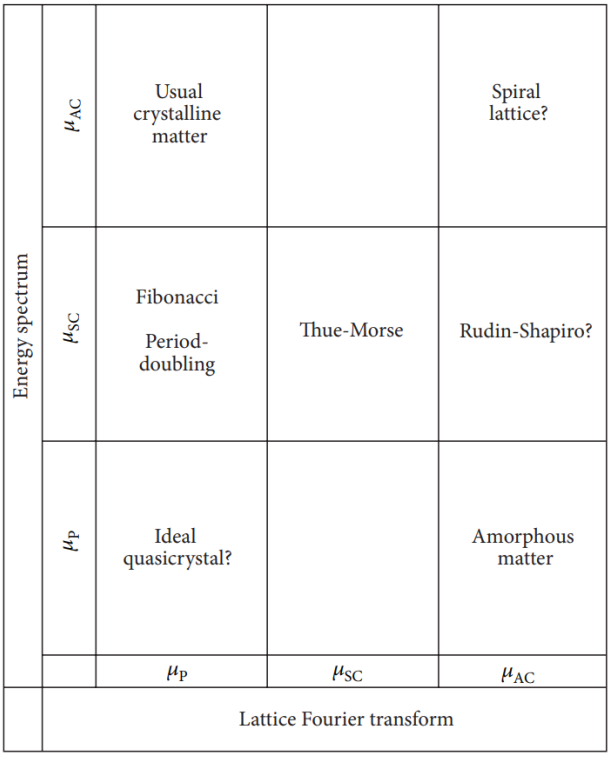

Figure 5.2: Classification of aperiodic systems according to the spectral measures of their Hamiltonian and of their lattice Fourier transform. Figure from ref. [38].

On the experimental side, many properties have been observed in quasicrystals, such as the very low thermal conductivity and peculiar electronic conductivities

[39] . The latter's dependence on temperature shows that it does not behave like a regular insulator does. In fact, as the temperature rises, its electrical conductivity grows linearly for high enough temperatures and as $\sqrt{T}$ for low temperatures (observed in an AlPdRe quasicrystal alloy [40]). On top of that, additional features including low friction coefficients, high hardness, corrosion resistance and superplasticity were also observed [6][41].

5.2 Fibonacci Chain

A large part of this thesis focused on studying impurities in the one-dimensional Fibonacci quasicrystal (FQC). We will therefore give a description of how this model is built and study its local symmetry structure. In general, there are two inequivalent one-dimensional tight-binding Fibonacci chains. Both of them are built on a chain with spatially periodic sites, but on which the on-site potentials, or the hopping integrals, are modulated by a Fibonacci sequence. As will be shown later, these two models are equivalent under this model's renormalization group. Finally, we study the effect of introducing an on-site impurity in the chain.

5.2.1 Fibonacci Sequence and Words

Before we start describing the models, we will briefly show how the Fibonacci sequence is built. An intuitive way of constructing it is through the so-called "rabbit sequence", in which a *Fibonacci word* is generated from a set of binary letters $\mathcal{A} = \{L, S\}$ (sometimes called a binary alphabet). An inflation rule is then imposed on each letter, at each step (called a *generation*):

$$\begin{aligned} S &\to L \\ L &\to LS \end{aligned} \tag{5.4}$$

The first few generations are shown in table 5.1.
The intuitive picture behind the name "rabbit sequence" comes about by considering the letter S to be a small rabbit and L to be a large one. On one hand, the small rabbit S grows to become a large rabbit L after one generation. On the other hand, the large rabbit will stay alive and produce an offspring S, resulting in the replacement rule $L \to LS$.
In a more mathematical language, the Fibonacci sequence $\{F_n\}_{n=0}^{\infty}$ is constructed as follows: we start with the first two numbers being 1 and construct the sequence recursively according to

$$F_n = F_{n-1} + F_{n-2}, \quad n \geq 2, \tag{5.5}$$

where F_n is called the n^{th} Fibonacci number. We note that at generation n, the size of the Fibonacci word $W_F^{(n)}$, generated by the inflation rule (5.4), is given by

$$|W_F^{(n)}| = F_n,$$

Generation	Word size	Word
0	1	S
1	1	L
2	2	LS
3	3	LSL
4	5	LSLLS
5	8	LSLLSLSL
6	13	LSLLSLSLLSLLS
7	21	LSLLSLSLLSLLSLSLLSLSL

Table 5.1: First seven generations of Fibonacci words. The word size follow the Fibonacci sequence, as can be seen in the middle column.

as can be seen in the middle column of table 5.1. This means that we can also write down a recursive scheme for each word generation:

$$W_F^{(n)} = W_F^{(n-1)} W_F^{(n-2)}, \quad n \geq 2. \tag{5.6}$$

One notable feature of the Fibonacci sequence is that the ratio between two consecutive generations asymptotically approaches the golden ratio:

$$\lim_{n\to\infty} \frac{F_n}{F_{n-1}} = \frac{1+\sqrt{5}}{2} \equiv \tau.$$

5.2.2 Tight-binding Models

The tight-binding, (nearest-neighbor) Hamiltonian, in both the hopping and on-site models, is given by

$$H = \sum_{i=1}^{N} \Big(v_i \left|i\right\rangle \left\langle i\right| + t_{i,i+1} \left|i\right\rangle \left\langle i+1\right| + \text{h.c.} \Big). \tag{5.7}$$

where, for a chain of generation M, the length is given by $N = |W_F^{(M)}|$ (boundary conditions are open or periodic depending on the model used). The two models are schematically depicted in figure 5.3.
Let us start with the on-site modulated FQC. The hopping strength is set to a constant $t_{i,i+1} = t$, and the on-site potential follows the Fibonacci sequence such that:

$$v_i = \begin{cases} V_w, & \text{when site } i \text{ falls on } L \\ V_s. & \text{when site } i \text{ falls on } S \end{cases} \tag{5.8}$$

depending on the site number. To illustrate features of this chain, we plot the energy spectrum in figure 5.4.

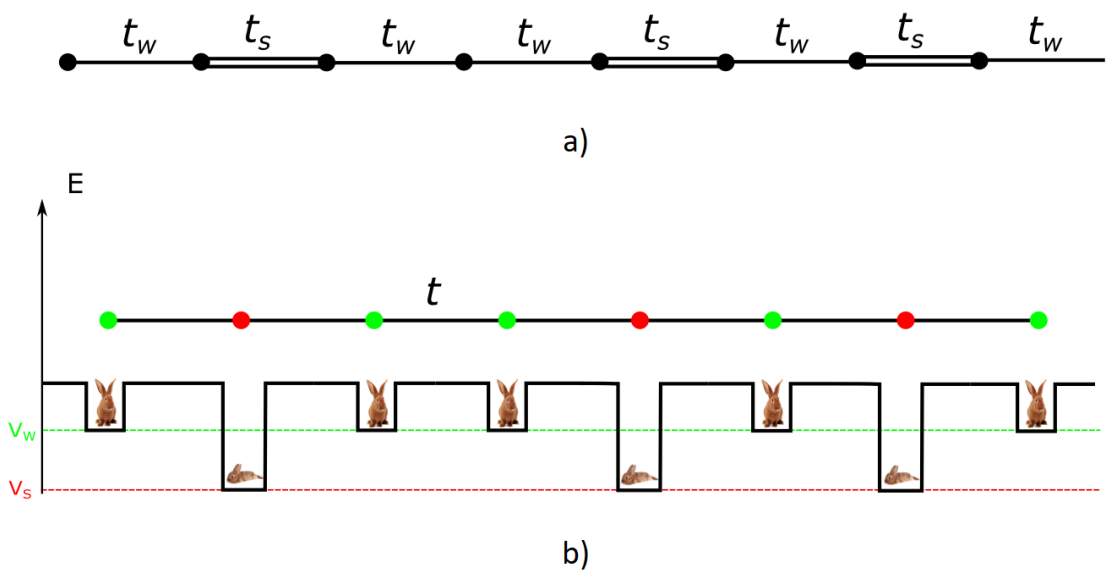

Figure 5.3: A depiction of the two tight-binding models. a) Hopping model, where a single bond represents a weak hopping and double bond represents a strong one. b) On-site model, where the weak and strong potentials ,V_W and V_S, are represented by wells in which the rabbits are happily resting.

The second model we look at is the hopping model. In this case, the on-site potential stays constant, $v_i = V$, at each site. The hopping parameters are modulated by the Fibonacci sequence and take on two different values:

$$t_{i,i+1} = \begin{cases} t_w, \\ t_s. \end{cases} \tag{5.9}$$

depending on i. In this case, the M^{th} generation chain has size $N = |W_F^{(M)}| + 1$, and there are $|W_F^{(M)}|$ links. The energy spectrum is plotted in figure 5.4.
Another way of obtaining this tight binding model is to consider an XY quantum spin chain without anisotropy on the Z quantization axis. The spin chain Hamiltonian is given by

$$H = \sum_{i=1}^{N-1} J_i \left[[S_i^x S_{i+1}^x + S_i^y S_{i+1}^y \right], \tag{5.10}$$

where the couplings J_i take on values J_L or J_S according to the i^{th} Fibonacci number. Performing a Jordan Wigner transformation gives:

$$\begin{aligned} S_j^x &= \frac{1}{2}\left(c_j^\dagger e^{i\pi \sum_{l<j} c_l^\dagger c_l} + c_j e^{-i\pi \sum_{l<j} c_l^\dagger c_l} \right), \\ S_j^y &= \frac{1}{2}\left(c_j^\dagger e^{i\pi \sum_{l<j} c_l^\dagger c_l} - c_j e^{-i\pi \sum_{l<j} c_l^\dagger c_l} \right). \end{aligned} \tag{5.11}$$

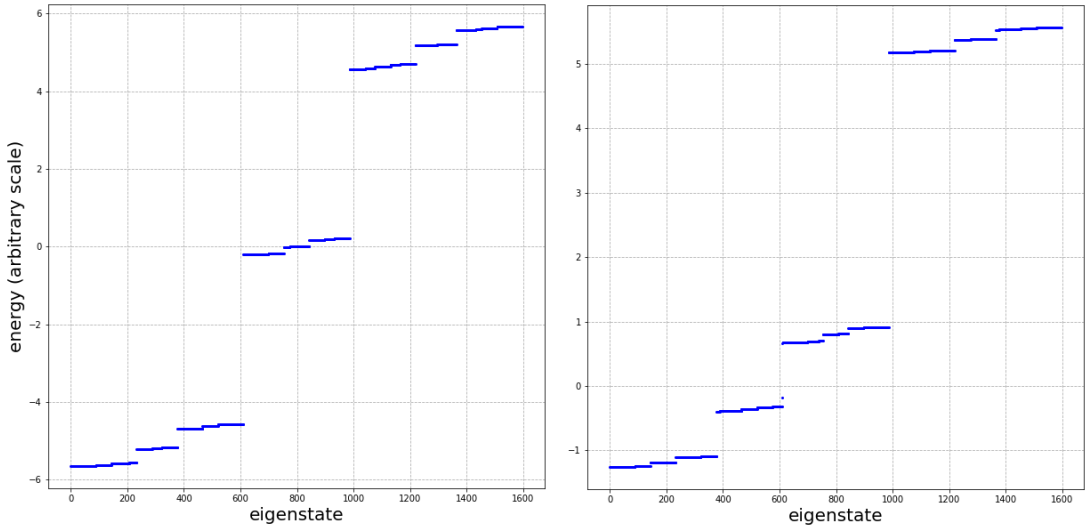

Figure 5.4: Spectrum of the 16$^{\text{th}}$ Fibonacci chain approximant. a) Hopping Model. b) On-site model. A trifurcating structure is clearly visible in both cases. We note that in the on-site model, the largest clusters are the two that result from the first decimation step in the renormalization procedure, as explained later in the text.

One then obtains the Hamiltonian

$$H = \sum_i t_i \left(c_i^\dagger c_{i+1} + c_i c_{i+1}^\dagger \right),$$

where $t_i = 2J_i$. This is the hopping model with on-site potential set to zero. Quantum spin chains with quasiperiodic modulation of the coupling parameter have been studied in ref. [42]. They have analysed different regimes under a renormalization group and plotted a phase diagram depicting them.

5.2.3 Local Symmetry Structure of the Fibonacci Chain

Fibonacci chains can be seen as a departure from a completely ordered crystal phase. However, it still has a lot of structure. According to the classification shown in figure 5.2, the FQC is not that far off from usual crystalline matter. In terms of the local symmetry framework, the infinite FQC has, in fact, a *completely locally symmetric* distribution of its components. Study of its structure has shown that the infinite Fibonacci word belongs to the class of *Sturmian word* [43]. These are words constructed out of a binary alphabet, in which there exists two kinds of possible palindromes (words with a reflection symmetry) of a certain length l. If l is even, then only one such unique palindrome exists and if it is odd, then there are two possible choices. For example, if we take for $l = 3$, we have two possibilities: LSL or SLS, while for $l = 4$, the only possible choice is $SLLS$, as we cannot have a SS configuration.

Some work has been done to link these local symmetries to the localisation of Hamiltonian eigenstates by means of a perturbative approach [11], and where an explanation for the appearance of edge states is also given within the same framework.
We can use the results from chapter four to derive the non-local currents. However, since our system is discrete, we follow the procedure developed in ref. [31]. The non-local currents resulting from the flow of the non-local charges, due to the presence of these local symmetries, are obtained when considering the time derivative of the expectation value of the non-local density operator

$$\hat{\sigma}_n \equiv |n\rangle \langle S(n)| = |n\rangle \langle \overline{n}| \,. \tag{5.12}$$

That is,

$$\begin{aligned} \partial_t \sigma_n &= \left(\partial_t \langle\psi|n\rangle\right) \langle\overline{n}|\psi\rangle + \langle\psi|n\rangle \left(\partial_t \langle\overline{n}|\psi\rangle\right) \\ &= i \langle\psi| H |n\rangle \psi_{\overline{n}} - i\psi_n^* \langle\overline{n}| H |\psi\rangle \\ &\equiv q_n^+ + q_n^-. \end{aligned}$$

The non-local currents $q_n^\pm$ are defined through the above equation and are obtained when plugging equation (5.7) on the RHS,

$$q_n^\pm \equiv i\psi_{n\pm1}^* t_{n\pm1,n}^* \psi_{\overline{n}} - i\psi_n^* t_{\overline{n},\overline{n\pm1}} \psi_{\overline{n\pm1}}. \tag{5.13}$$

They can be compared to the usual local currents, which in the discrete case are given by:

$$j_n^\pm \equiv i\psi_{n\pm1}^* t_{n\pm1,n}^* \psi_n - i\psi_n^* t_{n,n\pm1} \psi_{n\pm1}. \tag{5.14}$$

The rate of change of the total charge $\Sigma_{\mathbb{D}}^\psi$, defined by

$$\Sigma_{\mathbb{D}}^\psi \equiv \sum_{n\in\mathbb{D}} \sigma_n,$$

which flows out of a region $\mathbb{D}$ of local symmetry is given by the sum of the individual non-local currents through the continuity equation:

$$\partial_t \Sigma_{\mathbb{D}}^\psi = \sum_{n\in\mathbb{D}} (q_n^+ + q_n^-) \equiv Q_{\mathbb{D}}. \tag{5.15}$$

In order to construct an amplitude mapping relation, a dual current $\tilde{q}_n^\pm$ has to be introduced, which, contrary to the continuous case, is not naturally derived from the problem setup. It is given by

$$\tilde{q}_n^\pm \equiv i\psi_{n\pm1} t_{n\pm1,n} \psi_{\overline{n}} - i\psi_n t_{\overline{n},\overline{n\pm1}} \psi_{\overline{n\pm1}}. \tag{5.16}$$

In this case, when all the currents are nonzero, the amplitude mapping relation derived in equation (4.7) takes the discrete form

$$\psi_{\overline{n}} = \frac{1}{j_n^\pm} \left(q_n^\pm \psi_n - \tilde{q}_n^\pm \psi_n^* \right). \tag{5.17}$$

5.2.4 On-site Model and the Local Symmetry Theory of Resonator Modes

The on-site model can be analysed using a framework devised by Röntgen *et al.* [11], in which they have linked the real space local symmetries of the chain to the local symmetries of eigenstates' wavefunctions. This is done in a perturbative manner and provides an intuitive understanding of the spectrum, shown below, in figure 5.6 or in figure 5.4 for a larger chain. It also provides the possibility to control the occurence of edge states, as was shown in the paper by Röntgen *et al.*, with energies lying outside of the quasibands.

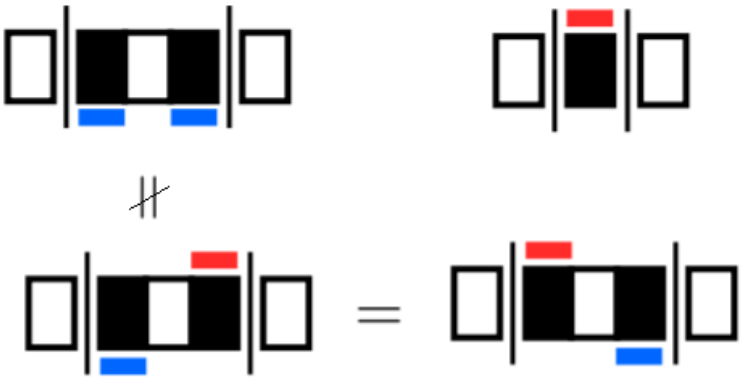

Figure 5.5: Examples of LRMs. The black/white large rectangles represent the "high/low" on-site potentials of the Fibonacci chain. The vertical lines represent the walls of a "cavity". The blue and red rectangles represent positive or negative values of the wavefunctions confined inside this cavity. Notice that the lower two modes are the same as they are both antisymmetric under parity. The upper left LRM has positive parity and is thus different than the ones below. Figure taken from ref. [11].

Local Resonator Modes In order to understand the link between real-space symmetries and wavefunction parities, building blocks that go under the name of Local Resonator Modes (LRM) are introduced. It is called as such because when one works perturbatively, the first few orders for the eigenfunctions all localise within a particular resonator in the chain. Examples of local resonators, with their modes, is shown in figure 5.5. The claim is that, in the regime of high contrast

$$c \equiv \frac{|V_S - V_L|}{t} \gg 1,$$

there is an almost one-to-one mapping between the two symmetries discussed above. This can be seen by looking at figure 5.6, where it is shown that the lo-

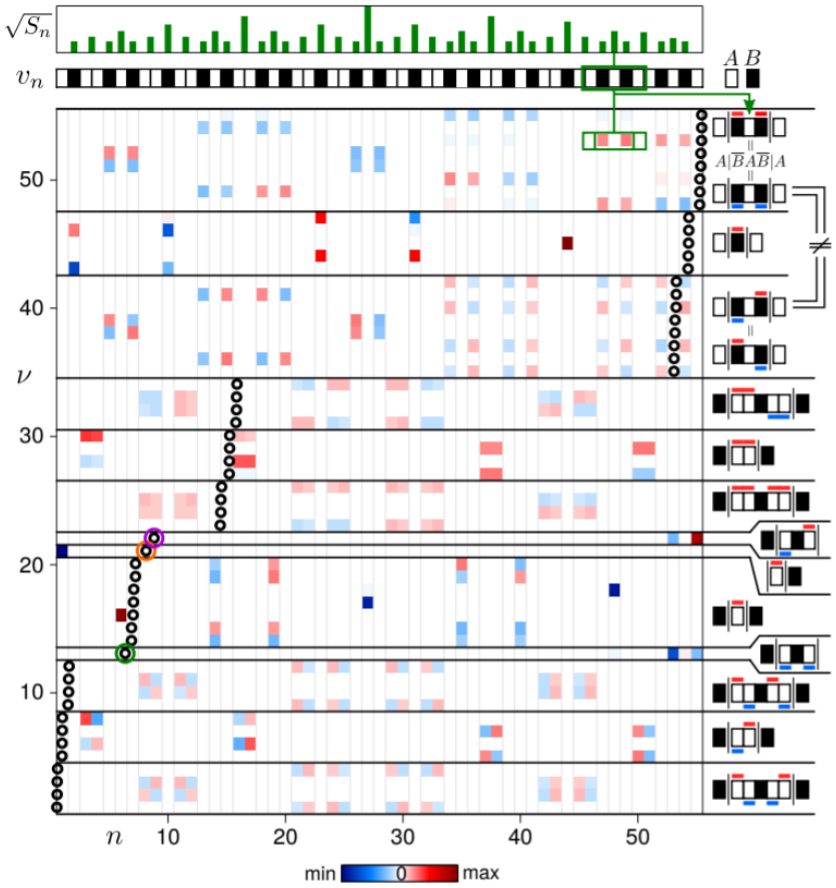

Figure 5.6: Eigenstate map of an on-site Fibonacci chain of generation 9, at high contrast c. The topmost figure quantifies the extent of a locally mirror symmetric region in the chain, in terms of $\sqrt{S_n}$, where S_n is the length of the mirror symmetric region. Below it is the Fibonacci chain in terms of the on-site potentials, labelled here by A and B. The small circles are the energies of each state (their axis is not included as it would have cluttered the figure), and each "quasiband" of energies is associated to a LRM, depicted on the right. We note that the edge modes' energies, depicted by the three colored circles, lie outside of the quasibands, where we see that they belong to a unique resonator structure, associated to cavity wall ending at the boundary. Figure taken from ref. [11].

cal resonator blocks, with their reflection symmetries, have modes that are either positive or negative under a parity transformation.
This establishes a very elegant organization of the bands in terms of these resonator structures. As one goes to lower contrast, this picture still holds but is hidden by the dressing of the wavefunctions in their delocalized, critical behavior. The relatively higher hopping parameter induces a mixing of the wavefunctions, which gives them more support at other sites of the chain, as can be seen in figure 5.7.

Understanding the fragmentation of the eigenstates for $c \gg 1$. In the regime $c \gg 1$, we can perform a perturbative treatment of the chain to understand why the wavefunction fragments itself and isolates into these resonator cavities. For simplicity, we set $V_S = V$ and $V_L = 0$. We rescale the Hamiltonian as $H' = H/V$ and write

$$H' = H'_0 + \frac{1}{c} H_I, \tag{5.18}$$

where $H'_0 = H_0/V$ is the matrix containing the Fibonacci modulated on-site potentials, rescaled by the on-site potential V and H_I has ones in the first upper and lower diagonals. Treating the second term as a perturbation of the first, we can expand the full states and energies perturbatively and make use of degenerate perturbation theory:

$$\begin{aligned} \left|\phi^{(i)}\right\rangle &= \left|\phi^{(i)}\right\rangle_0 + \lambda \left|\phi^{(i)}\right\rangle_1 + \lambda \left|\phi^{(i)}\right\rangle_2 + \dots \\ E^{(i)} &= E_0^{(i)} + \lambda E_1^{(i)} + \lambda E_2^{(i)} + \dots, \end{aligned}$$

where the index $i = 1, \dots, N$ denotes which one of the N states we are dealing with. This is because H_0 has only two highly degenerate eigenvalues. The procedure for obtaining the zeroth order states $\left|\phi^{(i)}\right\rangle_0$ is complicated for binary chains, as the degeneracies are only resolved at very high orders [44][45]. Röntgen *et al.* worked out the expression for the zeroth order states $\left|\phi^{(i)}\right\rangle_0$ up third order, and have also given an expression for the first-order states $\left|\phi^{(i)}\right\rangle_1$. They have shown that it localises either on sites labelled by L or by S (in their paper they called them A and B). They have also shown that the block of potential on which they localize is either of length 1 or length 2 (S, L, or LL). This explains the structure shown in figure 5.6. At high contrast, with corrections to the zeroth order being marginal, the fragmentation of these eigenstates is very strong.

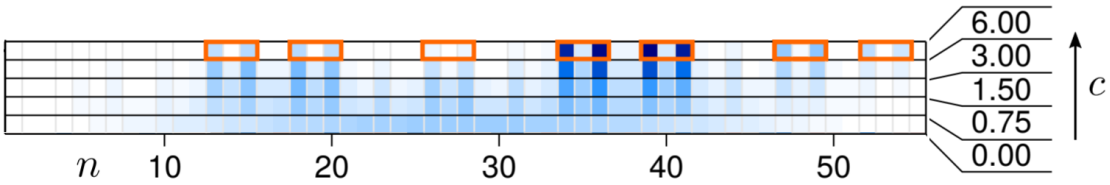

Figure 5.7: Dressing of one resonating mode at high contrast, as c becomes smaller. Figure taken from ref. [11].

5.3 Harper's Model and its Equivalence to the FQC

Harper's Model. In order to discuss the topological properties of the FQC, we introduce yet another model for aperiodic one-dimensional chains, the Harper

model. This model allows modulation of the on-site potential as well as the hopping parameter. We can describe both cases using the following second-quantised Hamiltonian:

$$H = \sum_n \left\{ \left[t + \lambda V_n^{(1)}(\phi) \right] c_n^\dagger c_{n+1} + \gamma V_n^{(2)}(\phi) c_n^\dagger c_n + \text{h.c.} \right\}, \tag{5.19}$$

where $V_n^{(2)}(\phi - \pi p) = V_n^{(1)}(\phi) = \cos(2\pi pn + \phi)$ are the the modulating functions in the diagonal and off-diagonal cases, respectively. The parameters λ and γ are their respective amplitudes, and p is an irrational number that characterises the quasiperiodic nature of the chain. Note that the chain can be composed of either fermionic or bosonic particles, but we take them to be fermionic in the subsequent discussions.

We start by describing the uniform hopping case, with only on-site modulation. This means we set $\lambda = 0$. We will describe the higher dimensional periodic realisation of the model by taking the phase parameter $\phi \equiv k$ to be an extra degree of freedom coming from the k^{th} Fourier component of a two-dimensional periodic Hamiltonian, called *ancestor Hamiltonian* [10]. Thus, we extend the fermionic operators to $c_{n,k} = \sum_m e^{-imk} c_{n,m}$, obeying

$$\{c_{n,m}, c_{n',m'}^\dagger\} = \delta_{nn'}\delta_{mm'}. \tag{5.20}$$

Summing over the new degrees of freedom, we can write down the ancestor Hamiltonian as

$$\begin{aligned}
\mathcal{H} &= \frac{1}{2\pi} \int_0^{2\pi} dk \sum_n \left\{ t c_{n,k}^\dagger c_{n+1,k} + \gamma \cos(2\pi pn + k) c_{n,k}^\dagger c_{n,k} + h.c. \right\} \\
&= \sum_{n,m} \left(t c_{n,m}^\dagger c_{n+1,m} + h.c. \right) + \\
&\quad \frac{1}{4\pi} \int_0^{2\pi} dk \sum_n \sum_{m,m'} \left(\gamma e^{i(2\pi pn+k)} e^{ik(m-m')} c_{n,m}^\dagger c_{n,m'} + h.c. \right),
\end{aligned}$$

resulting in

$$\mathcal{H} = \sum_{n,m} \left(t c_{n,m}^\dagger c_{n+1,m} + \gamma \frac{e^{i(2\pi pn)}}{2} c_{n,m}^\dagger c_{n,m+1} + h.c. \right). \tag{5.21}$$

This Hamiltonian is already known to be describing a two-dimensional rectangular lattice where electrons are hopping in the presence of a uniform magnetic field with p flux quanta per unit cell (a similar setting as the QHE; see appendix A.2). A graphical representation of this model is shown on figure 5.8a

When the flux quantum $p = q/l$ is rational, the spectrum of this Hamiltonian is composed of l bands. Recall that in section 3.2.2, we derived the Hall conductance

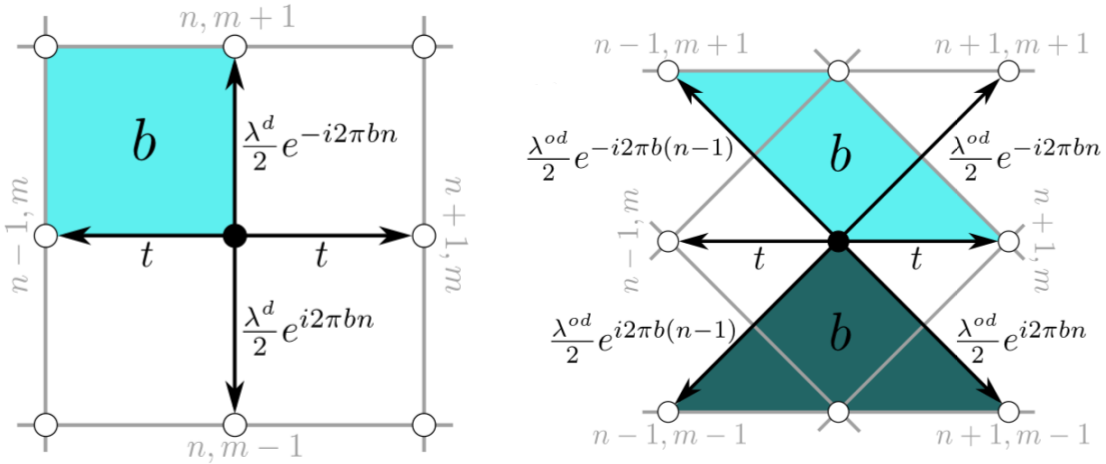

(a) (b)

Figure 5.8: Graphical representation of the two-dimensional Hamiltonians. a) Diagonal modulation. b) Off-diagonal modulation. The arrows represent a hopping amplitude (t, $\lambda \equiv \lambda^d$, $\gamma \equiv \lambda^{od}$), the amount of flux quanta going through a unit cell is represented by $p = b$). Figure from ref. [10]

as the sum of Chern numbers associated with each band:

$$\sigma_{xy} = \frac{e^2}{2\pi\hbar}C, \quad \text{where} \quad C \equiv \sum_a C_a.$$

In other words, each gap is associated with a Chern number, given by integer values of the Hall conductance. When taking an appropriate limit $q, l \to \infty$, p becomes irrational and the spectrum becomes fractal. The gaps, however, are still characterised by those Chern numbers, and it is shown in a paper by Kraus *et al.* [1] that for irrational values of p, the Berry curvature is independent of the parameter k, such that one can obtain the topological characterisation without resorting to an integration over Berry curvature. This means that the one-dimensional Harper model inherits the Chern numbers associated to the two-dimensional model.
For the off-diagonal case, the ancestor Hamiltonian takes the following form:

$$\mathcal{H} = \sum_{n,m}\left(tc^\dagger_{n,m}c_{n+1,m} + \frac{\lambda}{2}(e^{i2\pi pn}c^\dagger_{n,m}c_{n+1,m+1} + e^{-i2\pi pn}c^\dagger_{n,m}c_{n+1,m-1}) + h.c.\right) \tag{5.22}$$

with a graphical representation shown in figure 5.8b. The two models are topologically equivalent, meaning that the system can continuously change from having a modulation of the on-site potential to having a modulated hopping without closing the band gaps [10]. Their topological phases are therefore described by the same indices.

Topological Equivalence of the FQC and the Harper model If we let the two values of the on-site FQC potential be $v_n \pm 1$, we can write it in the following form [10]:

$$v_n = 2\left(\left[\frac{n+2}{\tau}\right] - \left[\frac{n-1}{\tau}\right]\right) - 1 = \pm 1, \tag{5.23}$$

where τ is the golden ratio. We can write down a generalized potential, $V_n^S(k;\beta)$, in terms of a parameter β which smoothly connects the Fibonacci and Harper potentials:

$$V_n^S(k;\beta) = \frac{\tanh\{\beta[\cos(2\pi pn + k) - \cos(\pi p)]\}}{\tanh\beta}. \tag{5.24}$$

As $\beta \to 0$, we recover the Harper modulation with a constant shift. As $\beta \to \infty$, the Fibonacci QC modulation (5.23) is obtained. In fact, the function $V_n^S(k;\beta)$ is completely continuous when its domain is $[0,\infty)$, meaning that the two Hamiltonians are deformable into each other without crossing any singularities. They are thus topologically equivalent.

Observations of Edge States in Quasicrystals As we have already seen before, in the numerical calculation of on-site FQC eigenstates of the Hamiltonian, edges states arise in finite FQCs. They have in fact also been observed experimentally in the works of Kraus *et al.* [10], where they constructed an optical, quasiperiodic lattice based on the Aubry-André (Harper) model and measured the existence of edge modes. It is in that same paper that they have argued that these edge modes are in fact a result of the existence of a topological phase and that they are protected by its symmetries.

5.4 Renormalization Group (RG) of the Fibonacci Chain- Decimating Generations

In this section, we look at the RG method to understand the structure of the spectrum in more detail [46]. We will overview steps that need to be taken to decimate the chain generation by generation, and derive the effective couplings that result from the procedure. On top of that, we show that the two models that we study separately are equivalent under this RG. The equivalence becomes clear after taking an additional step in the decimation process for the on-site model.

The goal of this method is to get an insight on the structure of the n^{th} Fibonacci approximant Hamiltonian spectrum, i.e the spectrum of

$$H = \sum_{j=1}^{F_n} t_j \Big(|j\rangle\langle j+1| + |j+1\rangle\langle j| \Big), \tag{5.25}$$

where $F_n = F_{n-1} + F_{n-2}$ is the n^{th} Fibonacci number and the hopping parameters take on two values, $\{t_w, t_s\}$, following the distribution of the Fibonacci chain. The spectrum is shown in figure 5.4. In the limit $\rho \equiv t_w/t_s \ll 1$, we can devise a perturbative approach to study the Hamiltonian. This procedure goes as follows:

- Diagonalize the strong-bond Hamiltonian H_0, by setting $t_w = 0$. This results in three degenerate levels:

$$E_0 = \begin{cases} t_s, & \text{(bonding level)} \\ 0, & \text{(atomic level)} \\ -t_s, & \text{(anti-bonding level).} \end{cases}$$

- We then introduce a perturbation H_1 which contains all terms with t_w. This lifts the degeneracy in each level, but keeps them well separated. In turn, each of these levels is further fragmented and constitutes the spectrum of a sublattice. We call the three resulting sublattices
  - bonding chain,
  - atomic chain,
  - anti-bonding chain.
- These chains have themselves a new set of hopping parameters, which we call renormalized couplings taking the following values (which we will derive next):

$$\{t'_w, t'_s\} = \begin{cases} \left\{\dfrac{t_w^2}{2t_s}, \dfrac{t_w}{2}\right\}, & \text{(bonding chain)} \\ \left\{\dfrac{t_w^3}{t_s^2}, -\dfrac{t_w^2}{t_s}\right\}, & \text{(atomic chain)} \\ \left\{\dfrac{t_w^2}{2t_s}, -\dfrac{t_w}{2}\right\}, & \text{(anti-bonding chain).} \end{cases}$$

These three sublattices can be obtained by applying two kinds of generation decimation. The first one, called molecular decimation is applied on the (anti) bonding level, and goes as follows:

- Replace every strong bond of the original lattice by a site in the decimated lattice.
- Connect the new sites with strong bonds if they are directly linked by a weak bond in the original lattice. Connect them with weak bonds if an atomic site is present in between them.

The second one, called atomic decimation, is applied to the atomic level and goes as follows:

- Replace every single atomic site in the original lattice by a site in the decimated lattice.
- Connect the new sites with a strong bond if there is only one molecular bond between the two atomic sites of the original lattice. Connect them with weak bonds if there are two.

A scheme of the procedure is drawn in figures 5.9 and 5.10. We note at this point that, although this procedure seems limited to the hopping model, it also works for the on-site model in the case where $|V_S - V_L| \gg t$ [46]. The equivalence between the two is evident when we apply the following decimation procedure:

- Take the Hamiltonian $H_0 = \sum V_i \left|i\right\rangle \left\langle i\right|$, where $t = 0$. It is already diagonal and has two degenerate levels with energies V_S and V_L.
- Introduce the perturbation $H_1 = \sum t(\left|i\right\rangle \left\langle i+1\right| + \text{h.c})$, within each level. This results in two chains with one kind of site each, having different hoppings given by

$$\{t_w, t_s\} = \begin{cases} \left\{\dfrac{t^2}{V_S - V_L}, t\right\}, & (V_L \text{ chain}) \\ \left\{\dfrac{t^3}{(V_L - V_S)^2}, \dfrac{t^2}{V_L - V_S}\right\}, & (V_S \text{ chain}) \end{cases}$$

That last step is in fact a reduction to the hopping Fibonacci model. A scheme of the decimation for one kind of site is shown on figure 5.11.

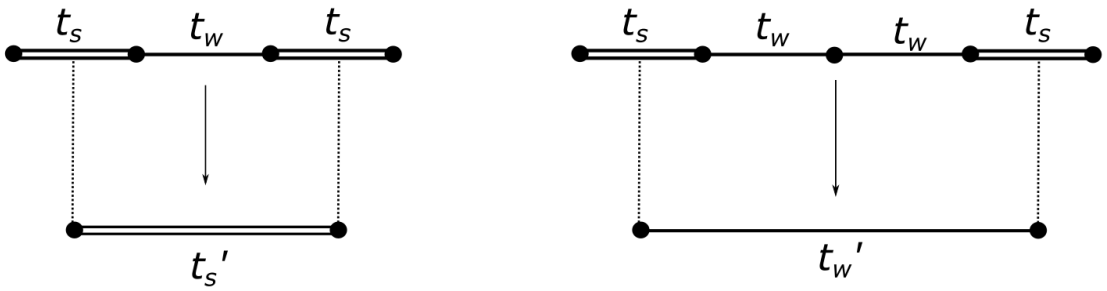

Figure 5.9: Molecular decimation. We obtain an effective strong hopping on the left, and an effective weak one on the right.

In order to derive the effective hopping parameters, we first need to set up our perturbation series for the Hamiltonian. To this end, we write the Schrödinger equation with the original Hamiltonian as

$$\begin{aligned} H\left|\psi\right\rangle = (H_0 + H_1)\left|\psi\right\rangle &= E\left|\psi\right\rangle, \\ (E - H_0)\left|\psi\right\rangle &= H_1\left|\psi\right\rangle. \end{aligned}$$

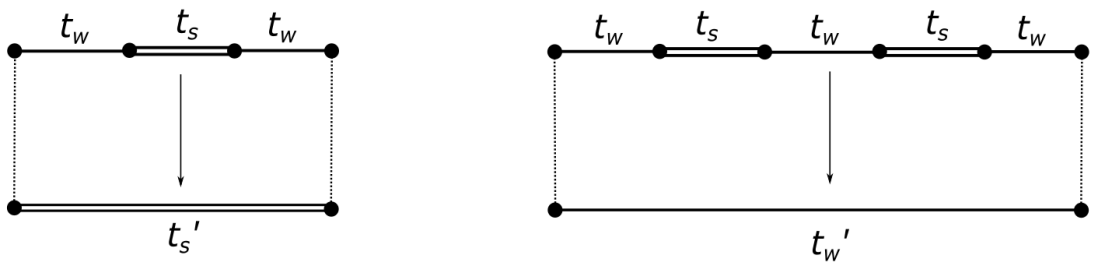

Figure 5.10: Atomic decimation. We obtain an effective strong hopping on the left, and an effective weak one on the right.

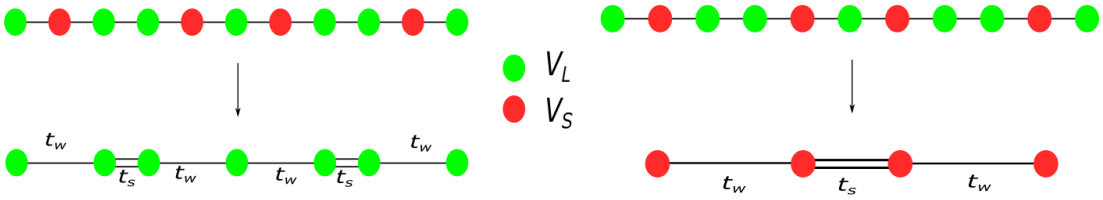

Figure 5.11: Additional decimation step for the on-site. On the left picture, the S sites are decimated and on the right, the L ones.

We introduce the projection operators Q, which project the unperturbed Hamiltonian onto one of its three degenerate subspaces. Its complement, projecting H_0 out, is given by $P = \mathbb{1} - Q$. By definition, they commute with H_0. With this, we can split the Schrödinger equation in two:

$$(E - H_0)Q\,|\psi\rangle = QH_1\,|\psi\rangle = QH_1(Q^2 + P^2)\,|\psi\rangle\,, \tag{5.26}$$
$$(E - H_0)P\,|\psi\rangle = PH_1\,|\psi\rangle = PH_1(P^2 + Q^2)\,|\psi\rangle\,, \tag{5.27}$$

where we used $Q^2 = Q$, $P^2 = P$ and $P + Q = \mathbb{1}$. From Eq. 5.27, we can write

$$P\,|\psi\rangle = \Big[(E - H_0) - PH_1P\Big]^{-1} PH_1Q^2\,|\psi\rangle\,. \tag{5.28}$$

If we plug that back into equation 5.26, we obtain

$$(E - H_0)Q\,|\psi\rangle = \big(QH_1Q + QH_1P[(E - H_0) - PH_1P]^{-1}PH_1Q\big)\,Q\,|\psi\rangle\,.$$

The effective Hamiltonian for a sublattice is thus given by

$$H_{eff} = H_0 + QH_1Q + QH_1P[(E - H_0) - PH_1P]^{-1}PH_1Q. \tag{5.29}$$

We expand this expression in powers of H_1 and will keep terms up to and including $\mathcal{O}(H_1^3)$, as they are necessary to derive the effective hoppings. This results in

$$\begin{aligned} H_{eff} = H_0 &+ QH_1Q + QH_1P[E - H_0]^{-1}PH_1Q \\ &+ QH_1P[E - H_0]^{-1}PH_1P[E - H_0]^{-1}PH_1Q + \mathcal{O}(H_1^4). \end{aligned}$$

With this effective Hamiltonian for each of the sublattices, we can now calculate the effective hoppings are.

Molecular effective hopping parameters. We start with the molecular decimation. For the strong coupling, we consider the chain depicted in figure 5.9, on the left. There are four on-site states $\{|1\rangle, |2\rangle, |3\rangle, |4\rangle\}$. The Hamiltonians are given by

$$\begin{aligned} H_0 &= t_s\big(\,|1\rangle\langle 2| + |3\rangle\langle 4| + \text{h.c}\big), \\ H_1 &= t_w\big(\,|2\rangle\langle 3| + \text{h.c.}\big). \end{aligned}$$

The eigenstates of H_0 are

$$\left.\begin{aligned} |+\rangle_1 &= \frac{1}{\sqrt{2}}\big(\,|1\rangle + |2\rangle\,\big) \\ |+\rangle_2 &= \frac{1}{\sqrt{2}}\big(\,|3\rangle + |4\rangle\,\big) \end{aligned}\right\} E_0 = t_s \;\; \text{(bonding)},$$

and

$$\left.\begin{aligned} |-\rangle_1 &= \frac{1}{\sqrt{2}}\big(\,|1\rangle - |2\rangle\,\big) \\ |-\rangle_2 &= \frac{1}{\sqrt{2}}\big(\,|3\rangle - |4\rangle\,\big) \end{aligned}\right\} E_0 = -t_s \;\; \text{(anti-bonding)},$$

The action of H_1 on these states is

$$\begin{aligned} H_1\,|\pm\rangle_1 &= \pm\frac{t_w}{\sqrt{2}}\,|3\rangle\,, \\ H_1\,|\pm\rangle_2 &= \frac{t_w}{\sqrt{2}}\,|2\rangle\,. \end{aligned}$$

The renormalized hopping is obtained from the first-order term in H_{eff}, i.e

$$\begin{aligned} t'_s &= {}_1\langle +|H_1\,|+\rangle_2 = \frac{t_w}{2} \;\; \text{(bonding sublattice)}, \\ t'_s &= {}_1\langle -|H_1\,|-\rangle_2 = -\frac{t_w}{2} \;\; \text{(anti-bonding sublattice)}. \end{aligned} \tag{5.30}$$

We now take the chain on the right to compute the weaker effective hopping. There are now five states, $\{|1\rangle, |2\rangle, |3\rangle, |4\rangle, |5\rangle\}$. The Hamiltonians are given by

$$\begin{aligned} H_0 &= t_s\big(\,|1\rangle\langle 2| + |4\rangle\langle 5| + \text{h.c.}\big), \\ H_1 &= t_w\big(\,|2\rangle\langle 3| + |3\rangle\langle 4| + \text{h.c}\big). \end{aligned}$$

H_0 is thus diagonalized by $|3\rangle$ ($E_0 = 0$, atomic),

$$\left.\begin{aligned} |+\rangle_1 &= \frac{1}{\sqrt{2}}\big(\,|1\rangle + |2\rangle\,\big) \\ |+\rangle_2 &= \frac{1}{\sqrt{2}}\big(\,|4\rangle + |5\rangle\,\big) \end{aligned}\right\} E_0 = t_s \;\; \text{(bonding)},$$

and

$$\left.\begin{aligned} |-\rangle_1 &= \frac{1}{\sqrt{2}}\big(\,|1\rangle - |2\rangle\,\big) \\ |-\rangle_2 &= \frac{1}{\sqrt{2}}\big(\,|4\rangle - |5\rangle\,\big) \end{aligned}\right\} E_0 = -t_s \;\; \text{(anti-bonding)},$$

The action of H_1 on these is

$$\begin{aligned} H_1\,|3\rangle &= t_w(|2\rangle + |4\rangle), \\ H_1\,|\pm\rangle_1 &= \pm\frac{t_w}{\sqrt{2}}\,|3\rangle\,, \\ H_1\,|\pm\rangle_2 &= \frac{t_w}{\sqrt{2}}\,|3\rangle\,. \end{aligned}$$

The effective hopping is, once again, obtained from ${}_1\langle\pm|H_{eff}\,|\pm\rangle_2$. In this case, however, the first-order term is 0:

$${}_1\langle\pm|H_1\,|\pm\rangle_2 = \frac{t_w}{\sqrt{2}}\,{}_1\langle\pm|3\rangle_2 = 0,$$

as $|3\rangle$ and $|\pm\rangle_1$ are orthogonal. We then look at the next leading order term of H_{eff}. This gives

$$t'_w = {}_1\langle\pm|H_1 P[\pm t_s - H_0]^{-1} P H_1\,|\pm\rangle_2\,.$$

The projector out of the subspace is given in this case by

$$P_\pm = |\mp\rangle_1\,\langle\mp| + |\mp\rangle_2\,\langle\mp| + |3\rangle\,\langle 3|\,,$$

such that the factor in the middle is evaluated to be

$$\begin{aligned} P[E - H_0]^{-1}P &= P\left(\frac{1}{2t_s}\,|\mp\rangle_1\,\langle\mp| + \frac{1}{2t_s}\,|\mp\rangle_2\,\langle\mp| + \frac{1}{t_s}\,|3\rangle\,\langle 3|\right) \\ &= \frac{1}{2t_s}\,|\mp\rangle_1\,\langle\mp| + \frac{1}{2t_s}\,|\mp\rangle_2\,\langle\mp| + \frac{1}{t_s}\,|3\rangle\,\langle 3|\,. \end{aligned}$$

Plugging this back into t'_w, we get

$$\begin{aligned} t'_w &= {}_1\langle\pm|H_1\left(\frac{1}{2t_s}\,|\mp\rangle_1\,\langle\mp| + \frac{1}{2t_s}\,|\mp\rangle_2\,\langle\mp| + \frac{1}{t_s}\,|3\rangle\,\langle 3|\right) H_1\,|\pm\rangle_2 \\ &= \frac{t_w^2}{2t_s}\,\langle 3|\left(\frac{1}{2}\,|\mp\rangle_1\,\langle\mp| + \frac{1}{2}\,|\mp\rangle_2\,\langle\mp| + |3\rangle\,\langle 3|\right)|3\rangle = \frac{t_w^2}{2t_s}. \end{aligned}$$

This completes the calculation for the effective hopping parameters of the two molecular sublattices.

Atomic effective hopping parameters. We now take figure 5.10 and start with the chain on the left to compute the effective strong hopping. Once again, there are four states, but the Hamiltonians now take the form

$$\begin{aligned} H_0 &= t_s\big(\,|2\rangle\langle 3| + \text{h.c.}\big), \\ H_1 &= t_w\big(\,|1\rangle\langle 2| + |3\rangle\langle 4| + \text{h.c}\big). \end{aligned}$$

H_0 is diagonalized by $|1\rangle$, $|4\rangle$ (E=0) and

$$\begin{aligned} |+\rangle &= \frac{1}{\sqrt{2}}(|2\rangle + |3\rangle), \quad E = t_s \ \text{ (bonding)}, \\ |-\rangle &= \frac{1}{\sqrt{2}}(|2\rangle - |3\rangle), \quad E = -t_s \ \text{ (anti-bonding)}. \end{aligned}$$

The action of H_1 on these states is

$$\begin{aligned} H_1\,|1\rangle &= t_w\,|2\rangle\,, \\ H_1\,|4\rangle &= t_w\,|3\rangle\,, \\ H_1\,|+\rangle &= \frac{t_w}{\sqrt{2}}\big(\,|1\rangle + |4\rangle\,\big), \\ H_1\,|-\rangle &= \frac{t_w}{\sqrt{2}}\big(\,|1\rangle - |4\rangle\,\big). \end{aligned}$$

The renormalized strong coupling is then given by $\langle 1|\,H_{eff}\,|4\rangle$. The first-order correction is zero again, $\langle 1|\,H_1\,|4\rangle = t_w\,\langle 1|3\rangle = 0$. In order to compute the second order correction, we compute the factor in the middle of the operator inside the bra-ket. The projection operator in this case is

$$P = |+\rangle\langle +| + |-\rangle\langle -|\,, \tag{5.31}$$

such that we get

$$\begin{aligned} P[E - H_0]^{-1}P &= P\left(\frac{1}{-t_s}\,|+\rangle\langle +| + \frac{1}{t_s}\,|-\rangle\langle -|\right) \\ &= \frac{1}{t_s}\big(\,-|+\rangle\langle +| + |-\rangle\langle -|\,\big). \end{aligned}$$

The second order correction is given by

$$\begin{aligned} t_s' &= \frac{1}{t_s}\,\langle 1|\,H_1\big(\,-|+\rangle\langle +| + |-\rangle\langle -|\,\big)H_1\,|4\rangle \\ &= \frac{t_w^2}{2t_s}\,\langle 2|\,\big(\,-|+\rangle\langle +| + |-\rangle\langle -|\,\big)\,|3\rangle \\ &= \frac{t_w^2}{2t_s}\big(\,-\langle 2|2\rangle\,\langle 3|3\rangle + \langle 2|2\rangle - \langle 3|3\rangle\,\big) = -\frac{t_w^2}{t_s}. \end{aligned}$$

To get the renormalized weak hopping parameter, we consider the diagram on the right of figure 5.10. In this case, we have 6 states, with Hamiltonians

$$H_0 = t_s(|2\rangle\langle 3| + |4\rangle\langle 5| + \text{h.c}),$$
$$H_1 = t_w(|1\rangle\langle 2| + |3\rangle\langle 4| + |5\rangle\langle 6| + \text{h.c}).$$

The eigenstates are

$$\left.\begin{aligned} |+\rangle_1 &= \frac{1}{\sqrt{2}}\big(\,|2\rangle + |3\rangle\,\big) \\ |+\rangle_2 &= \frac{1}{\sqrt{2}}\big(\,|4\rangle + |5\rangle\,\big) \end{aligned}\right\} E_0 = t_s \quad \text{(bonding)},$$

$$\left.\begin{aligned} |1\rangle \\ |6\rangle \end{aligned}\right\} E_0 = 0 \quad \text{(atomic)},$$

and

$$\left.\begin{aligned} |-\rangle_1 &= \frac{1}{\sqrt{2}}\big(\,|2\rangle - |3\rangle\,\big) \\ |-\rangle_2 &= \frac{1}{\sqrt{2}}\big(\,|4\rangle - |5\rangle\,\big) \end{aligned}\right\} E_0 = -t_s \quad \text{(anti-bonding)}.$$

The action of H_1 on these states is

$$\begin{aligned} H_1\,|1\rangle &= t_s\,|2\rangle\,, \\ H_1\,|6\rangle &= t_s\,|5\rangle\,, \\ H_1\,|\pm\rangle_1 &= \frac{1}{\sqrt{2}}(|1\rangle \pm |4\rangle), \\ H_1\,|\pm\rangle_2 &= \frac{1}{\sqrt{2}}(|3\rangle \pm |6\rangle). \end{aligned}$$

We can now compute the effective hopping $\langle 1|\,H_{eff}\,|6\rangle$. In this case, it is not only the first term that gives a zero contribution to the effective hopping, the second term in the perturbation expansion also does so. The projection operator is given by

$$P = |+\rangle_1\langle +| + |-\rangle_1\langle -| + |+\rangle_2\langle +| + |-\rangle_2\langle -|\,,$$

so that

$$P[-H_0]^{-1}P = \frac{1}{t_s}\big(\,-|+\rangle_1\langle +| + |-\rangle_1\langle -| - |+\rangle_2\langle +| + |-\rangle_2\langle -|\,\big),$$

and

$$\begin{aligned}\langle 1|\, H^{(2)}_{eff}\,|6\rangle &= \langle 1|\, H_1 \frac{1}{t_s}\big(-|+\rangle_1\langle +| + |-\rangle_1\langle -| - |+\rangle_2\langle +| + |-\rangle_2\langle -|\,\big) H_1\,|6\rangle \\ &= \frac{t_w^2}{t_s}\,\langle 2|\,\big(-|+\rangle_1\langle +| + |-\rangle_1\langle -| - |+\rangle_2\langle +| + |-\rangle_2\langle -|\,\big)\,|5\rangle \\ &= 0.\end{aligned}$$

The leading correction is then of order 3 and we have

$$\begin{aligned}t'_w &= \langle 1|\, H_1 P[E-H_0]^{-1} P H_1 P[E-H_0]^{-1} P H_1\,|6\rangle \\ &= \frac{t_w^2}{t_s^2}\,\langle 2|\,\big(-|+\rangle_1\langle +| + |-\rangle_1\langle -| - |+\rangle_2\langle +| + |-\rangle_2\langle -|\,\big) \\ &\qquad \times H_1\big(-|+\rangle_1\langle +| + |-\rangle_1\langle -| - |+\rangle_2\langle +| + |-\rangle_2\langle -|\,\big)\,|6\rangle \\ &= \frac{t_w^2}{t_s^2}\,\langle 2|\,\big(-|+\rangle_1\langle +| + |-\rangle_1\langle -| - |+\rangle_2\langle +| + |-\rangle_2\langle -|\,\big) \\ &\qquad \times \Big(-\frac{t_w}{\sqrt{2}}(|1\rangle + |4\rangle)\,{}_1\langle +| + \frac{t_w}{\sqrt{2}}(|1\rangle - |4\rangle)\,{}_1\langle -| \\ &\qquad\quad -\frac{t_w}{\sqrt{2}}(|3\rangle + |6\rangle)\,{}_2\langle +| + \frac{t_w}{\sqrt{2}}(|3\rangle - |6\rangle)\,{}_2\langle -|\Big)\,|5\rangle \\ &= \frac{t_w^3}{2t_s^2}\,\langle 2|\,\big(-|+\rangle_1\langle +| + |-\rangle_1\langle -| - |+\rangle_2\langle +| + |-\rangle_2\langle -|\,\big) \\ &\qquad\qquad \times\Big(-(|3\rangle + |6\rangle) - (|3\rangle - |6\rangle)\Big) \\ &= -\frac{t_w^3}{t_s^2}\Big(-\frac{1}{2} - \frac{1}{2}\Big) = \frac{t_w^3}{t_s^2}.\end{aligned}$$

We have thus derived all three renormalized hopping strengths,

$$\{t'_w, t'_s\} = \begin{cases} \left\{\dfrac{t_w^2}{2t_s}, \dfrac{t_w}{2}\right\}, & \text{(bonding chain)} \\ \left\{\dfrac{t_w^3}{t_s^2}, -\dfrac{t_w^2}{t_s}\right\}, & \text{(atomic chain)} \\ \left\{\dfrac{t_w^2}{2t_s}, -\dfrac{t_w}{2}\right\}, & \text{(anti-bonding chain),} \end{cases}$$

as envisaged. The derivation of the two effective couplings, resulting from the first decimation step of the on-site model, is also done in a similar way, but the calculations are easier to carry out, as the unperturbed Hamiltonian is already diagonal.

Renormalization Paths. After having performed the procedure described above, we can ask ourselves where does a particular site come from, as it climbs up from

lower generations. The answer to that question is what is called its "renormalization path" [46]. We label the two kinds of sites by 'm' (molecular site) and 'a' (atomic site). A particular path can take the form '$amma...m$' for an atomic site at the top of the renormalization process, or '$mmam...m$' for a molecular one.
The same question can be asked for energy eigenstates. Where does a particular level come from? It also has a renormalization path that it follows, but we make the distinction between whether it sits in the top cluster 't' (bonding molecular), the central cluster 'c' (atomic) or the bottom cluster 'b'. A particular level can then be encoded by the symbolic string sequence '$tctbt...c$' for example. There exists a particular symmetry between the two renormalization paths in the perturbative limit ($\rho \ll 1$), which becomes evident with the "cut and project" method (see figure 5.13) [47]. By defining the conumber [48], this symmetry becomes visually present in the self-similar, fractal plot of energy levels versus conumber. The resulting structure, with two plots of chains of different sizes, is shown in figure 5.12. For an M^{th} generation chain, this conumber is defined as

$$C_j = jF_{M-1} \text{mod}(F_M). \tag{5.32}$$

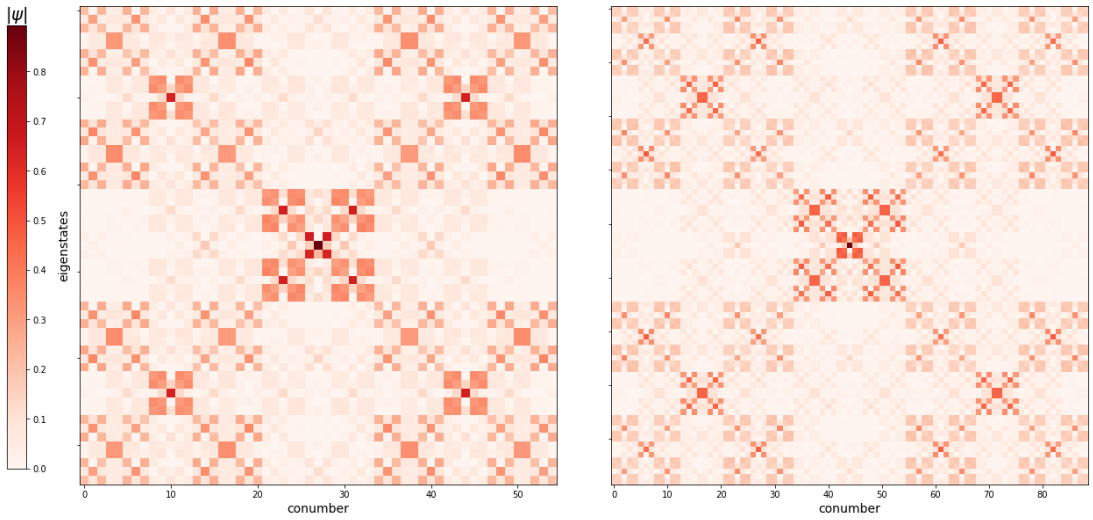

Figure 5.12: Fractal structure of the hopping model with PBC. The chains are of generation 9 and 10, respectively.

5.4.1 Disorder in the Fibonacci chain (Original Results)

We study the effect of disorder by introducing, at the simplest level, one impurity at some site m. The Hamiltonian with the impurity reads

$$H = \sum_i t_i(|i\rangle \langle i+1| + |i+1\rangle \langle i|) + V_d |m\rangle \langle m| . \tag{5.33}$$

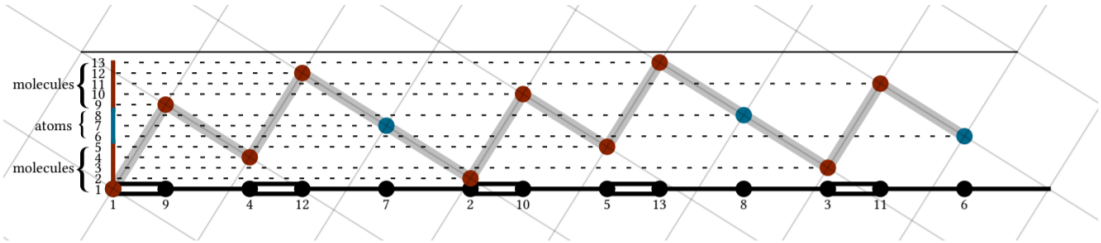

Figure 5.13: Relabeling of the sites according to their conumber, obtained by projecting the sites on the vertical axis. Conumbers naturally order the sites depending on whether they are atomic or molecular. The former lie at the center, while the latter are at the edges. Figure taken from ref. [47].

The impurity can sit on an atomic site or a molecular site. We study the case where the impurity takes a value $V_d < \rho$, so that we can take it to be a perturbation to the original Hamiltonian. In fact, we will incorporate it in the Hamiltonian H_1 that we considered above, in equation (5.29). Placing the impurity at the atomic site $m = 1$ in the right chain of figure 5.10, the energy, to first order, is given by

$$\begin{aligned} E &= E_0 + E_1 = V_d, \quad (E_0 = 0) \\ E_1 &= \langle 1| H_1 |1\rangle = V_d, \end{aligned}$$

In figure 5.14 b), we see the shift of the central site clearly when the impurity is placed in there. In a) and c), the atomic impurity is placed such that it lies on the left and right of the conumbered sites. In this case, there are more states that feel the shift in energy from those sites. Moreoever, as we shall see later, it generates the same type of disordered graph, belonging to the same "class", the only difference being that they are mirror images of each other. The molecular energy levels do not get modified to first order, as they are made of superpositions $|i\rangle \pm |i+1\rangle$ that are orthogonal to the atomic site. Moreover, if the atomic site is renormalized to an atomic site in the sublattice, the same result holds there, and there is very little perturbation to the main structure, especially on the molecular clusters. If we had taken the cartoon on the left of figure 5.10 (leading to the strong renormalized coupling), then the atomic site becomes a molecular site in the renormalized lattice, and there is more disorder in general in the fractal, which not only sits at the atomic clusters, but also the molecular ones.
In the case of a molecular site impurity, we take first the site $m = 1$ in figure 5.9, on the left. This results in the energy of the renormalized molecular site to take on a first-order corrected value

$$E_1 = {}_1\langle \pm | H_1 | \pm \rangle_1 = \frac{V_d}{\sqrt{2}}.$$

If we now place the impurity at site $m = 1$ of the right figure in 5.9, we obtain the same results, but with the possibility of having an atomic site in the renormalized

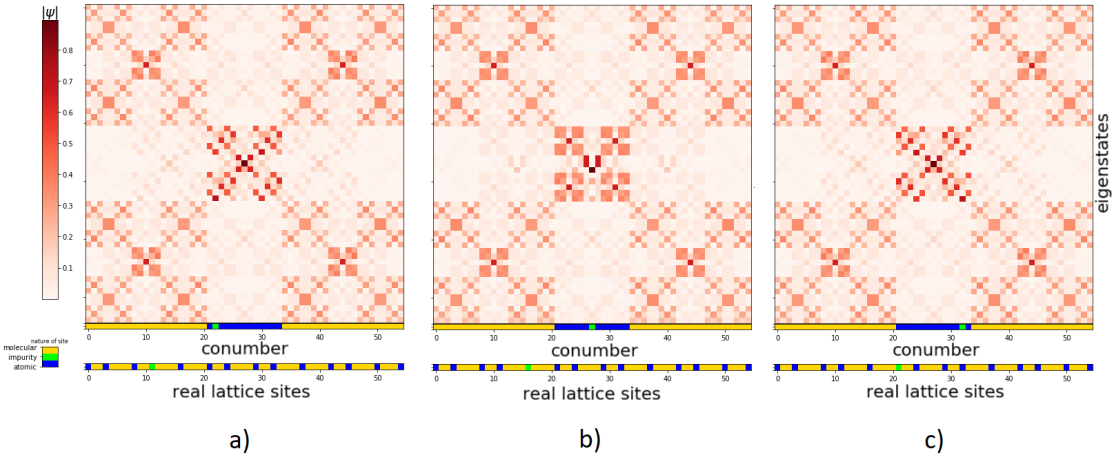

Figure 5.14: Impurity on the atomic cluster, with potential $V_{imp} = 0.1$. a) Impurity on the left. b) Impurity in middle. c) Impurity on the right.

lattice, which increases the disorder in the fractal structure. This explains the features observed in figure 5.15.

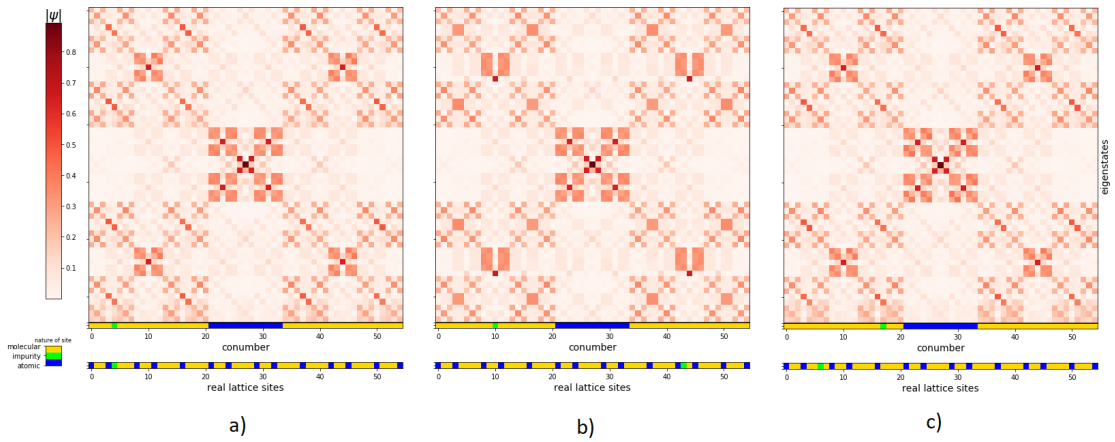

Figure 5.15: Impurity on the left molecular cluster, with potential $V_{imp} = 0.1$. a) Impurity on the left. b) Impurity in middle. c) Impurity on the right.

Finally, any effect of the impurity on the renormalized couplings is absent up to at least order V_d^3.
To summarize, the effect of the impurity on how disordered the fractal pattern becomes depends on the renormalization path of the site at which it is placed. Placing an impurity on an atomic (molecular) site for which the renormalization path has a high density of atomic (molecular) sites will result in less disorder than one for which the density of molecular (atomic) sites is significant. It might be worth investigating the quantitative regimes (densities of the respective sites along the renormalization path) in which the disorder becomes significant.

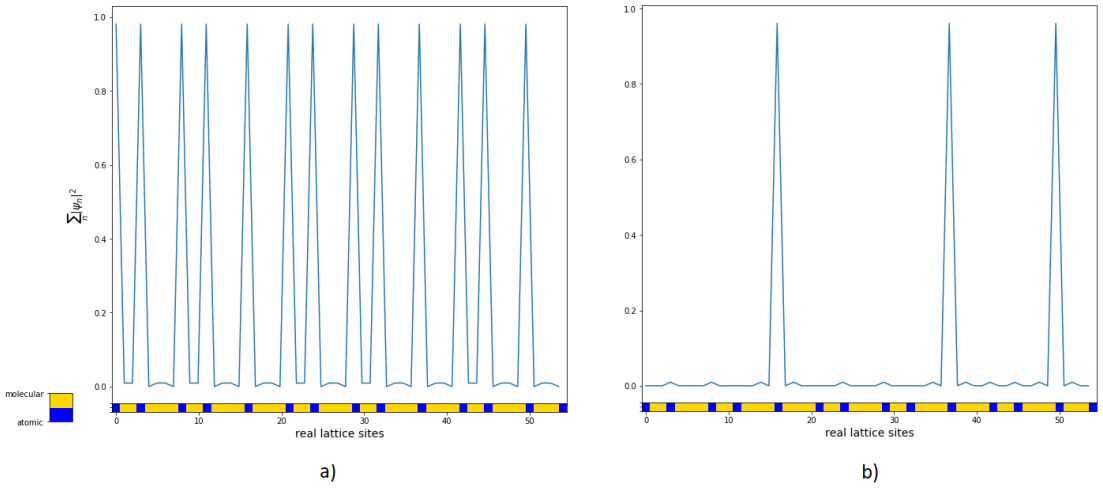

Figure 5.16: Atomic cluster Probabilities. a) Original central cluster. b) Central subcluster of the original central cluster.

Localisation character

The main feature of quasicrystalline phases is that eigenmodes exhibit what is called "criticality". That is they are neither extended, as in the periodic case with Bloch waves, nor are they strictly localized, like the disordered case. In fact, in the case of the Fibonacci crystal, the probability density follows a power law, which is a result of the scaling behavior of the wavefunctions. This power law can be derived through the method of transfer matrices [49] and yields

$$|\psi(L)| \sim L^{\log|t_s/t_w|/\log(\tau^p)}, \tag{5.34}$$

where L is the average intersite length. p is 2 in case the renormalization path is fully molecular and 3 when it is fully atomic. In between, it depends on the how many atomic and molecular sites are present in the renormalization path [46]. A nice feature of this chain is that the integrated density of states of a certain cluster localises according to its nature. For example, the central (atomic cluster) has peaks on atomic sites while the bonding (and anti-bonding) clusters have them on molecular sites. Moreover, when one goes down the decimation path, the same is observed for the decimated chain. Examples are shown in figures 5.16 and 5.17.
The interesting thing when one adds an impurity is the appearance of a state in a gap of the original Fibonacci spectrum. This leads to exponential localization, as we can see in figure 5.18. This can be understood using Green's's functions for tight-binding Hamiltonians [50].
We let H_0 denote the Fibonacci Hamiltonian and H_1 denote the impurity Hamil-

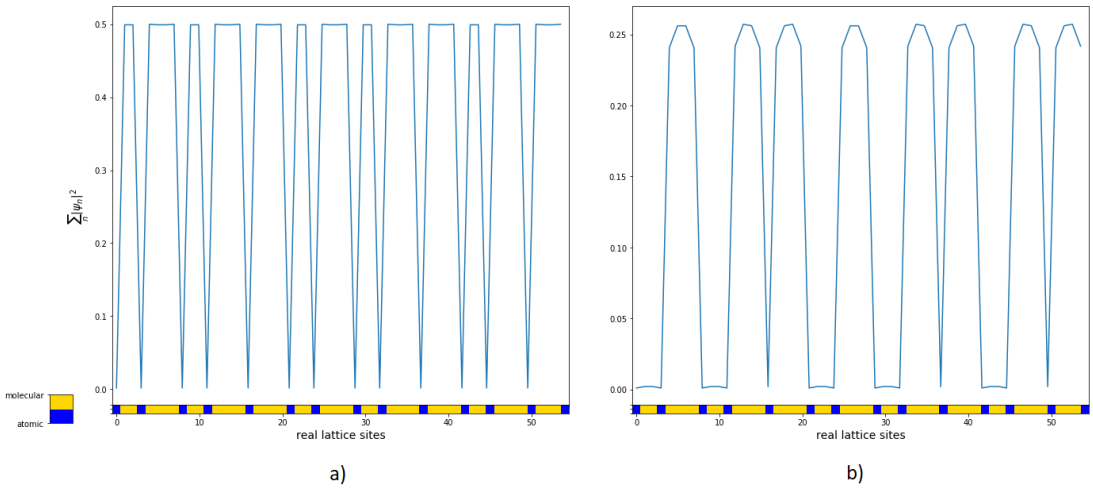

Figure 5.17: Molecular cluster probabilities. a) Original left/right cluster. b) Left/Right subcluster of the original.

tonian. The matrix elements of the unperturbed Green's function are given by

$$G_0(i,j;E) = \langle i| \frac{1}{E - H_0} |j\rangle = \sum_\alpha \frac{\langle i|\alpha\rangle \langle \alpha|j\rangle}{E - E_\alpha}, \tag{5.35}$$

where $|\alpha\rangle$ is an eigenstate of H_0 and E_α its energy. When taking into account the perturbation with V_{imp}, the new Green's function follows the self-consistent Dyson equation, given by

$$G = G_0 + G_0 H_1 G, \tag{5.36}$$

with $H_1 = V_{imp} |n\rangle \langle n|$ for an impurity located at site n. The Green's function's matrix elements are thus given by

$$G(i,j;E) = G_0(i,j;E) + G_0(i,n;E) V_{imp} G(n,j;E).$$

By setting $i = n$, we can solve for $G(n,j;E)$ to get

$$G(i,j;E) = G_0(i,j;E) + \frac{V_{imp}}{1 - V_{imp} G_0(n,n;E)} G_0(i,n;E) G_0(n,j;E).$$

Thus, we have a pole of the Green's function lying at

$$G_0(n,n;E) = \frac{1}{V_{imp}}. \tag{5.37}$$

Since we have shifted a certain state's energy by V_{imp}, the energy $E = E_0$ level of this state will lie in a gap of the spectrum and hence $E_0 \neq E_\alpha$. Thus, the only pole of the Green's function is the one given above. Moreoever, the density

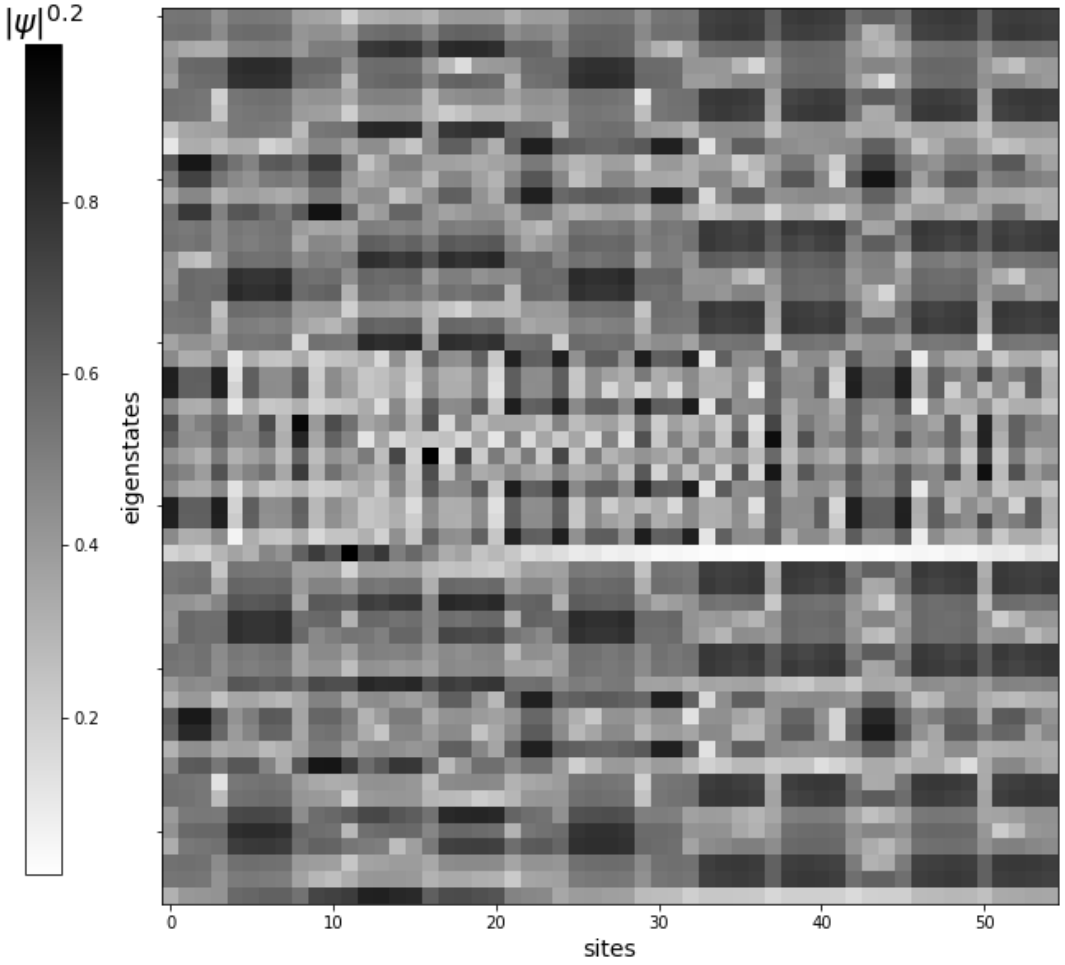

Figure 5.18: Exponential localisation as a result of the impurity (see the white line).

of states at the edge of the gap for a 1 dimensional chain diverges [51], making $G_0(n, n, E)$ a monotonically decreasing function of E within the gap; i.e at some point the pole of $G(i, j; E)$ is crossed when $E = E_0$. The overlap between this state's wavefunction at site i and j is given by

$$\Psi(i)\Psi(j)^* = \frac{1}{2\pi i} \oint_{C_{E_0}} dz G(i, j; z),$$

where we have taken $\Psi(i) = \langle i|E_0\rangle$ and C_{E_0} is a counter-clockwise oriented circle with centre located at E_0, in the complex plane. Using the residue theorem, we

have

$$\begin{aligned}\frac{1}{2\pi i}\oint_{C_{E_0}} dz G(i,j;z) &= \mathrm{Res}(G(i,j;E_0)) \\ &= \lim_{(z\to E_0)}(z-E_0)\left[G_0(i,j;z)+\frac{V_{imp}}{1-V_{imp}G_0(n,n;z)}G_0(i,n;z)G_0(n,j;z)\right] \\ &= -\frac{G_0(i,n;E_0)G_0(n,j;E_0)}{\left.\frac{dG_0(n,n;z)}{dz}\right|_{z=E_0}}.\end{aligned}$$

Since $G_0(i,n;E_0) \propto e^{-a|i-n|}$ for E_0 outside of the spectrum [51], it follows that this gap state is exponentially localized.

Local Symmetries and classes of disorder

An interesting observation that we came across is that placing impurities on sites belonging to a particular renormalization path give rise to the same perturbed graph. These classes of graphs, for a Fibonacci approximant of the 9^{th} generation, with 55 sites and hoppings, are generated by the following renormalization paths:

- Molecular sites:
  - MMMM (16 sites, generate 2 graphs, mirror images)
  - MMMA (8 sites, generate 2 graphs, mirror images)
  - MMA (8 sites, generate 2 graphs, mirror images)
  - MAM (8 sites, generate 3 graphs, 2 of which are mirror images generated by 4 sites and another generated by the other 4 sites)
  - MAA (2 sites, generate 1 graph)
- Atomic Sites:
  - AAA (1 site, generates 1 graph)
  - AAM (2 sites, generate 2 graph, mirror images)
  - AMA (2 sites, generate 1 graph)
  - AMM (8 sites, generate 3 graph, 2 of which are mirror images generated by 4 sites and one which is generated by the 4 other sites)

The perturbed graphs can be seen in figures 5.19a through to figure 5.24.
At first, we thought that there might be a connection between the degree of "perturbation" in the LDOS fractal plot and the size of the locally symmetric region around the site at which the impurity is placed, as is observed in figure 5.24, but this hypothesis was quickly ruled out by looking at figure 5.22a, which has a

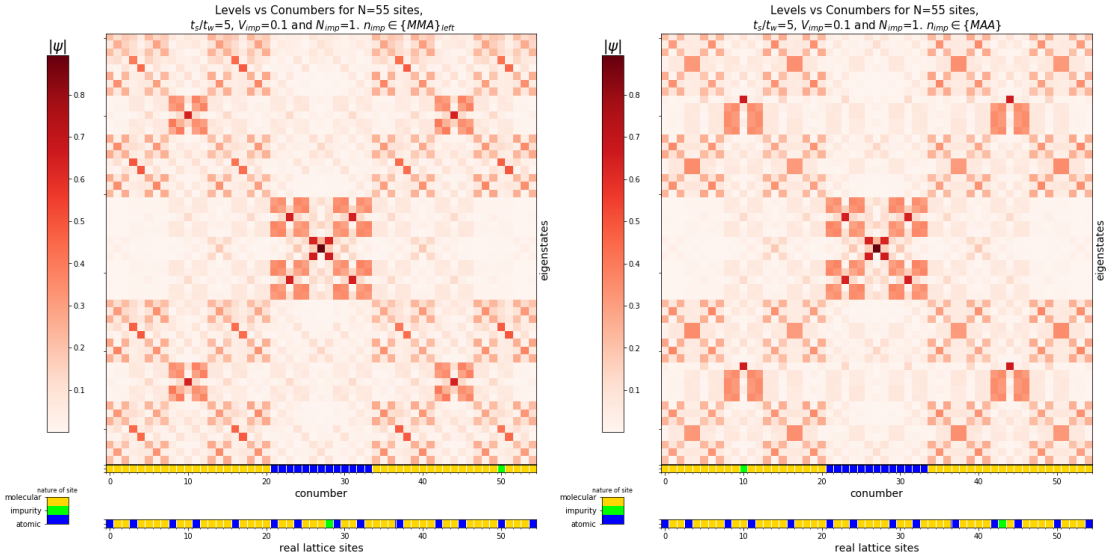

(a) Class MMA (b) Class MAA

Figure 5.19: Example of disorder classes.

smaller region of local symmetry.
There is, however a strong indication from the works of Röntgen *et al.* [11] that local symmetries play an important role, as described in section 5.2.4. There, we saw that the sites at which the amplitude localizes the most are intimately related to the local symmetry structure. Since the effect of the impurity is mostly noticeable at the sites with the largest amplitudes, we expect a link with the local symmetry of the chain. It would be interesting to study the relation between the theory of local resonator modes for the on-site model and the renormalization procedure taking this on-site model to a hopping one. This would provide hints in determining the role of local symmetries in the generic case.

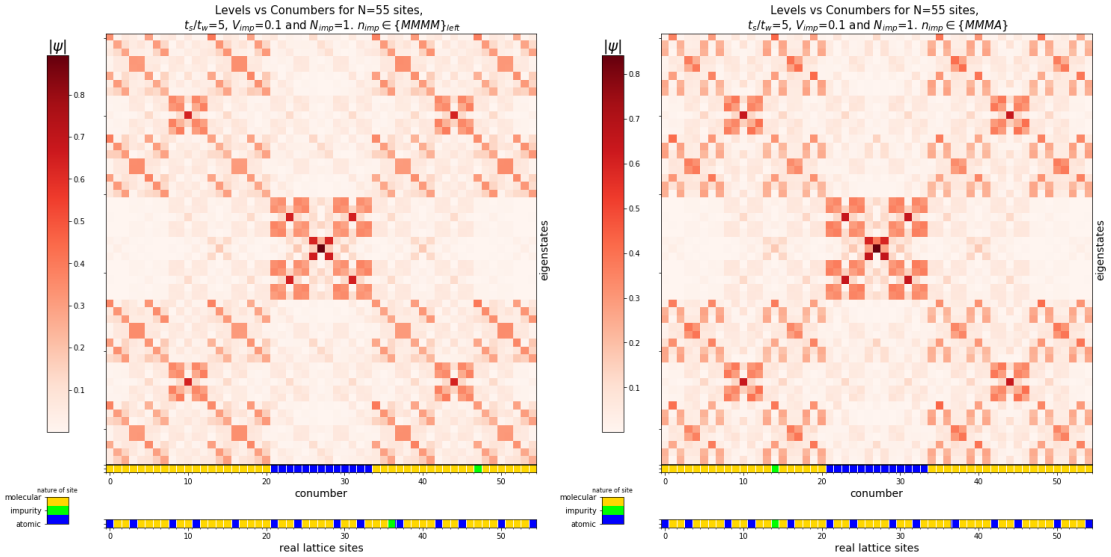

(a) Class MMMM (b) Class MMMA

Figure 5.20: Example of disorder classes.

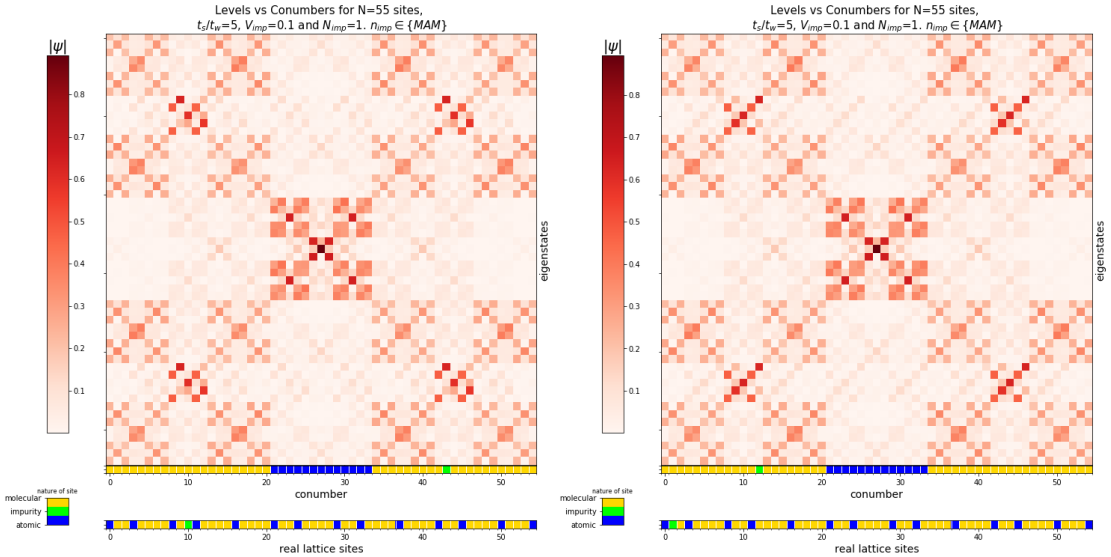

(a) Class MAM 1 (b) Class MAM 2

Figure 5.21: Example of disorder classes.

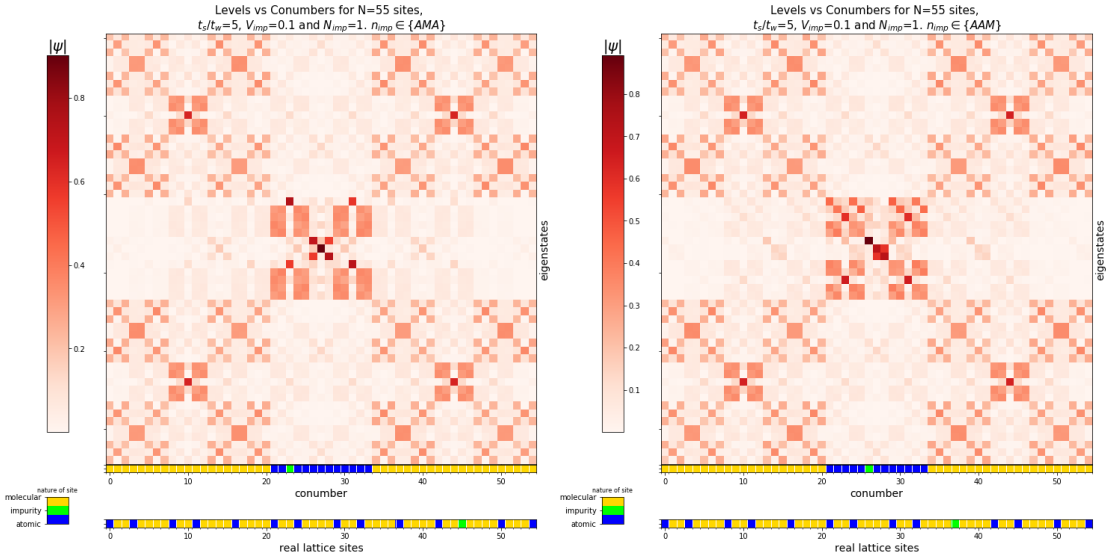

(a) Class AMA. (b) Class AAM

Figure 5.22: Example of disorder classes.

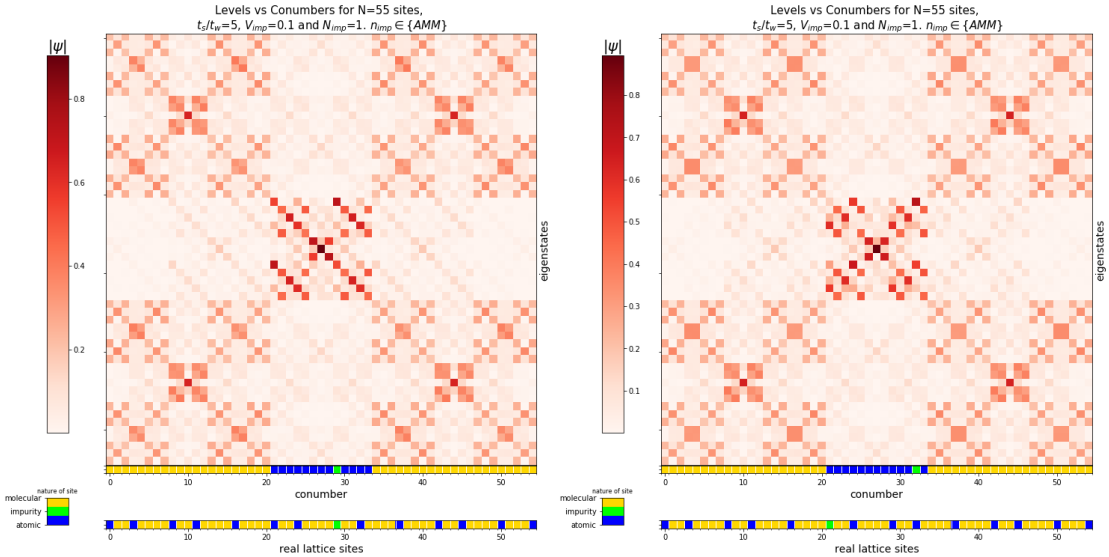

(a) Class AMM 1. (b) Class AMM 2.

Figure 5.23: Example of disorder classes.

To summarize the contents of this chapter, we first started our discussion with quasicrystals in general. This was then followed by an in-depth analysis of the Fibonacci chain with all its local symmetries. We then provided an understanding of the spectrum through a theory of local resonator modes and a renormalization group analysis. An equivalence between the Fibonacci model and the Harper

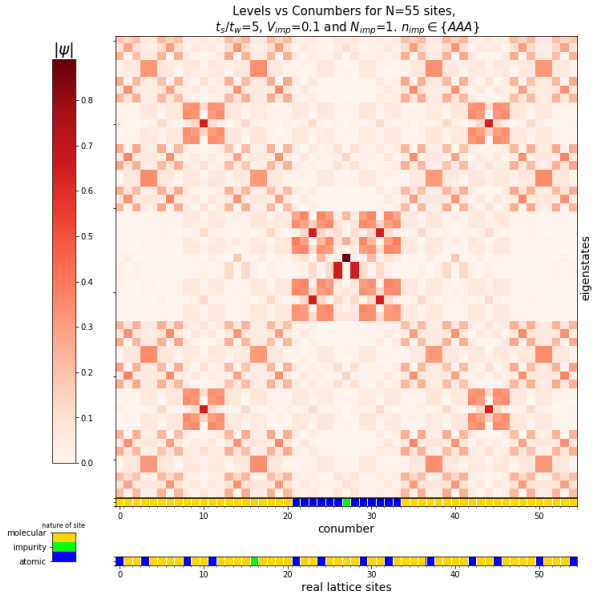

Figure 5.24: Example of a disorder class: AAA.

model was established and the hypothetical topological modes of the Harper model were attributed to the Fibonacci model too. Lastly, we studied the effect of impurities on the hopping model and demonstrated a correspondence between the renormalization paths of the sites at which impurities are placed, and the type of disorder generated by the impurity in the weak strength regime.

6. Outlook

6.1 Outlook

In this section, we first discuss alternative methods that would quantify the topological order of the Fibonacci chains. We then present some suggestions to bridge the gap between the LRM approach to the on-site Fibonacci chain with the RG approach.
In the previous section, we mentioned that the topological characteristics of the Fibonacci chain come from a two-dimensional parent Hamiltonian in a periodic lattice, and it was argued that they survive the projection onto the lattice of codimension 1 [1][10]. The spirit of the alternative methods is that we want to be able to derive topological characteristics directly from the model itself. This would provide a quantification of topological order that can be used to test the chain's robustness against the presence of impurities. Since the Fibonacci chain is not strictly periodic, one cannot formally compute a Berry curvature in momentum space, as is done usually.
We found in the literature that there exist alternative ways of defining topological invariants that, in some cases [52][53], coincide with already established methods. One of them is through the computation of the *Bott* or Localizer indices [54], which are based on a real-space approach, as opposed to momentum space. The second method would be to calculate the entanglement entropy of the Fibonacci chain, as it has been demonstrated that topological order is intimately related to the level of entanglement present in a many-body system [55][56].
We briefly outline in the next part how such analysis can be performed and can give conclusive evidence of whether the Fibonacci chain contains a topological phase or not.

6.1.1 Computation of the Localizer index

The Bott index [57] has been widely used in determining topological phase transitions of periodically driven systems in general [58][59], with disordered topological insulators [52] in particular being well studied. It seems that it is mostly used for two-dimensional, time-dependent Hamiltonians. The alternative index that can be used for more general dimensionalities is the Localizer index. It probes the

topology of a different space than the Bott index [54], but could in principle provide a characterization of topological order. We will briefly provide the ingredients needed in order to compute this index.
First of all, it requires a system with open boundary conditions. In 2D, three observables are required to compute it: the positions X, Y and the Hamiltonian H. Let us denote them by $M_1 = X$, $M_2 = Y$ and $M_3 = H$. One then needs to find a set of matrices that are a Clifford algebra representation. In this case, we can take the Pauli matrices (the same number of matrices as observables is required). The "localizer" matrix is then built according to the definition [54]:

$$L_{\boldsymbol{\lambda}}(M_1, M_2, M_3) = \sum_{j=1}^{3} (M_j - \lambda_j \mathbb{1}) \otimes \sigma_j. \tag{6.1}$$

The Clifford spectrum $\Lambda(M_1, M_2, M_3) \subset \mathbb{R}^3$ of the matrices M_j, is defined such that a vector $\boldsymbol{\lambda} = (\lambda_1, \lambda_2, \lambda_3)$ is in $\Lambda(M_1, M_2, M_3)$ whenever $L_{\boldsymbol{\lambda}}(M_1, M_2, M_3)$ is singular. This localizer, as its name suggests, finds what are called ϵ-approximate eigenvectors $\mathbf{v}$ to the almost-commuting matrices M_i. What this means is that when two matrices M_1 and M_2 almost commute in the sense

$$||[M_1, M_2]|| < \delta,$$

then an ϵ-approximate eigenvector satisfies

$$||M_i \mathbf{v} - \lambda_i \mathbf{v}|| < \epsilon(\delta) \quad \text{for } i = 1, 2.$$

In other words, the localizer finds eigenvectors that "approximately" simultaneously diagonalizes the matrices M_1 and M_2. Note that the approximate denomination is in the sense that $\epsilon \to 0$ as $\delta \to 0$. A proof of these statements can be found in ref. [60]. For any $\boldsymbol{\lambda} \notin \Lambda(M_1, M_2, M_3)$, the localizer index is then defined as

$$\text{ind}(\boldsymbol{\lambda}) = \frac{1}{2}\text{Sig}\Big[L_{\boldsymbol{\lambda}}(X, Y, H)\Big], \tag{6.2}$$

where the $\text{Sig}(M)$ operation gives the difference between the number of positive eigenvalues and that of negative eigenvalues of M:

$$\text{Sig}(M) = (\#\text{of pos eigenvalues}) - (\#\text{of neg eigenvalues}).$$

This index has been shown to coincide with the Chern numbers in the case of the infinite $p_x + ip_y$ model [61].

6.1.2 Calculating Entanglement Entropy

It has been argued for some time that topological order is closely related to the level of long-range entanglement in a system with many degrees of freedom [55].

Different methods to extract this quantitative measure of topological order have been proposed [62] [63] [64]. We will briefly overview the idea and the methods that could potentially provide us with a topological invariant that can characterize the Fibonacci chain.
A measure of entanglement is provided through the von Neuman entropy. Classically, entropy (known as Shannon entropy) is defined as a measure of information gained from learning the outcome of a random event, where each outcome x is given a probability $p(x)$. Quantitatively, the entropy of a given probability distribution p is defined by

$$\mathcal{S}(p) \equiv -\sum_x p(x) \log_2 \big[p(x)\big], \tag{6.3}$$

where $\{x\}$ is the set of all possible outcomes of the random variable X, and the entropy is measured in the amount of bits of information gained. On the other hand, we are dealing with quantum-mechanical systems, which require a modification of this classical Shannon entropy to the von Neuman entropy of a quantum state, represented by the density matrix ρ:

$$S(\rho) = -\operatorname{Tr}\big[\rho \log_2(\rho)\big]. \tag{6.4}$$

These two are related when the density matrix is that of a classical state, which only has diagonal entries. In that case, Eq. (6.4) reduces to Eq. (6.3).
Entanglement requires our system to be divisible into subsystems. These subsystems can then be separable or entangled according to the following definition: the quantum state ρ_{AB} representing the system $A \otimes B$ is separable whenever it can be written as

$$\rho_{AB} = \sum_a P_a \otimes Q_a, \tag{6.5}$$

where P_a is a state of the subsystem A and Q_a of subsystem B. The index a is an element of the set Σ representing the measurement outcomes of system $A \otimes B$. If it is not possible to write a bipartite state ρ_{AB} in the form of Eq. (6.5), then it is said to be an entangled state. One way to measure it is through the *entanglement entropy*:

$$S_E(\rho_{AB}) \equiv S(\rho_A) = S(\rho_B), \tag{6.6}$$

where $\rho_A = \operatorname{Tr}_B[\rho_{AB}]$ and $\rho_B = \operatorname{Tr}_A[\rho_{AB}]$ are reduced density matrices obtained by partially tracing out one of the subsystems. That is, the entanglement entropy is computed from the von Neumann entropy of the reduced state in either subsystems. It is worthy to note that this definition follows because for any separable system, the entanglement entropy is always 0; i.e. $S_E(\rho_{AB}) = 0 \Rightarrow \rho_{AB}$ is separable. This can be easily demonstrated by using the Schmidt decomposition of the bipartite state.
Kitaev and Preskill [63] have demonstrated that for a two-dimensional plane separated into two regions by a circle of circumference of length L, the entanglement

entropy of this system, calculated through the entropy of a quantum state ρ inside the disk is of the form

$$S_E(\rho) = \alpha L - \gamma + \ldots, \tag{6.7}$$

where α is a parameter that depends on the short-range correlations of the system, while γ is a global parameter that does not change with the scale of the system. It is that parameter that they call "topological entanglement entropy".
In this spirit, we should also be able to devise a way to calculate it for a system built from a Fibonacci chain and see whether we can derive a topological order that stems from entanglement between the parts of our system.

6.1.3 Bridging the LRM theory and the renormalization approach

Finally, we have reasons to believe that it is possible to link the level of disorder in an impurity-perturbed Fibonacci chain to the local symmetry structure of the unperturbed chain. In order to go in this direction, we will first have to find a way to renormalize the resonator structures, thereby bridging the LRM theory and the real-space RG. Once that is done, we can place impurities in the on-site model and gauge their effect on the resonators.

6.2 Conclusion

To conclude, we started out by describing the important symmetries of condensed matter that are relevant in describing topological characterizations. We saw that a general framework for topological matter was given in terms of the Ten-fold way. We then briefly presented the theory of wave propagation through locally symmetric structures and its various applications in the description of quantum mechanical systems with locally symmetric potentials. We then moved on to the chapter on quasicrystals. There, we first introduced quasicrystals in general, followed by one-dimensional models. Namely, we went through the Fibonacci chain in great depth and studied its local symmetry structure. The on-site model was also investigated through the lens of a theory of local-symmetry resonators and at the end, we analyzed the spectrum properties using a real-space renormalization procedure. We also presented the Harper model, where signatures of topological states were found through a projection from a two-dimensional periodic system. In turn, it was shown that the Harper model is topologically equivalent to the Fibonacci model, which makes it inherit the same Chern numbers as the former. We studied the effect of impurities on the hopping model and found out that in the weak impurity regime, we can categorize the type of disorder it induces with the renormalization path of the site at which the impurity is placed.
A question that arises from this work is whether the local symmetries of the system provide any kind of protection to the topological states previously found.

Moreover, since the physical mechanism behind these topological states is not understood, another question would be whether topology plays any role in the existence of the observed edge states. The final section outlines what could be done in order to adress these questions. Namely, we could resort to a real-space approach to compute topological indices (Bott index or localizer index), or we can compute the entanglement entropy of the non-interacting Fibonacci chain. In that sense, one can pinpoint the physical mechanisms underlying the hypothetical existence of a topological phase and an associated topological invariant, against which perturbations can be tested (in the form of the impurities we studied, for example). Finally, we think that we can adress the question on the local symmetry protection by connecting the theory of LRMs to the renormaliztion procedure and study the effect of impurities from that perspective.

A. Appendix A

A.1 Quantum Mechanics of Electrons in a Electromagnetic field - Continuum Case

We start by writing down a quantum mechanical description of the system. The derivations are mostly based on David Tong's lecture notes on the QHE [65], where more details can be found. The quantisation effects are already present when we consider a system of spinless noninteracting electrons. The Lagrangian of an electron in the presence of a magnetic field $\mathbf{B} = \nabla \times \mathbf{A}$, where $\mathbf{A}$ is the vector potential, is

$$L = \frac{1}{2}m|\dot{\mathbf{x}}|^2 - e\dot{\mathbf{x}} \cdot \mathbf{A},$$

from which we obtain the canonical momentum $\mathbf{p} = m\dot{\mathbf{x}} - e\mathbf{A}$. The Hamiltonian of the system is

$$H = \dot{\mathbf{x}} \cdot \mathbf{p} - L = \frac{1}{2m}(\mathbf{p} + e\mathbf{A})^2.$$

Note that the canonical momentum is not gauge invariant, while the mechanical momentum is. The canonical momentum obeys the usual canonical commutation relations, while the mechanical momentum $\mathbf{\Pi} \equiv m\dot{\mathbf{x}} = \mathbf{p} + e\mathbf{A}$ obeys

$$[\Pi_x, \Pi_y] = -i\hbar e\epsilon_{xyz}B_z = -i\hbar eB, \tag{A.1}$$

where we take $\mathbf{B} = B\hat{\mathbf{z}}$ for simplicity. If we introduce the operators

$$\begin{aligned} a &= \frac{1}{\sqrt{2e\hbar B}}\left(\Pi_x - i\Pi_y\right), \\ a^\dagger &= \frac{1}{\sqrt{2e\hbar B}}\left(\Pi_x + i\Pi_y\right), \end{aligned} \tag{A.2}$$

the Hamiltonian then takes the form

$$H = \hbar\omega_B\left(a^\dagger a + \frac{1}{2}\right).$$

This is exactly the same form as the Hamiltonian for a harmonic oscillator, so its energy levels are given by

$$E_n = \hbar\omega_B\left(n + \frac{1}{2}\right). \tag{A.3}$$

These are the so called *Landau levels*, which are highly degenerate. To see this, we work in the symmetric gauge and choose

$$\mathbf{A} = -\frac{1}{2}\mathbf{r} \times \mathbf{B} = -\frac{B}{2}\left(y\hat{\mathbf{x}} - x\hat{\mathbf{y}}\right) \tag{A.4}$$

We define a quantity that is similar to the mechanical momentum $\mathbf{\Pi}$, $\boldsymbol{\pi} \equiv \mathbf{p} - e\mathbf{A}$. In the symmetric gauge, it commutes with $\mathbf{\Pi}$ and thus the Hamiltonian. We can therefore use it to define another quantum number. To do this, we define another set of operators

$$\begin{aligned} b &= \frac{1}{\sqrt{2e\hbar B}}\left(\pi_x - i\pi_y\right), \\ b^\dagger &= \frac{1}{\sqrt{2e\hbar B}}\left(\pi_x + i\pi_y\right), \end{aligned} \tag{A.5}$$

such that a general state is given by two quantum numbers n and m:

$$|n, m\rangle = \frac{(a^\dagger)^n (b^\dagger)^m}{\sqrt{n!m!}}\,|0, 0\rangle\,,$$

and the energy only depends on n, which is still given by equation (A.3). From the above, we see that each Landau level is m-fold degenerate.
We are also interested in the shape of the wave functions. For a qualitative discussion of these, we consider the Landau gauge $\mathbf{A} = xB\hat{\mathbf{y}}$. The Hamiltonian then takes the form

$$H = \frac{1}{2m}\left[p_x^2 + (p_y + exB)^2\right],$$

for which the eigenvalue equation $H\psi_k(x, y) = E_k\psi_k(x, y)$ has solutions of the form

$$\psi_k(x, y) = e^{iky} g_k(x).$$

The free propagating wave comes from translational symmetry in the y direction. The eigenvalue equation then reads

$$\frac{1}{2m}\left[p_x^2 + (\hbar k + exB)^2\right]\psi_k(x, y) = e^{iky} H_k(p_x, x) g_k(x)$$

where the x-dependent part is now given by

$$H_k g_k(x) = \left[\frac{p_x^2}{2m} + \frac{m\omega_B^2}{2}\left(x^2 + kl_b^2\right)^2\right] g_k(x).$$

This the time-independent Schrödinger equation for a harmonic oscillator for which the equilibrium position has been shifted to $x_0 = -kl_b^2$, with $l_b \equiv \sqrt{\hbar/eB}$ denoting a *magnetic length*. The normalized solutions $g_{nk}(x)$ are

$$g_{nk}(x) = \frac{1}{\sqrt{2^n n!}}\left(\frac{m\omega_B}{\pi\hbar}\right)^{1/4} \mathcal{H}_n\left(\sqrt{\frac{m\omega_B}{\hbar}}(x + kl_b^2)\right) e^{-\frac{m\omega_B}{\hbar}(x + kl_b^2)^2}, \tag{A.6}$$

where $\mathcal{H}_n(x)$ are Hermite polynomials. To see how many states can occupy a certain Landau level, we need to restrict the sample to some rectangular surface of lengths L_x and L_y. Restriction along y quantises the momentum in units of $2\pi/L_y$. The restriction along x forces the wave number to take the values $-L_x/l_b^2 \leq k \leq 0$. This is because the wave function is strongly localized about $x_0 = -kl_b^2$. This gives the following number of states living in each Landau level:

$$N = \frac{L_y}{2\pi}\int_{-L_x/l_b^2}^{0} dk = \frac{L_x L_y}{2\pi l_b^2} = \frac{eAB}{2\pi\hbar} = \frac{\Phi}{\Phi_0}, \tag{A.7}$$

where the quantum of flux $\Phi_0 \equiv 2\pi\hbar/e$ has been introduced, and $\Phi = AB$ is the total flux through area A. In this way, we can understand the degeneracy of the Landau semi-classically, in the sense that if an electron occupies an area $2\pi l_b^2$ and the area of the 2D system is $L_x L_y$, then there are $L_x L_y/2\pi l_b^2$ degenerate position states the electron could be in.
One final ingredient that we need to discuss is the addition of an electric field in the x direction, $\mathbf{E} = E\hat{\mathbf{x}}$. This modifies the Hamiltonian to contain an additional term eEx, and results in a harmonic oscillator in the x direction that is shifted by a different value $x_0' = x_0 + mE/eB^2$. The energy levels now read

$$E_{nk} = \hbar\omega_B\left(n + \frac{1}{2}\right) - eB\left(kl_b^2 + \frac{eE}{m\omega_B^2}\right) + \frac{m}{2}\frac{E^2}{B^2}. \tag{A.8}$$

The degeneracy has now been lifted, and each Landau level grows linearly with the wave number k.

A.2 Quantum Mechanics of Electrons in a Electromagnetic field - Discrete Lattice Case

In this appendix, we overview a modification to the tight-binding model to accommodate magnetic fields. This is done through what is called a Peierl's substitution, and amounts to substituting the hopping parameter as follows:

$$t_{ij} \to t_{ij}\exp\left(i\frac{q}{\hbar}\int_{\mathbf{R}_j}^{\mathbf{R}_i} d\mathbf{r}\cdot\mathbf{A}\right). \tag{A.9}$$

To understand the essence of this substitution, we start from the Schrödinger equation and use the Hamiltonian of an electron in a magnetic field, as seen in part A.1, and in the presence of the periodic potential, $U(\mathbf{r})$, of the lattice.

$$\left[\frac{(\mathbf{p} - qA)^2}{2m} + U(\mathbf{r})\right]\psi(\mathbf{r}) = E\psi(\mathbf{r}). \tag{A.10}$$

Without this magnetic field, the Bloch theorem asserts that the solutions are of the form

$$\psi_{\mathbf{k}}(\mathbf{r}) = \frac{1}{\sqrt{N}} \sum_{\mathbf{R}} e^{i\mathbf{k}\cdot\mathbf{R}} \phi(\mathbf{r} - \mathbf{R}), \tag{A.11}$$

for some crystal momentum $\hbar\mathbf{k}$ and a set of lattice site coordinates $\mathbf{R}$. The localized functions $\phi(\mathbf{r})$ are usually taken to be the complete set of Wannier functions (note that we ommit the band index). Now we also recall the expression of the hopping integral in terms of the localized functions $\phi(\mathbf{r})$ above:

$$t_{ij} = \int d\mathbf{r}\ \phi^*(\mathbf{r} - \mathbf{R}_i) U(\mathbf{r}) \phi(\mathbf{r} - \mathbf{R}_j). \tag{A.12}$$

The problem with adding a magnetic field is that the functions $\psi_{\mathbf{k}}(\mathbf{r})$ cease to be eigenfunctions of the Hamiltonian operator. One way to amend that is to introduce modified localized functions $\tilde{\phi}$, which are modulated by a phase parameter containing a contribution from the gauge potential $\mathbf{A}(\mathbf{r})$:

$$\tilde{\phi}(\mathbf{r} - \mathbf{R}) \equiv \exp\left(i\frac{q}{\hbar} \int_{\mathbf{R}}^{\mathbf{r}} d\mathbf{r}' \cdot \mathbf{A}(\mathbf{r}') \right) \phi(\mathbf{r} - \mathbf{R}). \tag{A.13}$$

We can now check that using these modified functions in Eq. A.11, we have reconstructed eigenfunctions of the Hamiltonian with a magnetic field. Plugging the $\tilde{\phi}$'s into Eq. A.12, we now have

$$\begin{aligned}
\tilde{t}_{ij} &= \int d\mathbf{r}\ \exp\left[i\frac{q}{\hbar} \int_{\mathbf{R}_j}^{\mathbf{r}} d\mathbf{r}' \cdot \mathbf{A}(\mathbf{r}') - i\frac{q}{\hbar} \int_{\mathbf{R}_i}^{\mathbf{r}} d\mathbf{r}' \cdot \mathbf{A}(\mathbf{r}') \right] \phi^*(\mathbf{r} - \mathbf{R}_i) U(\mathbf{r}) \phi(\mathbf{r} - \mathbf{R}_j) \\
&= \int d\mathbf{r}\ \exp\left[i\frac{q}{\hbar} \int_{\mathbf{R}_j}^{\mathbf{R}_i} d\mathbf{r}' \cdot \mathbf{A}(\mathbf{r}') \right] \phi^*(\mathbf{r} - \mathbf{R}_i) U(\mathbf{r}) \phi(\mathbf{r} - \mathbf{R}_j) \\
&= \exp\left[i\frac{q}{\hbar} \int_{\mathbf{R}_j}^{\mathbf{R}_i} d\mathbf{r}' \cdot \mathbf{A}(\mathbf{r}') \right] t_{ij},
\end{aligned}$$

which exactly shows why one can just use a Peirels substitution of the hopping parameter to integrate the effect of a magnetic field in a system of non-interacting tightly bound electrons. A second-quantized, tight-binding Hamiltonain then reads:

$$H = \sum_i \epsilon_i c_i^\dagger c_i - \sum_{ij} t_{ij} \big(e^{i\theta_{ij}} c_i^\dagger c_j + \text{h.c} \big), \tag{A.14}$$

where θ_{ij} is the phase in Eq. A.12. This result, in two dimensions, gives rise to the well-known Hofstadter's butterfly [66], in which the "wings" represent the Chern integers of the quantum-Hall effect.

B. Appendix B

This is the source code for all plots and figures used in this thesis.

B.1 Source Code

```
#!/usr/bin/env python
# coding: utf-8

# In[ ]:


import numpy as np
import matplotlib.pyplot as plt
import matplotlib.colors as clrs
from mpl_toolkits.axes_grid1 import make_axes_locatable


def fibWord(n): #consists of N=Fibonumb((n+2)) letters
    Sn_1 = "0"
    Sn = "01"
    tmp = ""
    for i in range(2, n + 1):
        tmp = Sn
        Sn += Sn_1
        Sn_1 = tmp
    return Sn

def Fibonumb(n):
    if n<0:
        print("Incorrect input")
    # First Fibonacci number is 0
    elif n==0:
        return 0
    # Second Fibonacci number is 1
    elif n==1:
        return 1
    else:
        return Fibonumb(n-1)+Fibonumb(n-2)

```

```
N=8 #(N+1)^th generation word
F=Fibonumb(N+2) #amount of links in chain
Fm2=Fibonumb(N) #subsys N-2
Fm3=Fibonumb(N-1) #subsys N-3
ch=fibWord(N)

#conumbering
Cn=np.zeros(F)
for i in range(F):
    Cn[i]=(i+1)*(Fibonumb(N+1))%(F)

ts=5      #hopping strong
tw=1      #hopping weak


#distributing the hoppings in a Fibonacci sequence
t=np.zeros(F, dtype=np.complex128)
for i in range(F):
    if ch[i]=='0':
        t[i]=tw
    if ch[i]=='1':
        t[i]=ts


#Adding Impurities

Vimp=0.1        #weak impurity pot


v=np.zeros(F)

# n=np.random.randint(0,F,size=Nimp)   #random site assignment of
    impurities

n=[]                  # Place impurities here
Nimp=  len(n)         #number of impurities

for j in range(len(n)):

        v[n[j]]=Vimp

#constructing Hamiltonian
H=np.zeros([F,F], dtype=np.complex128)
H[0,F-1]=t[F-1]
H[F-1,0]=t[F-1].conj()
for i in range(F):
    H[i,i]=v[i]
    if i < F-1:
        H[i,i+1]=t[i]
        H[i+1,i]=t[i].conj()


```

```
#denoting atomic and molecular sites by 0 and 1 resp

tt=np.zeros(F)

for i in range(F):
    if H[i,i] == Vimp:
        tt[i]=0
    else:

        if i<F-1 and i>0:

            if H[i,i-1] == tw and H[i,i+1] == tw:
                tt[i]=-1
            else:
                tt[i]=1



#applying boundary condition:
if H[0,0] == Vimp:
    tt[F-1]=0
else:
    if t[F-1]==tw:
        tt[F-1]=tt[0]=-1
    elif t[F-1]==ts:
        tt[F-1]=tt[0]=1


SITES=np.zeros([1,F]) #initializing site representation
SITES[0,:]=tt


#computing the spectrum of the Hamiltonian

eigval, eigvect =np.linalg.eig(H)
idx = eigval.argsort()
eigval = eigval[idx]
eigvect = eigvect[:,idx]

M=np.zeros([F,F])
for i in range(F):
    M[i,:]=np.absolute(eigvect[:,i])**2



#aranging energy spectrum with conumber

MMM=np.zeros([F,F])
for i in range(F):
    for j in range(F):
        MMM[j,i]=np.absolute(eigvect[int(Cn[i])-1,j])

```

```
MM=list(reversed(MM))



#arranging the sites according to whether they are atomic or
    molecular in conumber order

tconum=np.zeros(F)
for i in range(F):
    tconum[i]=tt[int(Cn[i])-1]

TT=np.zeros([1,F])
TT[0,:]=tconum
TT[0,F-1]=TT[0,0]



#plotting the fractal together with arrangement of atomic/molecular
    sites

fig = plt.figure(figsize=[10,10])
plt.axis("off")

ax = fig.add_subplot(311, position=[0.13,0.14, 0.8, 1])
ax2 = fig.add_subplot(312, position=[0.13,0.182, 0.8, 0.1])
ax3 = fig.add_subplot(313, position=[0.13,0.08, 0.8, 0.1])

# ax.set_title("Levels vs Conumbers for N=%d sites, \n $t_s/t_w$=%g,
    $V_{imp}$=%g and $N_{imp}$=%g. $n_{imp}\in\{AMM\}$ " %(F,ts/tw,
    Vimp,Nimp), fontsize="15")

ax.set_yticklabels([])
ax.set_xticklabels([])
ax2.set_yticklabels([])
ax3.set_yticklabels([])

ax2.set_xlabel("conumber", fontsize="20")
ax.yaxis.set_label_position("right")
ax.set_ylabel("eigenstates", fontsize="20")
ax3.set_xlabel("real lattice sites", fontsize="20")

axp = ax.imshow(MM, cmap=plt.cm.Reds)

# Adding lattice sites and their conumber mapping.
colorsList = ["b","lime","gold"]
CustomCmap = clrs.ListedColormap(colorsList)
axc = ax2.imshow(TT, cmap=CustomCmap)
axs = ax3.imshow(SITES, cmap=CustomCmap)

# Minor ticks
ax2.set_xticks(np.arange(-0.5, F, 1), minor=True);
ax3.set_xticks(np.arange(-0.5, F, 1), minor=True);
```

```
186
187 ax2.grid(which='minor', color='w', linestyle='-', linewidth=1)
188 ax3.grid(which='minor', color='w', linestyle='-', linewidth=1)
189
190
191 # Adding the colorbar
192 cbaxes = fig.add_axes([0.02, 0.3, 0.04, 0.7])  # This is the position
        for the colorbar
193 cb = plt.colorbar(axp, cax = cbaxes)
194 cb.ax.set_title("$|\\psi|$", fontsize="20")
195
196 # This is the position for the at/mol cbar
197
198 cbaxes2 = fig.add_axes([0.02, 0.13, 0.04, 0.05])
199 cb = plt.colorbar(axc, cax = cbaxes2, ticks=[1, 0, -1])
200 cb.ax.set_title("nature of site", fontsize="8")
201 cb.ax.set_yticklabels(['molecular', 'impurity', 'atomic'])  #
    vertically oriented colorbar
202 cb.ax.yaxis.set_ticks_position('left')
203
204 #save
205 # plt.savefig("fract.png" , bbox_inches='tight')
206 #show
207 plt.show()
208
209
210
211 #plotting the energy spectrum
212
213 plt.figure(figsize=(10,10))
214 plt.plot(eigval, "bo",markersize=2)
215
216 plt.grid(ls="--")
217 plt.xlabel("eigenstate", fontsize=20)
218 plt.ylabel("energy (arbitrary scale)", fontsize=20)
219
220 plt.savefig("N=%g_Espect.png" %F)
221
222
223
224 #plotting the density map as a function of sites
225
226
227 fig = plt.figure(figsize=[10,10])
228 ax = fig.add_subplot(111)
229 ax.set_yticklabels([])
230 ax.set_xlabel("sites", fontsize="20")
231 ax.set_ylabel("eigenstates", fontsize="20")
232 axp = ax.imshow(M**0.1, cmap=plt.cm.binary)
233
234 idx = (np.abs(eigval - Vimp)).argmin()
235
```

```
236 ax.annotate("LM",xy=(F ,int(idx)), xytext=(F+10,int(idx)),
        arrowprops=dict(facecolor='red', shrink=0.1, width=2))
237
238 # Adding the colorbar
239 cbaxes = fig.add_axes([0.02, 0.15, 0.03, 0.7])  # This is the
        position for the colorbar
240 cb = plt.colorbar(axp, cax = cbaxes)
241 cb.ax.set_title("$|\\psi|^{0.2}$", fontsize="20")
242 #show
243 plt.show()
244
245
246
247 #plotting the localization of the clusters on atomic/molecular sites
        in renormalized chains
248
249 Ts=tw**2/ts
250 Tw=tw**3/ts**2
251 TTs=Tw**2/Ts
252 TTw=Tw**3/Ts**2
253
254 IND=np.where(eigval<-ts-tw/2)
255 KLAW=IND[0]
256
257 fig = plt.figure(figsize=[13,10])
258 # plt.title("Probability Density of atomic cluster. N=%d sites, $t_w/
        t_s=%g$" %(F,tw/ts), fontsize="15")
259
260 pden=np.zeros(F)
261 for i in range(len(KLAW)):
262     pden+=np.abs(eigvect[:,np.int(KLAW[i])])**2
263
264 plt.plot(pden)
265
266 plt.xlabel("sites", fontsize="20")
267 plt.ylabel("$\sum_n|\psi_n|^2$", fontsize="20")
268
269 #show
270 plt.show()
```

Bibliography

[1] Y.E. Kraus, Y. Lahini, Z. Ringel, M. Verbin, and O. Zilberberg. Topological states and adiabatic pumping in quasicrystals. *Physical Review Letters*, 109(10), 2012.

[2] The nobel prize in physics 2016. nobelprize.org. nobel media ab 2020. mon. 13 jul 2020. <https://www.nobelprize.org/prizes/physics/2016/summary/>, 2016.

[3] The nobel prize in chemistry 2011. nobelprize.org. tue. 14 jul 2020. <https://www.nobelprize.org/prizes/chemistry/2011/press-release/>, 2011.

[4] The nobel prize in physics 1998. nobelprize.org. nobel media ab 2020. mon. 13 jul 2020. <https://www.nobelprize.org/prizes/physics/1998/summary/>, 1998.

[5] D. Shechtman, I. Blech, D. Gratias, and J. W. Cahn. Metallic phase with long-range orientational order and no translational symmetry. *Physical Review Letters*, 53:1951–1953, 1984.

[6] E. Macia. on the nature of electronic wavefunctons in self-similar and quasiperiodic systems. *ISRN Condensed Matter Physics*, 2014:165943, 2014.

[7] J. M. Kosterlitz and D. J. Thouless. Ordering, metastability and phase transitions in two-dimensional systems. *Journal of Physics C: Solid State Physics*, 6(7):1181–1203, 1973.

[8] A. Kitaev. Fault-tolerant quantum computation by anyons. *Annals of Physics*, 303(1):2–30, 2003.

[9] K. v. Klitzing, G. Dorda, and M. Pepper. New method for high-accuracy determination of the fine-structure constant based on quantized Hall resistance. *Physical Review Letters*, 45:494–497, 1980.

[10] Y.E. Kraus and O. Zilberberg. Topological equivalence between the Fibonacci quasicrystal and the Harper model. *Physical Review Letters*, 109(11), 2012.

[11] M. Röntgen, C. V. Morfonios, R. Wang, L. Dal Negro, and P. Schmelcher. Local symmetry theory of resonator structures for the real-space control of edge states in binary aperiodic chains. *Physical Review B*, 99(21), 2019.

[12] E. Noether. Invariant variation problems. *Transport Theory and Statistical Physics*, 1(3):186–207, 1971.

[13] F. Bloch. Über die quantenmechanik der elektronen in kristallgittern. *Zeitschrift für Physik*, 52(7-8):555–600, 1928.

[14] H.A. Kramers. Théorie générale de la rotation paramagnétique dans les cristaux. *Proceedings of the Royal Netherlands Academy of Arts and Sciences*, 33(6-10):959–972, 1930.

[15] E. Hall. On a new action of the magnet on electric currents. *American Journal of Mathematics*, 2:287–292, 1879.

[16] K. S. Novoselov, Z. Jiang, Y. Zhang, S. V. Morozov, H. L. Stormer, U. Zeitler, J. C. Maan, G. S. Boebinger, P. Kim, and A. K. Geim. Room-temperature quantum Hall effect in graphene. *Science*, 315(5817):1379–1379, 2007.

[17] H.L. Stormer. The fractional quantum Hall effect (experiment). *Physica B+C*, 126(1):250 – 253, 1984.

[18] R. B. Laughlin. Anomalous quantum Hall effect: An incompressible quantum fluid with fractionally charged excitations. *Physical Review Letters*, 50:1395–1398, 1983.

[19] D. J. Thouless, M. Kohmoto, M. P. Nightingale, and M. den Nijs. Quantized Hall conductance in a two-dimensional periodic potential. *Physical Review Letters*, 49:405–408, 1982.

[20] A. Kitaev. Unpaired Majorana fermions in quantum wires. *Physics-Uspekhi*, 44(10S):131–136, 2001.

[21] A. Altland and M.R. Zirnbauer. Nonstandard symmetry classes in mesoscopic normal-superconducting hybrid structures. *Physical Review B*, 55(2):1142–1161, 1997.

[22] É. Cartan. Sur une classe remarquable d'espaces de Riemann. *Bulletin de la Société Mathématique de France*, 54:214–264, 1926.

[23] É. Cartan. Sur une classe remarquable d'espaces de Riemann. II. *Bulletin de la Société Mathématique de France*, 55:114–134, 1927.

[24] S. Ryu, A.P. Schnyder, A. Furusaki, and A.W.W. Ludwig. Topological insulators and superconductors: tenfold way and dimensional hierarchy. *New Journal of Physics*, 12(6):065010, 2010.

[25] P. A. Kalozoumis, C. Morfonios, F. K. Diakonos, and P. Schmelcher. Local symmetries in one-dimensional quantum scattering. *Physical Review A*, 87(3), 2013.

[26] P.A. Kalozoumis, C.V. Morfonios, F.K. Diakonos, and P. Schmelcher. Invariant currents and scattering off locally symmetric potential landscapes. *Annals of Physics*, 362:684 – 702, 2015.

[27] V.E. Zampetakis, M.K. Diakonou, C.V. Morfonios, P.A. Kalozoumis, F.K. Diakonos, and P. Schmelcher. Invariant current approach to wave propagation in locally symmetric structures. *Journal of Physics A: Mathematical and Theoretical*, 49(19):195304, 2016.

[28] N. Schmitt, S. Weimann, C. Morfonios, M. Röntgen, M. Heinrich, P. Schmelcher, and A. Szameit. Observation of local symmetry in a photonic system. In *Conference on Lasers and Electro-Optics*, page FM4B.7. Optical Society of America, 2019.

[29] M. Röntgen, C. V. Morfonios, I. Brouzos, F. K. Diakonos, and P. Schmelcher. Quantum network transfer and storage with compact localized states induced by local symmetries. *Physical Review Letters*, 123:080504, 2019.

[30] A. Szameit and S. Nolte. Discrete optics in femtosecond-laser-written photonic structures. *J. Phys. B: At. Mol. Opt. Phys.*, 43:080504, 2010.

[31] C.V. Morfonios, P.A. Kalozoumis, F.K. Diakonos, and P. Schmelcher. Nonlocal discrete continuity and invariant currents in locally symmetric effective Schrödinger arrays. *Annals of Physics*, 385:623–649, 2017.

[32] D. Leykam, A. Andreanov, and S. Flach. Artificial flat band systems: from lattice models to experiments. *Advances in Physics: X*, 3(1), 2018.

[33] International Crystallography Union. Report of the Executive Committee for 1991. *Acta Crystallographica Section A*, 48(6):922–946, 1992.

[34] C.J. Harris and J.F. Miles. Chapter 2 almost periodic functions. In *Stability of Linear Systems: Some Aspects of Kinematic Similarity*, volume 153 of *Mathematics in Science and Engineering*, pages 35 – 69. Elsevier, 1980.

[35] M. de Boissieu. Ted Janssen and aperiodic crystals. *Acta Crystallographica Section A*, 75(Pt 2):273–280., 2019.

[36] R. del Rio, S. Jitomirskaya, Y. Last, and B. Simon. What is localization? *Physical Review Letters*, 75:117–119, 1995.

[37] D. Damanik, M. Embree, and A. Gorodetski. Spectral properties of Schrödinger operators arising in the study of quasicrystals. *ArXiv*, 1210.5753, 2012.

[38] E. Maciá. The role of aperiodic order in science and technology. *Reports on Progress in Physics*, 69(2):397–441, 2005.

[39] A. L. Pope and T.M. Tritt. *Thermal Conductivity of Quasicrystalline Materials*, pages 255–259. Springer US, Boston, MA, 2004.

[40] C. Berger, T. Grenet, P. Lindqvist, P. Lanco, J.C. Grieco, G. Fourcaudot, and F. Cyrot-Lackmann. The new alpdre icosahedral phase: Towards universal electronic behaviour for quasicrystals? *Solid State Communications*, 87(11):977 – 979, 1993.

[41] J.M. Dubois. Bulk and surface properties of quasicrystalline materials and their potential applications. *Quasicrystals, An Introduction to Structure, Physical Properties and Applications*, pages 507–538, 2002.

[42] K. Hida. Renormalization group studies of the Fibonacci quantum spin chains. *Statistical Physics of Quantum Systems — Novel Orders and Dynamics —*, 74:57–62, 2005.

[43] C. Morfonios, P. Schmelcher, P. A. Kalozoumis, and F. K. Diakonos. Local symmetry dynamics in one-dimensional aperiodic lattices: a numerical study. *Nonlinear Dynamics*, 78(1):71–91, 2014.

[44] J. O. Hirschfelder and P. R. Certain. Degenerate rs perturbation theory. *Physical Review B*, 60(1118), 1974.

[45] H. J. Silverstone and R. K. Moats. Practical recursive solution of degenerate Sayleigh-Schrödinger perturbation theory and application to high-order calculations of the Zeeman effect in hydrogen. *Physical Review A*, 23:1645–1654, 1981.

[46] Q Niu and F Nori. Spectral splitting and wave-function scaling in quasicrystalline and hierarchical structures. *Physical Review B*, 42:10329–10341, 1991.

[47] N. Macé, A. Jagannathan, and F. Piéchon. Fractal dimensions of wave functions and local spectral measures on the Fibonacci chain. *Physical Review B*, 93(20), 2016.

[48] C. Sire and R. Mosseri. Excitation spectrum, extended states, gap closing : some exact results for codimension one quasicrystals. *Journal de Physique*, 51:1569 – 1583, 1990.

[49] M. Kohmoto and Jayanth Banavar. Quasiperiodic lattice: Electronic properties, phonon properties, and diffusion. *Physical Review B*, 34:563–566, 1986.

[50] E.N. Economou. *Green's Functions for Tight-Binding Hamiltonians*. Springer-Verlag, Heidelberg, Germany, 2006.

[51] E.N. Economou. *Single Impurity Scattering*. Springer-Verlag, Heidelberg, Germany, 2006.

[52] P. Titum, N. H. Lindner, M.C. Rechtsman, and G. Refael. Disorder-induced Floquet topological insulators. *Physical Review Letters*, 114:056801, 2015.

[53] D. Toniolo. On the equivalence of the Bott index and the chern number on a torus, and the quantization of the Hall conductivity with a real space kubo formula. *ArXiv*, 1708.05912, 2017.

[54] T.A. Loring. A guide to the Bott index and localizer index. *ArXiv*, 1907.11791, 2019.

[55] Xie Chen, Zheng-Cheng Gu, and Xiao-Gang Wen. Local unitary transformation, long-range quantum entanglement, wave function renormalization, and topological order. *Physical Review B*, 82(15), 2010.

[56] A. Hamma, R. Ionicioiu, and P. Zanardi. Ground state entanglement and geometric entropy in the Kitaev model. *Physics Letters A*, 337(1-2):22–28, 2005.

[57] T. A. Loring and M. B. Hastings. Disordered topological insulators via c*-algebras. *EPL (Europhysics Letters)*, 92(6):67004, 2010.

[58] Y. Ge and M. Rigol. Topological phase transitions in finite-size periodically driven translationally invariant systems. *Physical Review A*, 96(2), 2017.

[59] D. Toniolo. Time-dependent topological systems: A study of the Bott index. *Physical Review B*, 98(23), 2018.

[60] J. Michala, A. Pierson, T.A. Loring, and A.B. Watson. Wave-packet propagation in a finite topological insulator and the spectral localizer index. *ArXiv*, 2001.05008, 2020.

[61] T. Loring and Hermann S.B. The spectral localizer for even index pairings. *ArXiv*, 1802.04517, 2018.

[62] H.C. Jiang, Z. Wang, and L. Balents. Identifying topological order by entanglement entropy. *Nature Physics*, 8(12):902–905, 2012.

[63] A. Kitaev and J. Preskill. Topological entanglement entropy. *Physical Review Letters*, 96(11), 2006.

[64] M. Levin and W. Xiao-Gang. Detecting topological order in a ground state wave function. *Physical Review Letters*, 96(11), 2006.

[65] D. Tong. Lectures on the quantum-Hall effect. *ArXiv*, 1606.06687, 2016.

[66] D.R. Hofstadter. Energy levels and wave functions of bloch electrons in rational and irrational magnetic fields. *Physical Review B*, 14:2239–2249, 1976.